Investigations into hybrids of carbon nanotubes and organo-metallic molecular systems

Lewis, Peter

Award date:
2014

Awarding institution:
University of Bath

Investigations into hybrids of carbon nanotubes and organo-metallic molecular systems

Submitted by

Peter Rex Lewis

for the degree of Doctor of Philosophy

of the

University of Bath

Department of Physics

November 2013

Copyright

Signature of author.....

Peter Rex Lewis

Abstract

Endohedral functionalization via supercritical CO_2 was undertaken in order to produce encapsulation of organometallic systems that are difficult to encapsulate otherwise due to either their large size or extreme air sensitivity. Organometallic molecular systems from the prophyrin and phthalocyanine families (such as NiPc, ClAlPc and NiTPP) were successfully encapsulated inside of nanotubes with relatively large diameters (centred around 2 nm). This was assessed by a combination of high resolution transmission electron microscopy (HRTEM) and Raman spectroscopy. HRTEM revealed previously unreported ordering of NiTPP, a large planar molecule, in row-like assemblies inside nanotubes of diameters that match best the geometrical size of the molecule (2 nm), highlighting the role of confinement in promoting assembly. Using both endohedral and exohedral functionalization with NiTPP, ClAlPc and NiPc molecules provided a set of systems differing by only one specific parameter (e.g. central ion or body type, or size of the HOMO-LUMO gap), or comparatively affected the ability to bind to the nanotubes - the associated changes in the electronic properties of the nanotubes were revealed by resonant Raman spectroscopy. These changes were interpreted in terms of ability of the guest molecular species to produce charge transfer to/from the nanotube, and/or induce structural strain.

Acknowledgements

I would like to thank the following people for the contributions they have made to my PhD studies: My supervisor Dr. Adelina Ilie for all her support, mentoring and guidance.

All the academic and support staff of the University of Bath who assisted me during my studies, in particular, Dr. John Mitchels for his help with operating the TEM and Raman spectrometer of the Microscopy and Analysis suite; Dr. Daniel Wolverson of the Physics department for his help and guidance with my Raman spectroscopy experiments; Dr. Simon Brayshaw of the Chemistry department for his assistance with my molecular filling experiments; Dr. Michael Grogan for his help with learning how to use the software of the supercritical CO_2 rig and Wendy Lambson for all her help and advice in the ordering and use of the chemicals which I have needed during my studies.

The staff at Exeter University Physics department, in particular, Dr. Annette Plaut for kindly arranging for me to visit Exeter to carry out some of my Raman spectroscopy investigations and Ellen Green for setting up the Raman spectrometer and teaching me how to use it. My family and friends for supporting me throughout my PhD.

Contents

Chapter 1

Introduction

1.1 Motivation

Carbon nanotubes are members of the carbon nanomaterials family that revolutionised the field of Nanoscience and Nanotechnology. After having been reported in literature for several decades, carbon nanotubes were finally recognised in 1991 as a new form of carbon [1]. Carbon nanotubes are a one dimensional material and can be thought of as rolled up sheets of graphene, a two dimensional carbonaceous material which was only isolated in 2004 [2].

Carbon nanotubes are formed from sp^2 hybridized carbon atoms bonded to form a honeycomb structure. Carbon nanotubes and graphene are very strong mechanically, due to the strong bonds that form along the sheets plane. Single-walled carbon nanotubes exhibit semiconducting or metallic properties depending on how they are rolled [3].

There are two main motivations for functionalizing carbon nanotubes to produce new hybrid materials, (i) to combine their impressive electronic and structural properties with those of another system to obtain a new material with a combination of the properties of both components, and (ii) to make use of the nanoscale confinement provided by the cavity of the nanotube to create novel phases of nanomaterials.

Single walled carbon nanotubes (SWNTs) can be used to create hybrids in many ways, either involving the outer surface [4], the inner hollow cavity [5,6] or even their ends. There are numerous examples of external functionalization involving both covalent [4] and non-covalent derivatisation with various molecular species [7]. The selection of carbon nanotubes as nanoscale containers for molecular filling is driven by the fact that they provide nanoscale confinement and form a barrier between the molecular filling and the external environment [7]; this would be extremely advantageous if the filling material is for example sensitive to environmental factors such as oxidation. Confinement of material inside carbon nanotubes has been found to be a way to produce new low-dimensional hybrid nanomaterials with diverse nanoscale properties and applications [8, 9]. These range from nano-chemistry vessels [10], atto-gram mass transport [11] and chemical sensors [12], to spin-based switching for quantum information [13] and vectors for drug delivery [14]. There are two main classes of encapsulated systems: (i) inorganic compounds in the shape of nanowires and nanocrystals which form directly inside the nanotubes [6] and (ii) molecular systems which are already pre-formed before entering the nanotubes [7], [15, 16].

Organic molecules such as porphyrins are very important biologically. Members of this family are present both in blood (heme) and in plants (chlorophyll). The strong optical absorption of such organo-metallic molecules makes them strong candidates for inclusion into photovoltaic devices [17]. Other organo-metallic molecules such as phthalocyanines, a close relative to the porphyrin family, display useful bulk properties including dichroism and luminescence, and are used in gas-detection [18]. Organo-metallic molecules such as metallo-porphyrins are well known as charge donors [19] when introduced to a suitable substrate. The metal ion core of these molecules carry a non-zero magnetic spin which can make these hybrid systems paramagnetic and hence interesting for theranostic applications of carbon nanotube hybrids [14].

In this study single walled carbon nanotubes (SWNTs) have been functionalized both endo- and exohedrally with selected organo-metallic molecules: NiPc and ClAlPc from the phthalocyanine family and NiTPP from the porphyrin family.

To our knowledge, hybrids of carbon nanotubes with these molecular systems have not been produced to date. In general, encapsulation inside carbon nanotube templates confers a robustness to the hybrid system which is not present when the molecular systems are attached exohedrally. For this reason, our primary target was to employ a suitable method to produce endohedral encapsulation. We have chosen a supercritical fluid-based processes to induce encapsulation inside of nanotubes as this is particularly suitable for large molecular systems, such as NiTPP, which has low diffusional properties and therefore cannot be encapsulated by mere thermal diffusion; or for systems that are air-sensitive and have to be processed in solution. Supercritical CO_2 has not been widely applied as a filling method for carbon nanotubes. We showed that it produced successful encapsulation in carbon nanotubes with a range of diameters, from 1.3 up to 3.0 nm. Characterization with high resolution transmission electron microscopy (HRTEM) revealed previously unreported row-like ordering of large planar molecules.

Comparisons were also sought from the exohedral functionalization of the carbon nanotubes with the same organo-metallic systems. This is because metallo porphyrins and phthalocyanines are expected to functionalize less effectively the outer surface of the nanotubes (due to chelation with the central metal ion that perturbs their aromacity). Raman spectroscopy has been used as the main tool to probe the changes in the electronic properties of the nanotubes upon both endo and exo-hedral functionalization. The choice of molecules allowed well-motivated comparisons as (i) NiPc and NiTPP share the same metal ion core, but differ in their central ring structure and appendages, (ii) ClAlPc and NiPc share the same body, but have different central cores which makes the ClAlPc strongly dipolar, and finally (iii) the three systems have different sizes of the HOMO-LUMO gaps which confers them different propensity for charge transfer to or from the carbon nanotubes.

1.2 Summary of thesis

This thesis has been divided into seven chapters. Chapter 1 introduces the background of the subject and specific motivation. Relevant elements of theory for carbon nanotubes are given in Chapter 2. Chapter 3 deals with the factors that control encapsulation and exohedral functionalization of carbon nanotubes with guest species. Focus is on the specificity of the organo-metallic systems used. The suitability of the supercritical CO_2 process for molecular filling is argued. Chapter 4 describes the instrumentation developed and implemented concerning the supercritical CO_2 processes undertaken in this study. It also outlines the basic purification, characterization, washing and functionalization procedures applied to carbon nanotubes. Chapter 5 describes HRTEM investigations and brings evidence of successful encapsulation and ordering inside carbon nanotubes. It also presents comparisons with relevant encapsulated systems from prior work. Chapter 6 includes relevant elements of Raman spectroscopy theory and presents comparative studies applied to the nanotubes endo- and exohedrally functionalized with the organo-metallic systems. The results are discussed in terms of charge transfer between the organo-metallic guests and the nanotubes, and induced structural strain. Conclusions and future work are provided in Chapter 7.

Chapter 2

Background and theory

In this chapter the relevant theory for carbon nanotubes is discussed. The possible types of orbital hybridization of the carbon atom are briefly reviewed with a focus on the sp^2 hybridization found in graphene and carbon nanotubes. The lattice structure of graphene is described and the energy dispersion relation is obtained using the tight binding method. The structural and electronic properties of carbon nanotubes are then discussed in terms of those of graphene.

2.1 Carbon

Carbon is an element which possesses many allotropes. One of the most well known carbon based structure is diamond. Diamond is both very hard and a very good electrical insulator. In contrast, another common allotrope of carbon, graphite, has vastly different properties. It is a very soft material and a good conductor. It is the hybridisation of the atomic orbitals of carbon which make such great variation between its allotropes possible.

The carbon atom is the sixth atom in the periodic table. Every atom of carbon has six electrons, two of which are tightly bound and fully occupy the spherical 1s orbital.

The outer or valence electrons are less tightly bound and occupy the 2s, 2p orbitals. In the ground state, the electronic configuration of carbon is $2s^2$, $2p_x{}^1$, $2p_y{}^1$. With just a small excitation it is possible to raise an electron from the 2s orbital to into a $2p_z$ orbital; this process is called promotion. In the promoted state the carbon atom has the configuration $2s^1$, $2p_x{}^1$, $2p_y{}^1$, $2p_z{}^1$. In this state the wavefunctions of the separate atomic orbitals can interfere to produce hybrid orbitals.

There are three possible hybridization types; sp^3, sp^2 and sp. In sp^3 hybridisation a linear combination of the 2s, $2p_x$, $2p_y$ and $2p_z$ results in four equivalent hybridised orbitals. These form a tetrahedral structure, with each pointing to one of the four corners of a regular tetrahedron. The overlap of these hybridised orbitals can form strong molecular bonds called sigma (σ) bonds. Sigma bonds have cylindrical inter-atomic symmetry. In diamond, every carbon atom forms four σ bonds with four surrounding carbon atoms. This gives diamond high 3-dimensional regularity and great strength.

The hybridisation involved in graphite is sp^2. The hybridized atomic orbitals are formed from linear combinations of the 2s, $2p_x$ and $2p_y$. The possible linear combinations are:

$$h_1 = s + 2^{\frac{1}{2}} p_y \quad h_2 = s + \left(\tfrac{3}{2}\right)^{\frac{1}{2}} p_x - \left(\tfrac{1}{2}\right)^{\frac{1}{2}} p_y \quad h_3 = s - \left(\tfrac{3}{2}\right)^{\frac{1}{2}} p_x - \left(\tfrac{1}{2}\right)^{\frac{1}{2}} p_y \tag{2.1}$$

The resulting orbital configuration is trigonal in structure and planar in nature. The three equivalent hybridised orbitals point to the corners of an equilateral triangle and are separated by 120^o as shown by Figure 2.1 (a). Each of these hybridised orbitals is capable of overlapping with another hybridized orbital to form a σ bond. The $2p_z$ orbitals do not take part in the hybridisation process. Instead the two lobes of the $2p_z$ orbital are directed perpendicular to the trigonal plane out of the plane - this is shown in Figure 2.1 (b).

When two or more carbon atoms with un-bonded $2p_z$ orbitals come into close proximity, for example in the aromatic ring shown in Figure 2.1 (c), a molecular bond called a π bond is created.

A π bond is formed by the overlap of two in-phase $2p_z$ orbitals.

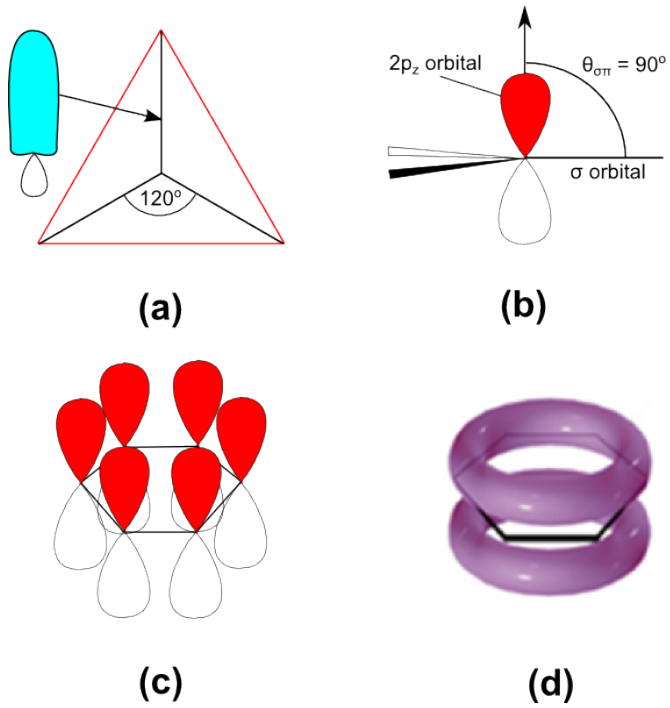

Figure 2.1: Diagrams of (a) sp^2 hybridized σ orbitals of trigonal carbon (adapted from [20]) (b) un-hybridized $2p_z$ orbital (c) schematic diagram of an aromatic ring (d) schematic diagram showing the delocalized nature of the electrons in the π bonding orbitals of an aromatic ring [21].

In a π bond the probability density of the electron between the atoms is continuous as shown below in Figure 2.1 (d) and the electrons become delocalized and are shared between the atoms of the ring. π bonds are weaker than sigma bonds and as a result the electrons are much less tightly bound.

2.2 Graphene

Graphene is a planar material of only one carbon atom in thickness. It is formed from sp^2 hybridized carbon atoms arranged in a hexagonal structure.

Figure 2.2 shows the structure of graphene. The three sp^2 hybridised orbitals of the carbon atoms form three σ bonds with the orbitals of three adjacent carbon atoms. This pattern is repeated throughout the graphene sheet resulting in its distinctive honeycombed structure.

2.2.1 The graphene lattice

The structure of graphene does not fit into a regular lattice. This is because it is not possible to create unit translation vectors which will allow one to reach all of the atoms in the structure. Instead it is necessary to split the main structure into two sub-lattices. The green dots present in Figure 2.2 represent sub-lattice A and the blue dots represent sub-lattice B. Each of the sub-lattices is a Bravais lattice and possesses three directions of symmetry. These are shown as blue dotted lines in the top left part of the figure. Each line of symmetry is separated by an angle of 120^{o}.

The unit cell of a Bravais lattice is created around a single atom. Due to the unique structure of the graphene lattice, it is necessary to have one atom from each sub-lattice in the unit cell. This results in the unit cell of graphene being a rhombus shape - the unit cells are shown in red. Each of the four corners of the unit cells lies in the centre of a hexagon. These are the lattice points of the graphene lattice. This form of unit cell is the smallest shape that can be fitted to the lattice that includes both atoms of the sub-lattice and can be repeated to encompass the entire lattice.

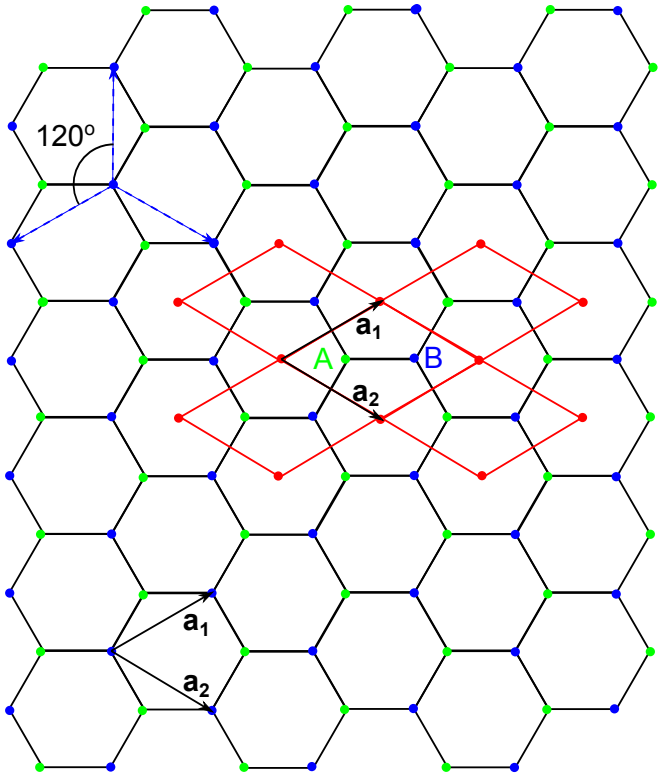

Figure 2.2: The crystal structure of graphene. Atoms A and B are non-equivalent atoms. The vectors $\mathbf{a_1}$ and $\mathbf{a_2}$ are the unit translation vectors of the graphene lattice. The red rhombuses are unit cells of the graphene lattice. The blue dotted lines indicate the three directions of symmetry in the graphene lattice.

The unit vectors of the of the Bravais lattice are given below:

$$\vec{a}_1 = \left(\frac{\sqrt{3}a}{2}, \frac{a}{2}\right) \quad \vec{a}_2 = \left(\frac{\sqrt{3}a}{2}, -\frac{a}{2}\right) \tag{2.2}$$

where $|\vec{a}_1| = |\vec{a}_2| = \text{a} = 2.46$ Å, and the carbon-carbon sp^2 bond length $= \frac{a}{\sqrt{3}} = 1.42$Å.

2.2.2 The reciprocal lattice of graphene

To facilitate the determination of the electronic structure of graphene it is useful to transform the real lattice into reciprocal space. The reciprocal lattice of graphene is shown in Figure 2.3 below.

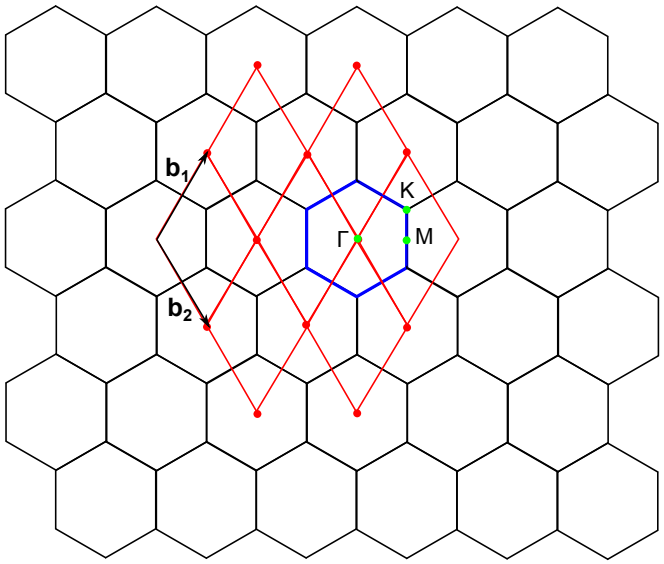

Figure 2.3: The reciprocal lattice of graphene. The unit cells of the reciprocal lattice are shown as red rhombuses. $\mathbf{b_1}$ and $\mathbf{b_2}$ are the lattice vectors of the reciprocal lattice. The blue hexagon shown in the figure is the first Brillouin zone. Γ, K and M are points of high symmetry in the lattice.

Comparing Figures 2.2 and 2.3, it can be seen that the reciprocal lattice is orthogonal to the real lattice. This is directly related to the general structure of reciprocal lattice translation vectors.

In general, the reciprocal translation vectors of this two dimensional lattice take the form:

$$\vec{b}_1 = 2\pi \left(\frac{\vec{a}_2 \times \vec{a}_3}{\vec{a}_1 \cdot \vec{a}_2 \times \vec{a}_3} \right) \quad \vec{b}_2 = 2\pi \left(\frac{\vec{a}_3 \times \vec{a}_1}{\vec{a}_1 \cdot \vec{a}_2 \times \vec{a}_3} \right) \tag{2.3}$$

where $\vec{a}_3 = 0\hat{i} + 0\hat{j} + c\hat{k}$, $\vec{a}_1$ and $\vec{a}_2$ are the real translation vectors of the graphene lattice.

Using equations (2.3) the reciprocal lattice vectors of graphene can be shown to be:

$$\vec{b}_1 = \left(\frac{2\pi}{\sqrt{3}a}, \frac{2\pi}{a} \right) \quad \vec{b}_2 = \left(\frac{2\pi}{\sqrt{3}a}, -\frac{2\pi}{a} \right), \tag{2.4}$$

where $|\vec{b}_1| = |\vec{b}_2| = \frac{4\pi}{a\sqrt{3}}$.

The first Brillouin zone is defined as the primitive cell of the reciprocal lattice. It is useful for describing the electronic properties of a material. The electronic distribution found in the 1st Brillouin zone is common to the entire reciprocal lattice. The points labelled Γ, K and M are the points of high symmetry in the reciprocal lattice of the graphene sheet.

2.2.3 The tight-binding approximation for the energy band structure

In the idealised view of atoms, electrons occupy well defined orbitals and possess a quantised energy depending on the orbital type and principle quantum level. However, when two or more atoms are brought into close proximity, as is the case in a crystal lattice, the valence electrons interact. The eigenstates of the valence electrons interfere and create energy bands. In the case of the graphene lattice the most interesting energy band is formed by the $2p_z$ valence electrons. These are known as the π bands of graphene. It is these bands which are closest in energy to the Fermi energy and hence are most important for charge transport.

In the tight-binding method (sometimes called the linear combination of atomic orbitals method) the starting point is the set of orbital energy levels of the tightly bound electrons of a single isolated atom. With other near neighbour atoms brought near to this originally isolated atom, the wavefunction of the original atom would be overlapped by those of the near neighbour atoms. If the atoms are far enough apart, this overlap would be small enough for it to be taken into account just by making comparatively small corrections to the originally isolated atom model. The overall picture of the energy levels of a lattice of atoms is made up of slightly modified atom models [22].

The tight-binding method can be used to calculate an empirical solution for the band structure of graphene as follows [3].

The crystal lattice of graphene possesses translational symmetry along the lattice vectors $\vec{a}_1$ and $\vec{a}_2$, this implies that any wavefunction of the lattice, Ψ, should obey Blochs theorem

$$T_{\vec{a}_i}\Psi = e^{i\vec{k}\cdot\vec{a}_i}\Psi \tag{2.5}$$

where in graphene $i = 1, 2$ and $T_{\vec{a}_i}$ is a lattice translation operator and $\vec{k}$ is the wave vector of the lattice.

The wavefunctions that satisfy this condition are called Bloch orbitals. There are two Bloch orbitals for graphene, one for each sub lattice. These take the form shown below.

$$\Phi_j(\vec{k}, \vec{r}) = \frac{1}{\sqrt{3}} \sum_{\vec{R}_j}^{N} e^{i\vec{k}\cdot\vec{R}_j}\phi_j(\vec{r} - \vec{R}_j) \tag{2.6}$$

where $(j = A, B)$ and $\vec{R}_j$ and $\vec{r}$ are position vectors of the atom j and the $2\mathrm{p_z}$ orbital of atom j respectively. The atomic orbital of atom j is designated by $\phi_j(\vec{r} - \vec{R}_j)$. With each individual orbital multiplied by its phase factor $e^{i\vec{k}\cdot\vec{r}}$, a summation over the whole lattice (N unit cells) will produce $\Phi_j(\vec{k}, \vec{r})$. The wavefunction of the crystal lattice, $\Psi(\vec{k}, \vec{r})$, is a linear combination of Φ_A and Φ_B.

$$\Psi_j(\vec{k}, \vec{r}) = \sum_{j,j'=A,B} C_{jj'}\Phi_{j'}(\vec{k}, \vec{r}), \tag{2.7}$$

where $j, j' = A, B$ and $C_{jj'}$ are complex coefficients.

The energy eigenvalues $E(\vec{k})$ of the eigenstate (2.7) can be found by solving the time independent Schrödinger equation

$$\hat{H}|\Psi_j\rangle = E(\vec{k})|\Psi_j\rangle \tag{2.8}$$

where $\hat{H}$ is the Hamiltonian of the graphene lattice.

By taking the inner product of (2.8) and inserting (2.7), it is possible to derive the secular equation.

The energy dispersion relation of graphene is described by the following equation:

$$det[H - ES] = 0 \tag{2.9}$$

In this case, $H_{jj'} = \langle \Phi_j | H | \Phi_{j'} \rangle$ and $S_{jj'} = \langle \Phi_j || \Phi_{j'} \rangle$ are the transfer integral matrices and overlap integral matrices respectively.

The secular equation for graphene is given by

$$\begin{vmatrix} H_{AA}(\vec{k} - E(\vec{k}) \cdot S_{AA}(\vec{k}) & H_{AB}(\vec{k} - E(\vec{k}) \cdot S_{AB}(\vec{k}) \\ H_{BA}(\vec{k} - E(\vec{k}) \cdot S_{BA}(\vec{k}) & H_{BB}(\vec{k} - E(\vec{k}) \cdot S_{BB}(\vec{k}) \end{vmatrix} = 0 \tag{2.10}$$

In order to solve the secular equation, it is necessary to take the lattice structure of graphene into account.

The three nearest neighbours belong to a different sub-lattice (surrounding atoms belong to the blue sub-lattice - see Figure 2.4). With these considerations in mind a number of simplifications can be made to the secular equation. As we are only considering interactions between nearest neighbours (shown schematically in Figure 2.4), it is only necessary to integrate over the single atom in H_{AA} and H_{BB}. This results in a number of useful simplifications,$H_{AA} = H_{BB} = \epsilon_{2p_z}$, $S_{AA} = S_{BB} = 1$ and $S_{AB} = sf(\vec{k}) = S^*_{BA}$. Here ϵ_{2p_z} is the energy of the $2p_z$ orbital, s is the nearest neighbour overlap integral and $f(\vec{k}) = (e^{i\vec{k}\cdot\vec{R}_1} + e^{i\vec{k}\cdot\vec{R}_2} + e^{i\vec{k}\cdot\vec{R}_3})$.

The contributions from the three nearest neighbours in the lattice are described by

$$H_{AB} = H_{BA} = \gamma_0 \cdot (e^{i\vec{k}\cdot\vec{R}_1} + e^{i\vec{k}\cdot\vec{R}_2} + e^{i\vec{k}\cdot\vec{R}_3}) = \gamma_0 \cdot f(\vec{k}) \tag{2.11}$$

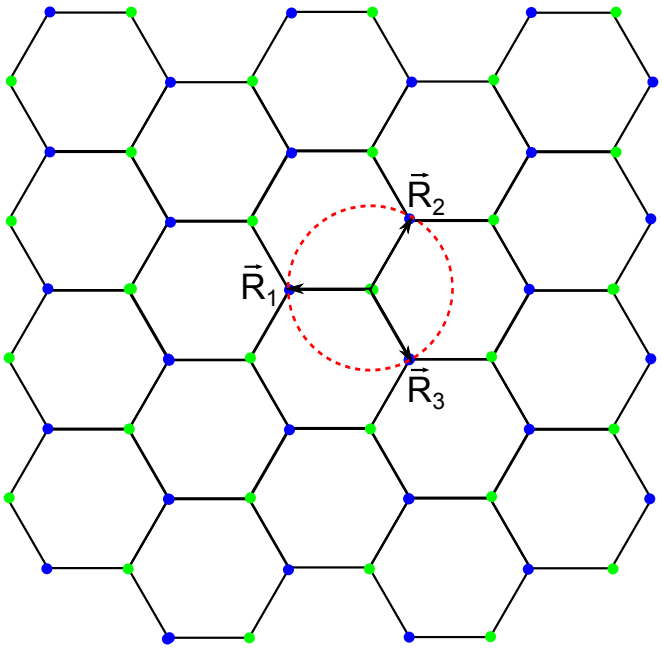

Figure 2.4: The three nearest neighbour atoms relative to atom are shown as red dots. The position vectors $\vec{R}_1$, $\vec{R}_2$ and $\vec{R}_3$ give the relative locations of the three nearest neighbours.

where γ_0 is the nearest neighbour transfer integral

$$\gamma_0 = \langle \Phi_A(\vec{r} - \vec{R}_A)|H|\Phi_A(\vec{r} - \vec{R}_A - \vec{R}_1)\rangle \tag{2.12}$$

Inserting the above simplifications into the secular equation allows for eigenvalues $E(\vec{k})$ to be found. Here $E(\vec{k})$ is a function of $w(\vec{k})$, k_x and k_y:

$$E(\vec{k}) = \frac{\epsilon_{2p_z} \pm \gamma_0 w(\vec{k})}{1 \pm s w(\vec{k})} \tag{2.13}$$

The positive and negative signs combine to give either the bonding energy band π (positive combination) or the anti-bonding π^* band (negative). The ϵ_{2p_z} and s terms are constant which are important in determining the absolute energy but not for appreciating the form of the energy bands.

The function $w(\vec{k})$ is given by:

$$w(\vec{k}) = \sqrt{|f(\vec{k})|^2} = \sqrt{1 + 4cos\frac{\sqrt{3}k_x a}{2}cos\frac{k_y a}{2} + 4cos^2\frac{k_y a}{2}} \tag{2.14}$$

where k_x and k_y are lattice wave vectors of the reciprocal lattice respectively and a is the modulus of the real lattice translation vectors [23].

2.2.4 The electronic band structure of graphene

The first Brillouin zone of the reciprocal lattice contains all of the points of high symmetry necessary to understand the unique band structure of graphene - these are shown in Figure 2.5 below.

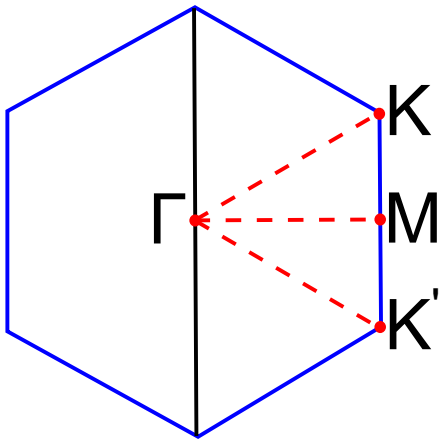

Figure 2.5: Expanded view of the first Brillouin zone of graphene labelled with the points of high symmetry (red circles), Γ, K, M and K'. K and K' are non-equivalent points as they correspond to the two non-equivalent A and B sub-lattices of the direct lattice.

The non-equivalent K and K' points, present at the corners of the Brillouin zone, mirror the atomic symmetry of the real lattice. Plotting E($\vec{k}$) along the lines of high symmetry allows for a graph of energy as a function of wave vector to be plotted, this is shown in Figure 2.6 below.

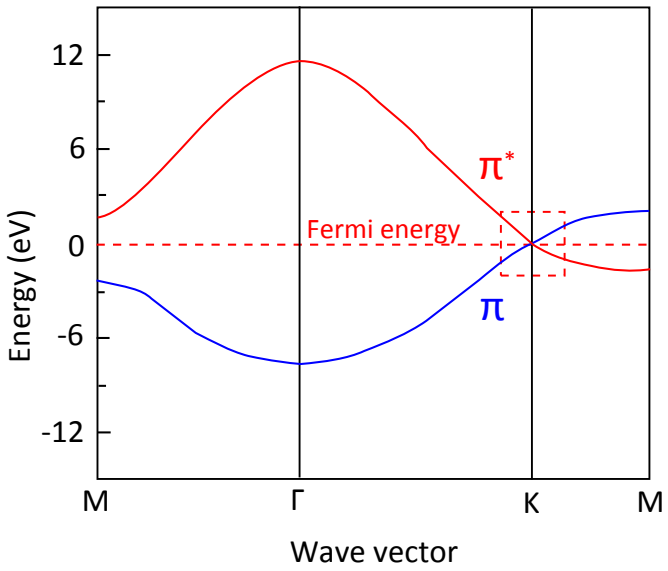

Figure 2.6: Plots of E($\vec{k}$) as a function of $\vec{k}$ along the lines of high symmetry, M $\rightarrow$ Γ, Γ $\rightarrow$ K and K $\rightarrow$ M. The plot follows the perimeter of the triangle in k space shown in Figure 2.5. The red dashed square is centred on one of the Dirac points. Adapted from [21].

The two energy bands closest to the Fermi level are the π bonding and the π^* anti-bonding bands respectively. These are highlighted in blue and red in the energy band diagram of Figure 2.6. Each of the two atoms in the lattice unit cell contribute one electron to the π bonds, these fully fill the π bonding energy band. It can be seen from the figure that the valence band (occupied π band) and the conduction band (unoccupied π^* band) meet at the K points; this classifies graphene as zero band-gap semiconductor material.

The K and K' points located at the 6 corners of the first Brillouin zone are known as Dirac points. As the band energy approaches the Fermi level, the electronic density of states at the Dirac points tends to zero. An interesting feature of the band structure of graphene is the shape of the conduction and valence bands above and below the Fermi level. It can be seen from Figure 2.7 that both bands are cone shaped at the Dirac points. The σ bands of graphene have been excluded from the figure as they are of much greater energy ($\approx$ 14eV [3]) than the π bands and therefore do not take any part in conduction, which involves energy levels around the Fermi level.

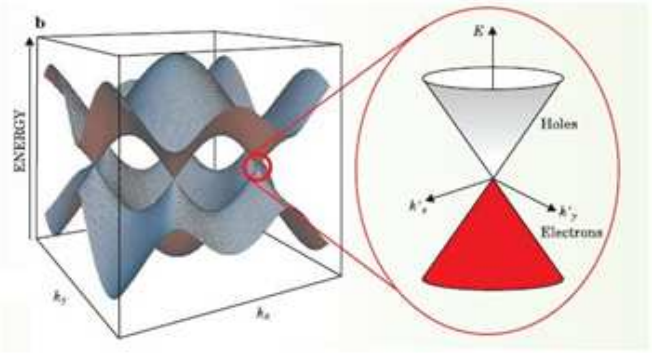

Figure 2.7: π energy bands, E, as a function of wave vector ($\vec{k}$). Insert diagram showing the linear nature of the π bands close to the π Dirac points [21].

2.3 Carbon nanotubes

2.3.1 Structure

Carbon nanotubes are a unique allotrope of carbon. Nanotubes can be thought of as being rolled sheets of graphene. The carbon atoms in a nanotube arrange themselves in hexagonal cells which link together to form long cylinders of up to 1 μm in length and diameters ranging from 0.5 to 10nm in diameter. A nanotube formed from a single sheet of graphene is known as a Single Walled Carbon Nanotube (SWNT), an example of a single walled armchair type nanotube is shown in Figure 2.8. The large majority of this work will involve SWNTs.

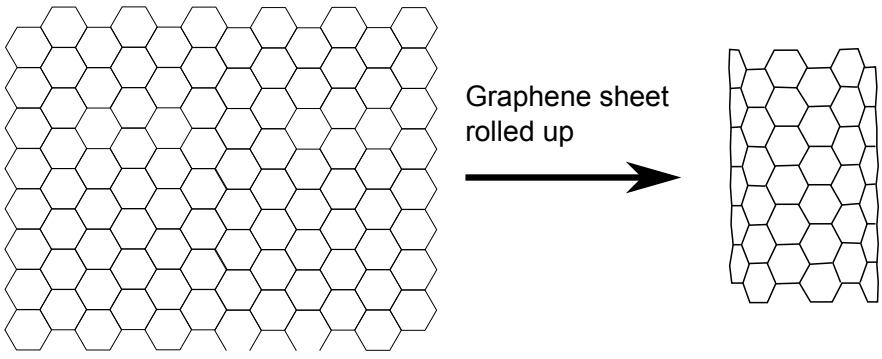

Figure 2.8: The rolling of a single walled carbon nanotube of the armchair type (based upon [24]).

It is also possible to have Multi-Walled Carbon Nanotubes (MWNTs). These are made from a number of concentric single walled nanotubes of increasing diameter, as show in Figure 2.9.

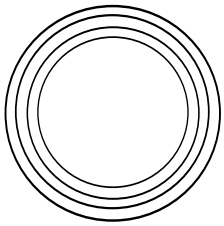

Figure 2.9: Schematic diagram of a 4 walled MWNT (end on).

There are many ways in which a graphene sheet can be rolled to form a carbon nanotube, with a wide range of resulting diameters and chiralities. The chirality of a nanotube describes the direction in which the graphene sheet has been rolled to create it. Every nanotube has an associated chiral vector $\vec{C}$ which forms the circumference of the nanotube.

The chiral vector determines the structural type and the electronic properties of the nanotube. The general form of a chiral vector is

$$\vec{C} = n\vec{a}_1 + m\vec{a}_2 = (n, m), \tag{2.15}$$

where n and m are integers [3].

There are three possible nanotube classes, armchair, zig-zag and chiral, these are shown in Figure 2.10.

Each chiral vector has an associated chiral angle, θ. This angle can be determined using the following equation [3]:

$$cos\theta = \frac{\vec{a}_1 \cdot \vec{C}}{|\vec{a}_1| \cdot |\vec{C}|} = \frac{2n + m}{2\sqrt{n^2 + nm + m^2}} \tag{2.16}$$

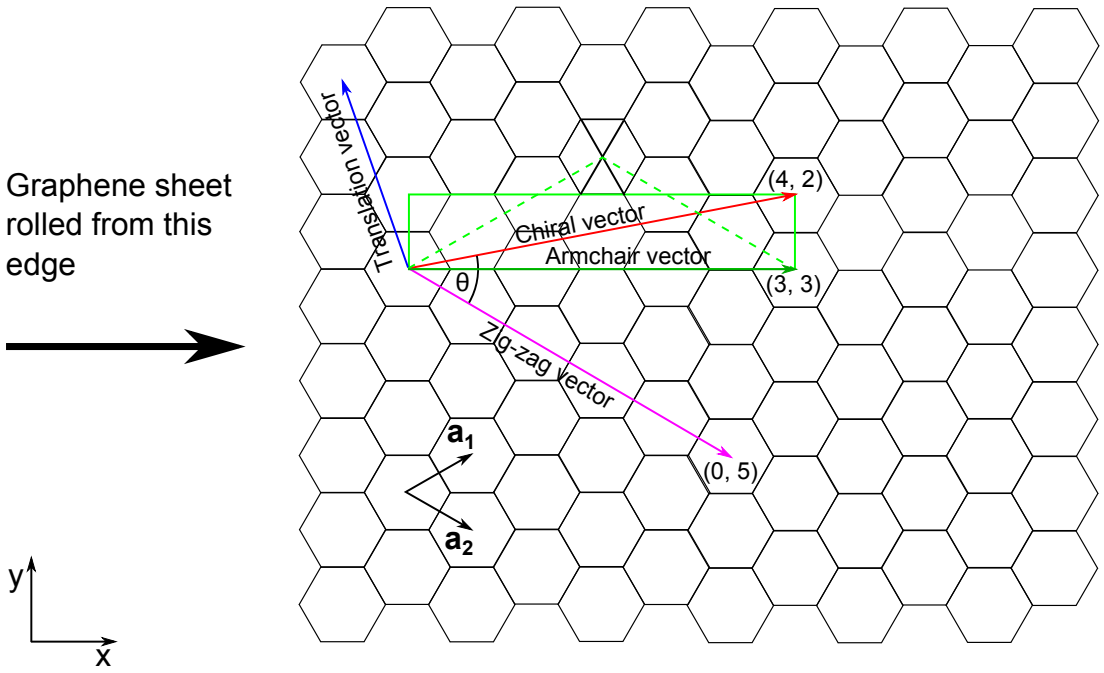

Figure 2.10: The possible chiralities of carbon nanotubes. The chiral and translation vectors of a (4,2) chiral nanotube are shown as red and blue lines respectively - the chiral and translation vectors are perpendicular to one another. The chiral angle, θ, is measured relative to the zig-zag line. The chiral vectors of (0, 5) zig-zag and (3, 3) armchair nanotubes have also been included on the diagram in magenta and green respectively. The green rectangle represents the unit cell of a (3, 3) armchair nanotube.

The chiral angles and structures of each type of nanotube are shown in Figure 2.11.

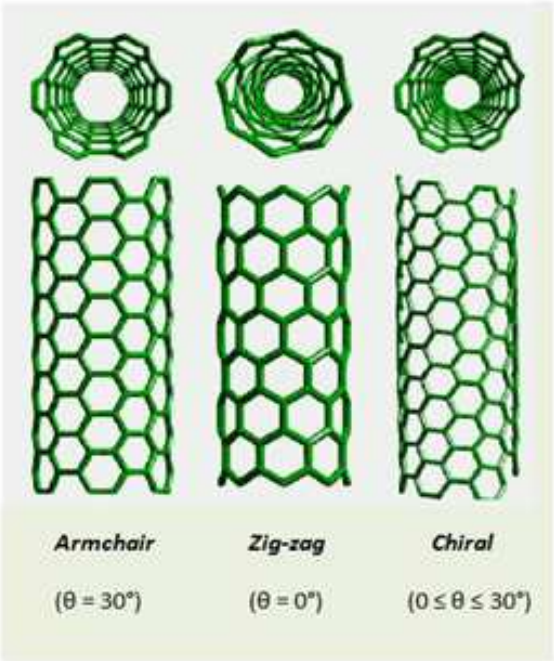

Figure 2.11: The different types of nanotube chirality and the corresponding chiral angle (Adapted from [25])

Given that the chiral vector forms the circumference of the nanotube, it is possible to determine the diameter, d, of the nanotube directly by the using the following equation [3]:

$$d = \frac{|\vec{C}|}{\pi} = \frac{a}{\pi}\sqrt{n^2 + nm + m^2} \tag{2.17}$$

The last structural property of nanotubes to be described is the translational symmetry along the length of the tube. This is determined by the translation vector,

$$\vec{T} = t_1\vec{a}_1 + t_2\vec{a}_2 \tag{2.18}$$

where t_1 and t_2 are integers which can be determined from the chiral indices n and m using the equations $t_1 = \frac{2m+n}{d_R}$ and $t_2 = -\frac{2n+m}{d_R}$ where d_R is the greatest common divisor of $(2m + n)$ and $(2n + m)$.

The translation vector, $\vec{T}$, and the chiral vector, $\vec{C}$, form a rectangle on the graphene lattice [3]. This is the unit cell of the nanotube, an example of the unit cell of a $\vec{C} = (3, 3)$ arm chair nanotube is shown as a green rectangle in Figure 2.10. The size of the minimum translation vector and hence the unit cell depends upon the chirality of the nanotube. For armchair nanotubes $|\vec{T}| = a$ and $|\vec{C}| = n\sqrt{3}a$, while for zig-zag nanotubes $|\vec{T}| = \sqrt{3}a$ and $|\vec{C}| = na$ [3]. Chiral nanotubes can have relatively large unit cells with the maximum occurring at an angle of 15°. Calculating the number of carbon atoms in a given nanotube unit cell is a reasonably simple procedure. Firstly it is necessary to calculate the number of hexagons, q, present in the unit cell of the nanotube. This can be achieved by dividing the area of the nanotubes unit cell, $S_{\mathrm{t}} = |\vec{T} \times \vec{C}|$, by the area of one hexagonal cell of graphene, $S_{\mathrm{g}} = |\vec{a}_1 \times \vec{a}_2|$,

$$q = \frac{s_t}{s_g}. \tag{2.19}$$

Given that there are two carbon atoms per hexagon, the total number of carbon atoms in the nanotube unit cell, n_{c}, is given by $n_{\mathrm{c}} = 2q$ (based upon [3]).

2.3.2 The reciprocal lattice of SWNTs

In order to effectively describe the electronic structure of carbon nanotubes it is necessary to construct the first Brillouin zone of the reciprocal lattice. Firstly, considering the lattice translation vectors along the length and around the circumference of the tube. The reciprocal lattice translation vector in the z direction of the tube, $\vec{k}_{\mathrm{z}}$, is given by:

$$\vec{k}_z = \frac{2\pi}{\vec{T}} \tag{2.20}$$

Since the diameter of a nanotube is very much less than its length, it can be thought of as being infinitely long. This results in a continuous wave vector $\vec{k}_{\mathrm{z}}$ along the tube.

As a result the first Brillouin zone extends from $\vec{k}_z = -\frac{\pi}{a}$ to $\frac{\pi}{a}$. The wavevectors in the circumferential direction, $\vec{k}_\perp$, are more interesting. Any wave vector, $\vec{k}_\perp$, is quantised according to the following boundary conditions $\mu \cdot \lambda = |\vec{C}| = \pi \cdot d$. Wave vectors which satisfy this take the form:

$$\vec{k}_{\perp,\mu} = \frac{2\pi}{\lambda} = \mu \cdot \frac{2\pi}{\vec{C}} \tag{2.21}$$

where, λ is the wavelength of the electron wavefunction and μ is the quantisation number which is an integer and can take any value from -$\frac{q}{2}$+1, 0, 1 ....,$\frac{q}{2}$. For armchair and zig-zag nanotubes $q = 2n$, while for chiral nanotubes $q = \frac{2(n_1^2+nm+n_2^2)}{d_{cd}R_c d}$. Here d_{cd} is the greatest common divisor of (n,m) and $R_{cd} = 3$ if $(n-m)/3n$ is an integer and $R_{cd} = 1$ otherwise [23].

This can be explained by considering the behaviour of an electron present on the circumference of the nanotube. An electron can only exist when the corresponding wavefunction meets the above boundary conditions. Most importantly, the wavefunction must possess a phase shift which is an integer multiple of 2π. All other phases result in destructive interference.

We now have the necessary wave vectors to describe the first Brillouin zone of a carbon nanotube. The first Brillouin zone consists of a rectangular band of parallel lines of length $\frac{2\pi}{a}(\vec{k}_z)$ directed along the $\vec{k}_z$ axis. These lines are quantised in the circumferential direction by the spacing of $\frac{2\pi}{|\vec{C}|}$. A detailed diagram of the first Brillouin zone of a (3,3) armchair nanotube is given in Figure 2.12.

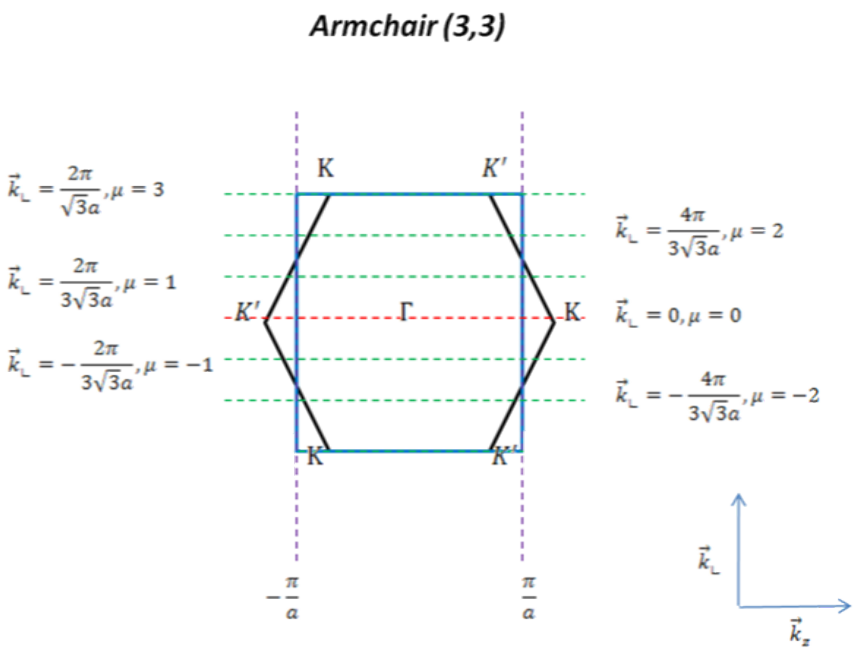

Figure 2.12: The first Brillouin zone of a (3,3) armchair nanotube.

For a given type of nanotube, the size of the Brillouin zone in the reciprocal lattice direction ($\vec{k}_z$) is constant. As the diameter of the nanotube increases, the number of quantised k lines around the circumference also increases. However, an increase in diameter also results in a decrease in the separation between the k lines. As a consequence of this, the electronic quantisation becomes less distinct with increasing diameter.

2.3.3 Electronic structure of SWNTs

If the k lines of a nanotube match up with the K points of the graphene Brillouin zone then the nanotube will be metallic. The nanotube shown in Figure 2.12 is metallic as are all armchair nanotubes; if the k lines do not intersect with any of the K points the nanotube will be semi-conducting. The zig-zag nanotubes can be either metallic or semiconducting; in addition chiral nanotubes can be a mixture of metallic and semiconducting. The basic principle of the zone folding approximation is that the electronic band structure of a nanotube can be determined from the band structure of graphene along the allowed k lines.

With the zone folding method, the band structure of graphene can be adapted to give the band structure of a nanotube by replacing the wavevectors of the graphene lattice by those of the nanotube (i.e. $k_x \rightarrow k_\perp$, $k_y \rightarrow k_z$). The band structure of a generic (n,0) zig-zag nanotube is described by the following equation:

$$E_\mu = \pm t \left[1 \pm 4cos\left(\frac{\mu \cdot \pi}{n}\right) cos\left(\frac{\sqrt{3}ka}{2}\right) + 4cos^2\left(\frac{\mu \cdot \pi}{n}\right) \right]^{\frac{1}{2}} \qquad (2.22)$$

where E_μ is the dispersion energy of the nanotube energy bands, t is the transfer integral, $-\frac{\pi}{\sqrt{3}} < ka < \frac{\pi}{\sqrt{3}}$ and n is a chiral integer and [3].

Similar expressions can be derived for armchair and chiral nanotubes. Figure 2.13 shows a plot of expression (2.22):

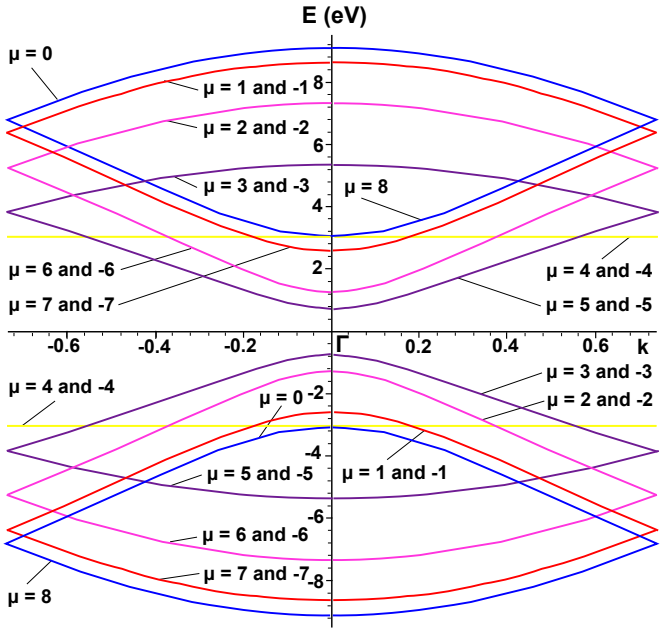

Figure 2.13: Band structure of an (8,0) semiconducting zig-zag SWNT from zone folding of graphene band structure. Image based upon [21].

The lowest energy bands of the first Brillouin zones for metallic and semiconducting nanotubes are shown in Figure 2.14.

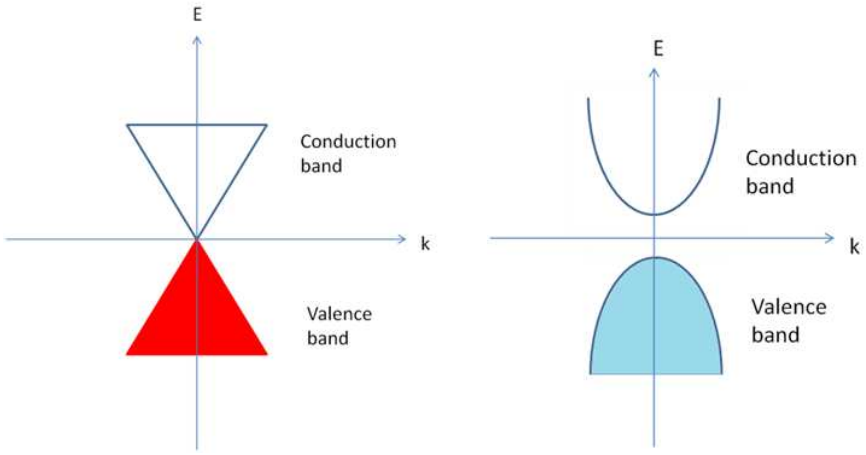

Figure 2.14: The band structures for (a) a metallic nanotube and (b) a semiconducting nanotube.

2.3.4 Electronic density of states

The electronic density of states is defined as the number of electronic states available in a given energy range; it is a quantity that is both useful for describing the electronic structure of a given nanotube, and is also measureable.

The density of states is dependent upon the dimensionality of an object - a carbon nanotube is classed as a 1 dimensional object (z direction) and is quantised in 2 directions i.e. x and y. The density of states, in a transverse direction, for a one dimensional object varies as $1/\sqrt{E}$, where E is the transverse energy. It can be shown [26] that the density of states for the first Brillouin zone of a nanotube is described by:

$$n(E) = \frac{4a}{\pi^2 d\gamma_0} \sum_{\mu=-\infty}^{\infty} g(E, E_\mu), \tag{2.23}$$

with:

$$g(E, E_\mu) = \begin{cases} |E|/\sqrt{E^2 - E_\mu^2} & |E| > |E_\mu| \\ 0 & |E| < |E_\mu| \end{cases} \tag{2.24}$$

The density of states for an (8,0) semiconducting zig-zag SWNT and a (5,5) metallic armchair SWNT are shown in Figure 2.15.

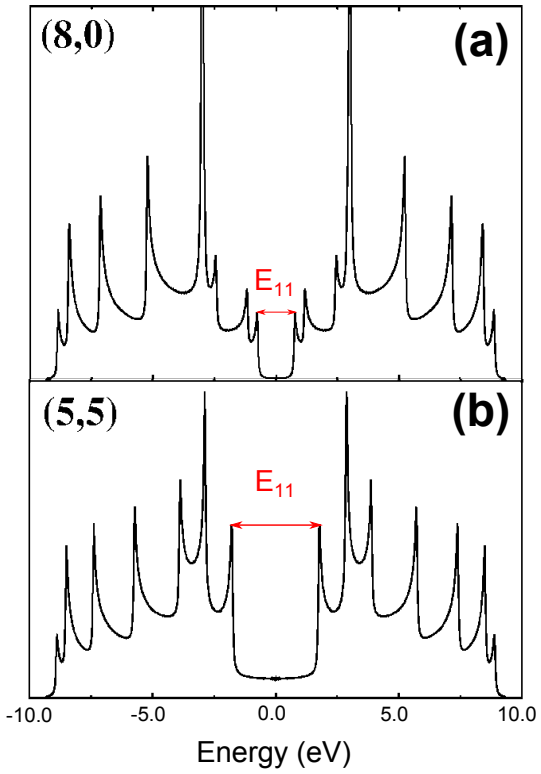

Figure 2.15: Density of states (DOS) as a function of energy, for a selection of SWNTs: (a) semiconducting and (b) metallic. The transition E_{11} has been labelled in red as an example (based on [27]). It is worth noting the differences between semiconducting and metallic nanotubes at the Fermi energy (Energy = 0), specifically, in semiconducting nanotubes the DOS is zero - in contrast for metallic nanotubes it is non-zero.

The following points are of note (Figure 2.15):

1) At the quantisation energies E = E_μ the function g(E, E_μ) diverges and produces what is called a van Hove singularity [3].

2) For the special case of $E_\mu = 0$, g(E,E_μ) becomes unity, the conduction and valence bands of the nanotube meet at the Fermi energy - the nanotube is metallic (Figure 2.15. b)).

The density of states peak at the singularities, as a result they dominate the physical properties of the nanotube. Concerning the optical properties of nanotubes, for a photon to be absorbed it has to match the energy interval E_{ii}, (see Figure 2.15) between symmetric singularities in the valence and conduction bands [27].

Chapter 3

The encapsulation of molecular systems by carbon nanotubes using a supercritical carbon dioxide-based method

In this chapter the factors affecting the binding of molecules to the external and internal surfaces of a carbon nanotube are reviewed. We targeted the encapsulation of organo-metallic molecular systems via a supercritical CO_2 process, whose physical mechanisms and advantages are described in detail. The choice of the molecular systems to be encapsulated is also justified: it includes molecules that are sensitive to air (and would benefit from having the nanotube protection), molecules that have large dimensions and hence lower diffusion towards encapsulation, and aromatic planar molecules with metallic cores which make them more difficult to create hybrids with nanotubes by exohedral functionalization.

3.1 The effect of curvature upon the reactivity and binding capability of SWNTs

It is well known that graphite is formed from a large number of individual graphene layers stacked one on top of each other. The graphene layers are held together by weak van der Waals interactions between the individual sheets. It is the π bands of graphene which are responsible for this interaction and it is known as π-π stacking [28]. In an ideal sheet of graphene the reactivity of the upper and lower surfaces are equivalent. In carbon nanotubes, however, the situation is more complicated because the curvature of the nanotube side-walls has a significant effect upon the reactivity of the nanotube.

Two parameters directly linked to the intrinsic curvature of nanotube side-walls and hence to their reactivity are the pyramidalization angle (θ_{P}) and the π-misalignment angle (ϕ) [29].

Geometrically speaking, carbon nanotubes are significantly different from graphene. The sp^2-hybridized carbon atoms in an ideal graphene sheet are all perfectly trigonal, that is, the angle between the π orbitals and the σ bonds is exactly 90°. In contrast, in carbon nanotubes the curvature of the nanotube side-walls causes the natural trigonal geometry to become distorted. The extent of the distortion can be understood in terms of the pyramidalization angle, which is defined as follows:

$$\theta_{\mathrm{P}} = (\theta_{\sigma\pi} - 90^{\mathrm{o}}), \tag{3.1}$$

where $\theta_{\sigma\pi}$ is the curvature induced deviation angle between the upper π orbital and the σ orbitals [29]. The pyramidalization angles of graphene and a generic SWNT are compared in Figure 3.1 (a) and (b) respectively.

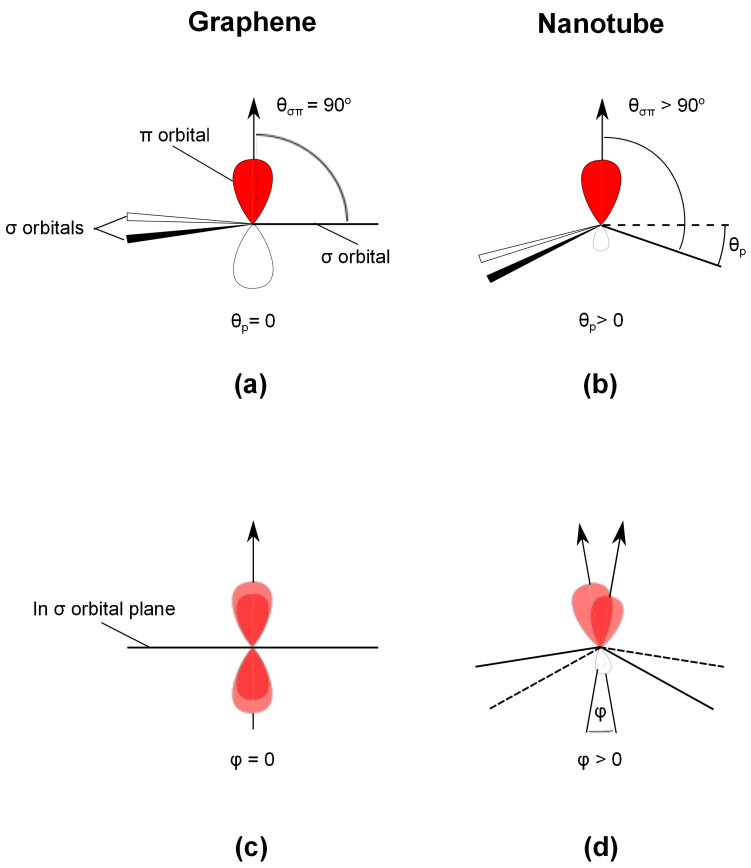

Figure 3.1: Diagrams of the pyramidalization angle θ of (a) graphene and (b) of a generic nanotube, respectively; the π misalignment angle ϕ of (c) graphene and (d) a generic nanotube respectively (adapted from [29]).

Another distortion introduced by the curvature of the nanotube is the mis-alignment of the π-orbitals between adjacent carbon atoms in the nanotube side-walls, this mis-alignment is only present in carbon atoms which have a C-C bond that is not parallel to the circumference of the nanotube.

In the planar geometry of graphene the π-orbitals between the carbon atoms are parallel. However, in a nanotube, the curvature of the walls is such that this is not always the case and an orbital mis-alignment angle ϕ develops. A comparison between the mis-alignment angles of graphene and a generic nanotube is given in Figure 3.1 (c) and (d).

The pyramidalization and misalignmentof the π-orbitals of the C atoms in the sidewalls of the SWNTs induces local strain and as such the exterior surface of carbon nanotubes is expected to be more chemically reactive than the surface of a graphene sheet [29]. Both of these effects, and hence the local strain in the nanotube, are inversely proportional to the diameter of the nanotube [29].

The exterior of SWNTs is also expected to be more reactive than the interior. This is because the pyramidalization of the nanotubes C atoms causes the exohedral lobes of the π-orbitals to be larger than those of the interior [30]. The larger lobes on the exterior favour overlap with chemically suitable atoms or molecules - the reduction in local strain provided by such an interaction also plays a part [30]. The difference between the reactivities of the exterior and interior increases with increasing pyramidalization angle and decreases with increasing diameter. However, the differences are only moderate for typical examples such as (10, 10) SWNTs with diameters of 1.4 nm [30].

3.2 Effects of curvature upon molecular adhesion

The curvature of the sidewalls of SWNTs make the interior and exterior surfaces different geometrically. The nanotube sidewalls curve away from an adatom / molecule attached externally and towards an adatom/ molecule attached internally. This has a strong effect on placement of adatoms / molecules adsorbed onto the internal and external surfaces of nanotubes.

The simplest model which gives qualitatively correct results for specific cases of adatom-nanotube binding energy is the empirical Leonard-Jones potential (LJP) which describes dispersive interactions between neutral atoms. This empirical model has been successfully applied to a number of graphitic materials. For a C_{60} molecule interacting with CNTs, the binding energy was found to be dependent upon molecule placement [31].

For C_{60} molecules interacting with nanotubes, the binding energy to the interior surfaces of the nanotube was found to be greater than when attached to the exterior or to the open ends of the nanotube [31]. The greatest binding energy was found for C_{60} molecules interacting internally with the hemispherical end caps of a nanotube [31]. This can be understood in terms of geometry matching - the closer the geometric match between the molecule and nanotube surface, the greater the number of atoms available to contribute strongly to the binding potential [32] - this is shown schematically in Figure 3.2.

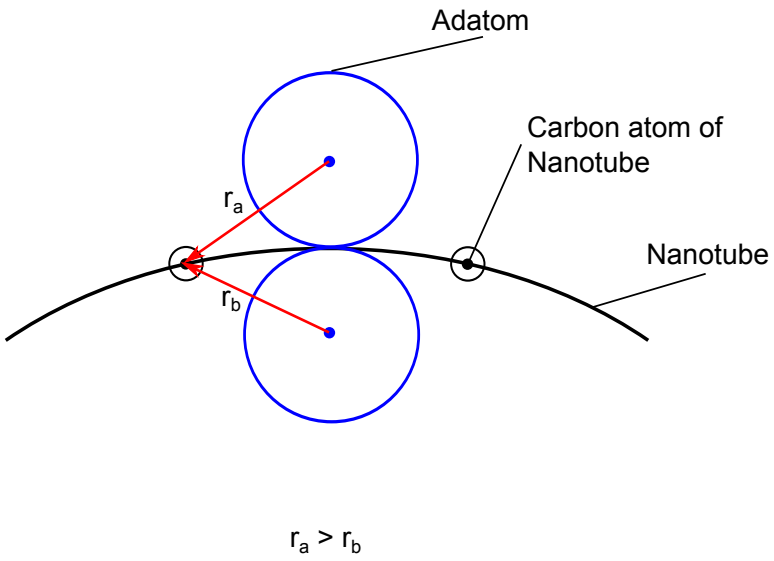

Figure 3.2: Schematic diagram of the geometric match between adatoms attached to the exterior and interior walls of a nanotube. r_a and r_b represent the distances between the centers of the adatoms and the carbon atoms in the walls of the nanotube.

To determine the binding energy between a molecule and nanotube, the binding energy between the molecule and the carbon atoms of the nanotube are summed; the potential energy of interactions between the molecule and a single carbon atom in the nanotube,V_{LJ} is described by the empirical relation

$$V_{\mathrm{LJ}} = 4\epsilon \left[\left(\frac{\sigma}{r}\right)^{12} - \left(\frac{\sigma}{r}\right)^{6} \right], \tag{3.2}$$

where r is the distance between the molecule and the individual carbon atom, ϵ is the depth of the potential well and σ is the hard-sphere radius of the molecule [5]. For example, calculations using a LJP model show that in interactions between adatoms and nanotube bundles the relative size of nanotube diameter and the van der Waals radius of the adatoms is critical in determining uptake of adatoms from the gas phase. As one would expect, small enough molecules can easily fit inside both the nanotubes and in the interstitial channels between tubes. There will be limits depending upon individual adatom species and nanotube diameter beyond which adatoms will not fit inside either space [33].

To reveal qualitative behaviour of an adatom interacting with a nanotube, a simplified model using the LJP can be used where an arbitrary adatom of van der Waals diameter S_{vdW} interacts via van der Waals interactions with an arbitrary nanotube bundle made of SWNTs, the diameter of a SWNT being d.

Varying the diameter of the nanotube, has a marked effect on the binding energy between the atom or small molecule and the SWNT upon which it is adsorbed. As $d \to \infty$ (Figure 3.3 (a)), the interaction strength between the adsorbed adatom and the SWNT becomes equivalent for the interior and exterior surfaces. The binding energy for an adatom to the walls of an infinite diameter nanotube is equivalent to that of graphene. As d is decreased the binding energy between the adatom and the exterior of the SWNT decreases.

Conversely, the binding energy between the adatom and the interior surface of the nanotube increases as d is decreased and reaches a maximum binding energy at an ideal diameter (d_{optimum}) specific to each atom or molecule - see Figure 3.3 (b). The ideal diameter for an arbitrary adatom is described by the following relation:

$$d_{\text{optimum}} = S_{vdW} + (2 \times r_{\text{vdW}}), \tag{3.3}$$

where $r_{\text{vdW}} = 0.15$ nm and is the thickness of the nanotubes π-orbitals [34]; S_{vdW} is the hard-sphere radius of the adatom. At the ideal diameter, the binding energy strongly favours the internal site [5]. At larger diameters Figure 3.3 (c) the interior is still favoured but not as strongly as at the ideal diameter, this is due to the differences in size. As d is decreased below d_{optimum} (Figure 3.3 (d)), the repulsive $1/d^{12}$ component of V_{LJ} becomes dominant due the overlap of the π-orbitals of the nanotube and those of the adatom, making encapsulation unfavourable.

From this simple model it is clear that the van der Waals diameter of the atom or molecule relative to the diameter of the nanotube is the most important parameter associated with the placement of the atom or molecule [5].

The molecules used in this study are shown in Figure 3.4 and the effective hard-core diameters (S_{vdW}) of the molecules and the corresponding ideal nanotube diameters d_{optimum} calculated using equation (3.3) are shown in Table 3.1.

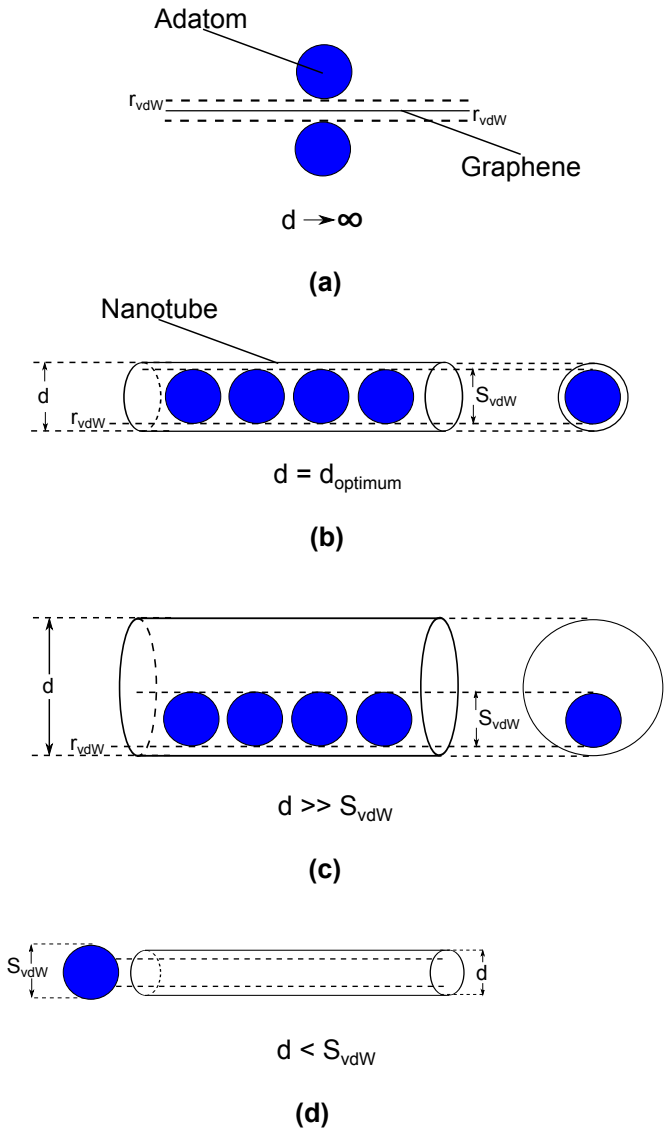

Figure 3.3: Schematic diagrams of adatoms attached to carbon nanotubes with (a) $d \rightarrow \infty$ (b) $d = d_{\text{optimum}}$ (c) $d >> S_{vdW}$ and (d) $d < S_{vdW}$. All symbols as defined in the text.

Cobalt carbonyl ($Co_2(CO)_8$) is a roughly spherical molecule with an effective hard-sphere diameter of 0.5 nm and a corresponding optimum nanotube diameter of 0.8 nm. The spherical geometry should give this molecule a high interaction energy with the inner walls of the nanotubes. The cobalt carbonyl molecule has a core formed from two paramagnetic cobalt atoms.

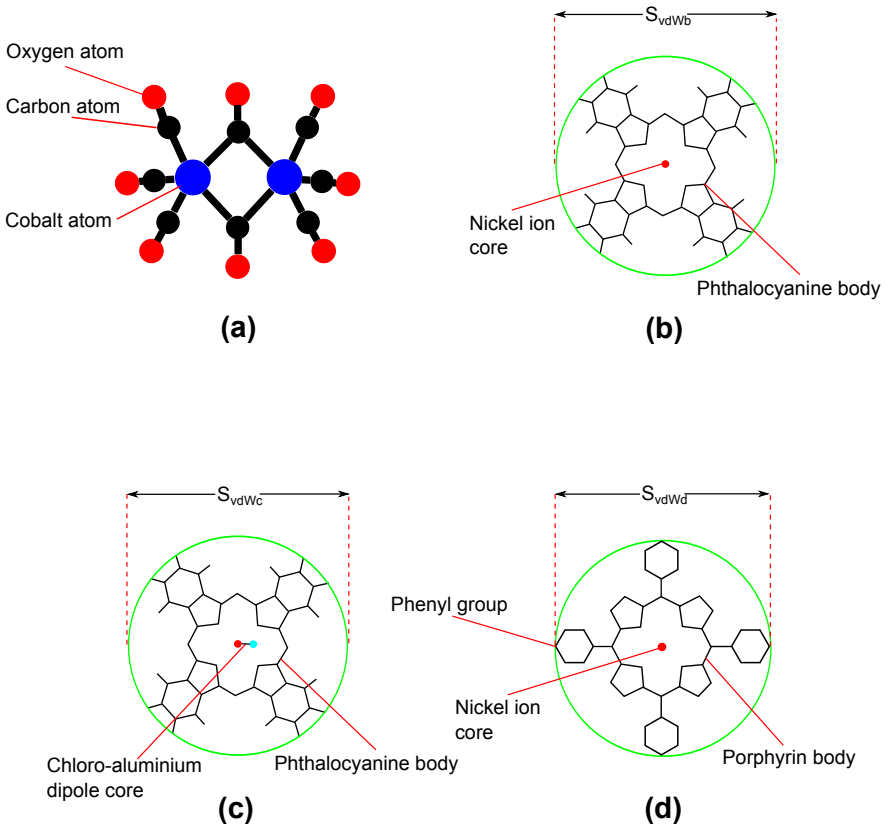

Figure 3.4: Schematic diagrams of the molecular strutcure of (a) Cobalt carbonyl ($Co_2(CO)_8$) (based upon [35]) (b) nickel phthalocyanine (NiPc) (based upon the structure of CoPc [36]), (c) chloro-aluminium phthalocyanine (ClAlPc) and (d) nickel tetraphenyl porphyrin (NiTPP) (based upon [37]). The green rings around the square TPP and Pc molecules represent the van der Waals diameters of the molecules.

In contrast, the other molecules used in this study are significantly larger, planar in nature and roughly square shaped. In order to obtain an effective hard-core diameter for these molecules, a circular symmetry has been assumed - see Figure 3.4. Both of the phthalocyanine (Pc) molecules, chloroaluminium Phthalocyanine (ClAlPc) and nickel Phthalocyanine (NiPc) molecules share the same structure and hence have the same effective hard-core diameter of 1.5 nm with an associated ideal nanotube diameter of 1.8 nm. However, they have dissimilar cores: NiPc has a paramagnetic nickel ion at its core, while ClAlPc has a Cl-Al dipole, which forms an electric dipole. The nickel tetra phenyl porphyrin (NiTPP) molecule is the largest of the set, possessing an effective hard-core diameter of 2 nm and an associated ideal nanotube diameter of 2.3 nm. It has a nickel ion at its core, as with the NiPc molecule, however, NiTPP has a porphyrin body with phenyl appendages attached.

Molecular species	S_{vdW} / nm	d_{optimum} / nm
$Co_2(CO)_8$	0.5	0.8
ClAlPc	1.5	1.8
NiPc	1.5	1.8
NiTPP	2.0	2.3

Table 3.1: The optimum nanotube filling diameters d_{optimum} for the molecules used in this study, S_vdW is the size of the molecules inluding the van der Waals radii of the constituent atoms. The sizes of the van der Waals potential surface of the Pc molecules were based upon that of cobalt phthalocyanine (CoPc) as quoted by [36]. Those of the NiTPP and $Co_2(CO)_8$ molecules were determined from molecular models.

Taking symmetry into account, the LJP interaction between these molecules and the inner surfaces of the nanotubes would be maximised if the molecules were arranged cross-ways along the axis of the nanotube - Figure 3.5 shows this schematically using the NiTPP molecule as an example. Given the square geomtery of the molecules they are likely to have a weaker LJP interaction than the cobalt carbonyl interaction - this would result from greater symmetry mis-match. However, this is not the geometry observed upon encapsulation (see chapter 5 section 5.4).

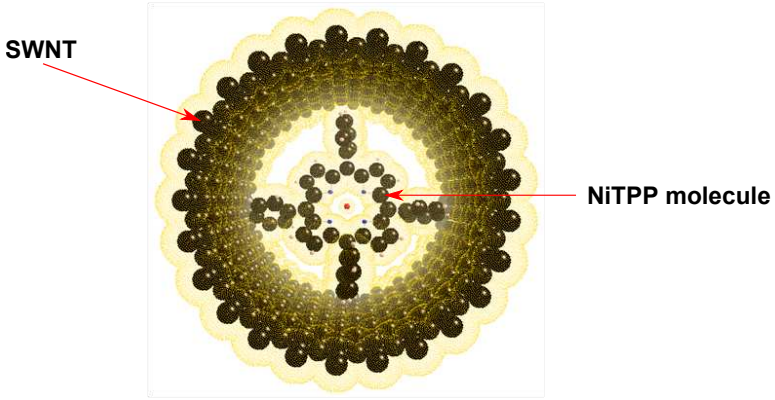

Figure 3.5: Schematic diagram showing a NiTPP molecule positioned in a SWNT arranged cross-ways to the length of the nanotube (based upon [38]) The yellow outline represents the van der Waals surfaces of the molecule and nanotube.

3.3 Aromatic interaction between molecules and the exterior of CNTs

For aromatic molecules it is possible for intermolecular interactions to occur through π stacking. In π stacking, the planar π systems of aromatic molecules lay one on top of each other, in a nearly parallel orientation [20].

The cobalt carbonyl molecule is not aromatic and as such cannot interact in this way. The other molecules of this study, however, posses multiple aromatic sub-structures which could enable π stacking to occur with the nanotubes exterior as well as between themselves. The aromatic molecules are shown in Figure 3.6 (a) and (b) with the structures likely to result in π stacking highlighted.

The TPP and Pc molecules have two possible sub-structures where π stacking between the molecule and surfaces of the nanotube could occur:

(i) the central ring systems

(ii) the benzene-like appendages attached to the central ring systems

Taking the porphyrin molecule as an example, the possible binding areas for the sub-structures on a nanotube of 2.3 nm in diameter is shown in Figure 3.6 (c) and (d). The porphyrin is also shown encapsulated inside of the nanotube, however, given that the molecule is separated from the inner walls of the nanotube, it is unlikely that π stacking would occur - unless the molecule were to be distorted to more closely match the geometry of the nanotube.

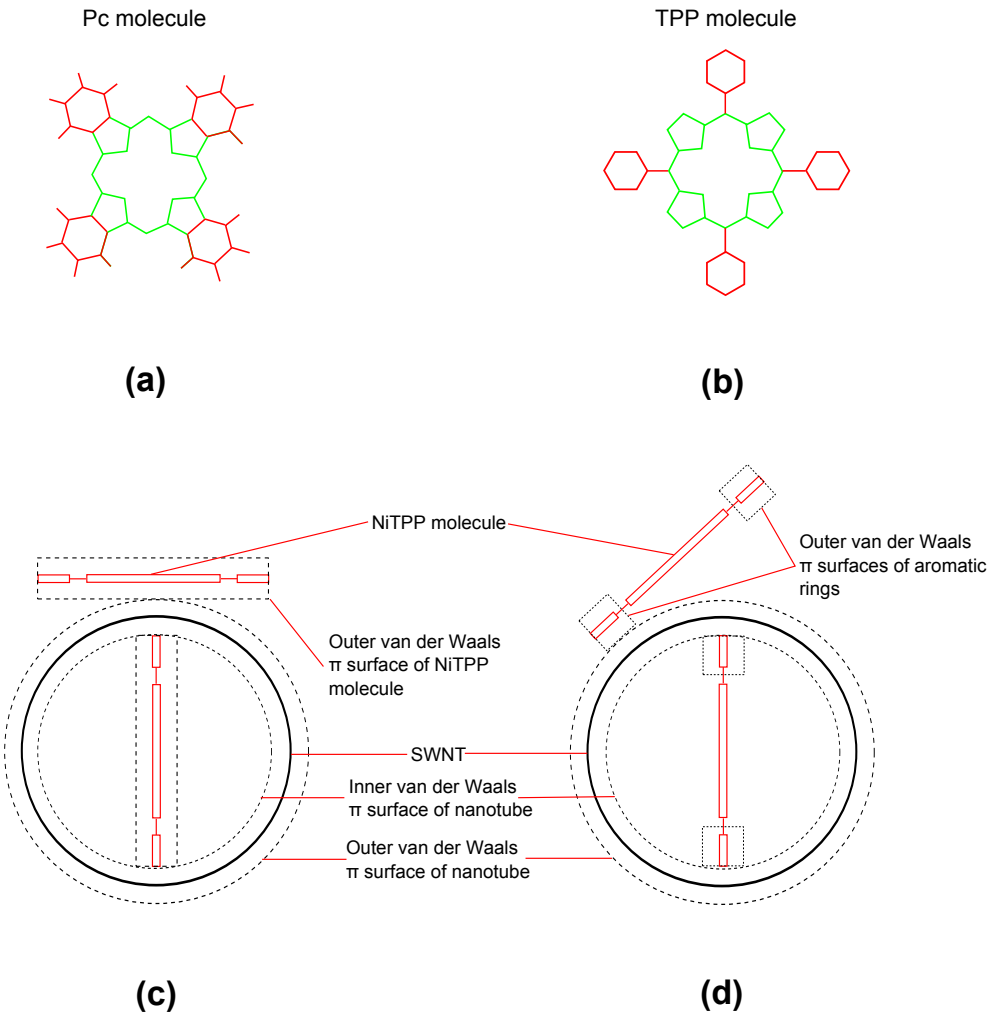

Figure 3.6: Schematic diagram showing the (a) Pc and (b) TPP molecules respectively. The structures likely to be involved in π stacking are highlighted in red, appendages and green, central ring system. (c) and (d) show the possible binding areas on a nanotube for a fully aromatic porphyrin molecule (c) and (d) where the aromacity of the central ring has been destroyed by chelation with a metal ion.

It has been found that un-chelated porphyrins (porphyrins without a metal centre), for example tetraphenyl porphyrin (TPP) shown in Figure 3.6 (b), show strong affinities for the exterior of semiconducting CNTs, so much so that the union of the two can be used to separate semiconducting nanotubes from a metallic/ semiconducting mixture [39]. However, upon chelation with a metal ion complex, the binding between metallo-Porphyrins and nanotubes becomes less favourable [39]. This highlights that the primary centre for the binding of the un-chelated TPP to the SWNT is the porphyrin ring system (Figure 3.6 (c)) and not the phenyl groups.

This also seems to be true for Phthalocyanine molecules in which upon the formation of a coordination bond between a metal ion and the nitrogen atoms, aromaticity of the central ring system is destroyed and thus π stacking via it is prevented [40]. In conclusion, the attachment of either the NiTPP, NiPc or ClAlPc molecules to CNTs via π stacking involving the centres of these systems seems unlikely.

The binding energy of aromatic molecules adsorbed to the exterior of CNTs by π stacking has been found to be weak for benzene-like molecules. However, if charge transfer between the nanotube and molecule occurs, the binding energy can be significantly higher [41]. It is well established that metalloporphyrins are electron donating systems [19], therefore this may present a route through which π stacking could occur between the appendages of the molecules and graphitic surface of the CNT (Figure 3.6 (d)). We finally note that in reference [42] CoOEP molecules were found to exohedrally functionalize SWNTs in high yield despite the presence of the metallic core.

3.4 Effects of curvature upon molecule diffusion on and in SWNTs

Calculations of the potential energy and molecular dynamics with a Leonard-Jones type potential found that both the curvature and helicity of the a carbon nanotube have a great bearing on the diffusion of an adatom adsorbed onto the nanotube walls [43]. It was found that adatom diffusion is very dependent upon the curvature of the nanotube. The diffusion barrier increases monotonically with curvature [43].

Therefore it is possible to conclude that diffusion along the interior of the nanotube (negative curvature) is easier than along graphite (zero curvature), however diffusion along a flat surface is easier than along the exterior of the nanotube (positive curvature). This can be understood in terms of curvature induced strain in the walls of the nanotube, the inner surface experiencing a negative strain (compression) and the exterior experiencing positive strain.

The helicity has also been shown to impact upon the diffusion path of an adsorbed adatom, with diffusion being favoured in armchair rather than zig-zag nanotubes [43]. With these considerations in mind it is reasonable to conclude that the interior of the nanotube is a more suitable environment for the formation of ordered nanostructures than the exterior.

Calculations have shown that due to a smoother potential energy surface in the interior of nanotubes, the barrier to diffusion is lower than that of the exterior surface even though the binding energy endohedrally is greater [43]. This makes the diffusion of adatoms through the interior of the nanotube much more favourable than along the exterior. Once the adatoms are inside, for adatoms of or near optimum size for the nanotube, the increase binding energy inside makes the removal of encapsulated adatoms demanding energetically.

3.5 Molecular encapsulation by SWNTs

3.5.1 Encapsulation methods

For filling carbon nanotubes with molecular species more traditional methods used either thermal diffusion [44] or filling from solution [5, 15, 45, 46].

Thermal diffusion of C_{60} fullerenes has been shown to produce SWNT filling yields of up to 85%. However, to achieve this result, a temperature of 650^o C was required [44]. The decomposition temperatures of a lot of organic molecules of similar size to C_{60} are far below this, indeed the cobalt carbonyl molecule is known to decompose above a temperature of 52^o C [47]. Therefore, the high temperatures necessary for this process to occur make it especially unsuitable for the encapsulation of molecules such as this. Porphyrins however, have a much greater thermal stability and enter the molten phase at temperature of 200 - 300^o C [48]. Results indicate that porphyrin peapods can be formed using a thermal diffusion method with a process temperature of 400^o C. [44]. Phthalocyanine molecules also possess a high degree of thermal stability - for example, the NiPc molecule is known to be stable in Ar up to a temperature of 750^o C [49].

Therefore, a thermal diffusion method may be suitable for the porphyrin and phthalocyanine molecules but might not be compatible with the cobalt carbonyl molecule. Nevertheless, the larger the molecule (e.g. the NiTPP molecule used here), the more difficult its encapsulation by thermal diffusion [5].

A number of studies have been conducted upon filling from solution using a variety of organic solvents, both aromatic, such as toluene, and polar, such as ethanol - these met with mixed results [5, 15, 45, 46]. The main advantage of filling by solution is that it is a relatively low-temperature process and therefore suitable for thermally unstable molecules.

In order to maximise the yield of encapsulated molecules upon filling from solution there are a number of criteria which must be optimised [5]:

(i) The solvent used must have a surface tension (γ) which is low enough to wet the surfaces of the CNT.

(ii) The interaction between the solvent and the solute (molecules to be encapsulated) must be weak.

(iii) The interaction between the solvent and the CNT must also be weak.

(iv) The interaction between the CNT and the solute must be relatively strong.

(v) The critical diameter of the solvent molecules should be small enough for them to escape from any encapsulated structure which has formed using the filling process.

It has been found that a solution's ability to effectively wet the surface of the nanotube is critical to whether it will induce molecular encapsulation [50]. The parameter which has the greatest effect on a solvent's ability to wet the surface of a CNT is the surface tension (γ), with the wetting threshold for CNTs being between 100 and 200 mNm^{-1}[50]. Wetting with liquids with a surface tension greater than the threshold is impossible.

It has been found that fluids with high surface tensions such as molten metals are not successfully encapsulated inside CNTs except when forced to do so by the application of very high pressures. Low surface tension solvents have been found to effectively wet CNT and to be drawn into the interior of the nanotube by capillary forces either via the open ends of the nanotubes or through wall defects [50].

The nanotube wetting threshold is high enough that they are expected to be wetted by water ($\gamma \sim 72$ mNm^{-1}) and most organic solvents ($\gamma \sim 72$ mNm^{-1}) [51]. The solubility of C_{60} and the relevant properties of some solvents which have been used in nanotube filling experiments are shown in Table 3.2. All of these solvents possess surface tensions low enough to effectively wet carbon nanotubes and enter into the interior, however, supercritical carbon dioxide ($ScCO_2$) has no surface tension at all.

Solvent	Solubility of C_{60} / gL^{-1}	Critical diameter of solvent molecule / nm	Surface tension, γ at 20 ^{o} C / mNm^{-1}
Toluene	2.800	0.78	28.52
Ethanol	0.001	0.44	22.39
Chloroform	0.160	0.33	27.32
n-Hexane	0.043	0.92	18.40
$ScCO_2$	Unknown	0.28	0.00

Table 3.2: C_{60} Solubility, critical diameter and surface tensions of selected solvents [52–54].

It has been found that if a CNT is filled with a gas such as air - this will oppose entry of liquid to the CNTs even if the liquid has a sufficiently low surface tension to allow wetting of the tube [51].

To counteract this, it is necessary to provide the existing fluid with an escape route such as the open ends of the nanotube or wall defects [51]. It is also important that the solvent molecules once inside the nanotubes are small enough to escape after the filling molecules have been encapsulated, specifically they will have to fit through the defects in the nanotube side-walls and around any pea-pod structures which have been formed. CO_2 with its linear form, has the smallest critical diameter of any of the molecules listed in the table and therefore should have the greatest chance of escaping from filled nanotubes.

The strength of the interaction between the solvent and the molecules to be encapsulated can greatly affect the probability of encapsulation being successful. If the solvent has a particular affinity for the molecule, as is the case when C_{60} is solubilised in toluene, then the binding energy between the solvent and solute can be so strong that encapsulation by the nanotube becomes unfavourable [46]. In this instance the molecules will remain in solution and be carried away from the nanotube. While the solubility of C_{60} in $ScCO_2$ is not known it is expected to be low, but non-zero [55].

It is clear that with the above criteria in mind that the properties of $ScCO_2$ make it the ideal solvent for filling from solution experiments. Indeed, it has been shown to be very effective in creating fullerene-CNT peapods [15]. While the porphyrin and phthalocyanine molecules used in this study are different from C_{60} geometrically, they share an aromatic structure. With this in mind it is reasonable to assume that the above consideration should apply to them also.

3.6 Molecular encapsulation by SWNTs using a $ScCO_2$ medium

3.6.1 Supercritical fluids

A gas is characterised as having a low density, a low viscosity and a high diffusity. In contrast a liquid has a relatively high density, a high viscosity and a low diffusity. There is a third fluid phase which has properties intermediate to those of liquids and gases; this is called a supercritical fluid (SCF). Table 3.3 shows the contrasting properties of the different fluids.

All supercritical fluids have a certain point in the phase space, characterised by a critical temperature, T_c and a critical pressure, P_c at which they make a transition from a normal fluid to a supercritical fluid; some examples are shown in Table 3.4.

Phase	Density / 10^3kg m^{-3}	Viscosity / mPas	Self diffusion coefficient / $10^4 m^2 s^{-1}$
Gas	(0.6 - 2) $\times$ 10^{-3}	(1 - 3) $\times$ 10^{-2}	0.1 - 0.4
Supercritical fluid near to T_c	0.2 - 0.5	(1 - 3) $\times$ $^{-2}$	0.7 $\times$ 10^{-3}
Liquid	0.6 - 1.6	0.2 - 3	(0.2 - 2) $\times$ 10^{-5}

Table 3.3: The properties of fluids [56]

Fluid	Critical temperature, T_c / ° C	Critical pressure, P_c / Bar
Helium-4	-268.0	2
Oxygen	-118.6	50
Carbon dioxide	31.0	74
Propane	96.7	42

Table 3.4: Selected supercritical fluids and corresponding critical temperatures and pressures [57].

At this critical point (T_c, P_c) the boundary between the liquid and gas phases ceases to exist and the liquid and gas densities become equal. Above this point the fluid does not condense to form a liquid or evaporate to form a gas, instead it has properties somewhere between the two [56]. Figure 3.7 shows the phase diagram of a single substance. Following the liquid-gas coexistance curve from the triple point (T) to the critical point (C), both the temperature and pressure of the fluid increases. The increase in temperature results in thermal expansion of the liquid and as a result a decrease in density, while the increase in the pressure results in an increase in the gas density.

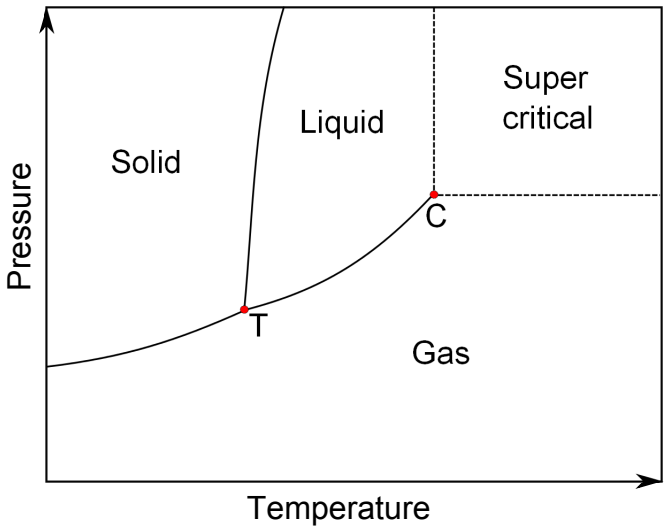

Figure 3.7: Schematic diagram of the phases of a single substance (based upon[56]).

The fluid densities continue to converge until the critical point is reached. At this point the densities equate and the liquid and gas phases become indistinguishable [56]. With the disappearance of the barrier between the gas and liquid phases, all inter-fluid surface tension is lost and the fluid enters a supercritical phase.

The solvent power of a supercritical fluid is very sensitive to density fluctuations, especially around the critical point. This means that relatively small changes of pressure or temperature near to the critical point can be used to tune the solvent power of the fluid. The low density and non-existent surface tension of supercritical fluids make them an attractive prospect for filling carbon nanotubes.

The critical temperatures and pressures of a selection of substances are shown in Table 3.4. When deciding upon which substance to use in a supercritical fluid experiment there are a number of practical factors to consider - arguably the two most important are the temperatures and pressures of the critical point. For example both oxygen and Helium 4 enter a supercritical phase at relatively low pressures, but require cryogenic temperatures to come near to the critical point. Substances exist which have critical points higher in both temperature and pressure, however, they tend to be dangerous - for example at its critical point propane is flammable and potentially explosive.

The substance most commonly used in supercritical fluid processes is carbon dioxide. It has a critical pressure of 74 bar, well in range of modern high pressure systems, and a critical temperature of 31.0 ^{o} C. These values are such that CO_2 can be maintained in the supercritical phase for an extended period using relatively simple equipment with a low risk of adverse effects. The low critical temperature of CO_2 is especially useful when dealing with temperature sensitive materials. Another useful characteristic of supercritical CO_2 is that it is chemically inert. This is important when using materials sensitive to oxidation, such as the cobalt carbonyl molecule. Carbon dioxide is also non-flammable, non-toxic, inexpensive and environmentally acceptable [57].

3.7 $ScCO_2$ induced encapsulation

Previous work [15] found that fullerenes of various sizes could be encapsulated inside SWNTs using $ScCO_2$ as a medium. In these studies the greatest yield of encapsulated fullerenes was achieved when the $ScCO_2$ was kept at a constant temperature of 50° C and the pressure was cycled between a pressure of 100 and 150 bars [15].

There are a number of factors that can determine the filling yield and below is provided the rationale for the initial choice of the $ScCO_2$ parameters used for filling experiments.

The encapsulation process relies upon the solvent power of the $ScCO_2$ which depends upon the density of the fluid. Figure 3.8 shows that the density of a supercritical fluid is very sensitive to changes in temperature and pressure near to the critical temperature, $T_c = 31°$ C. The temperature of 50° C used in the experiments of this study was such that the change in density is fairly fast, but not as abrupt as near to T_c. For example, if T was increased to a value that is significantly higher than T_c, for example over 100 ° C, the change in density is more gradual, but it is also significanly less dense - this would result in the fluid becoming more gas-like and adversely affect the effectiveness of the fluid as a solvent, as well as adversely affect the filling experiment. In contrast, if T is reduced below T_c the CO_2 will leave the SCF (supercritical fluid) state and re-enter the liquid phase, this would be disasterous for a filling experiment. By changing the pressure of the fluid while keeping the temperature fixed, it is possible to vary the density of the fluid in a controlled way such that one of the isotherms is followed.

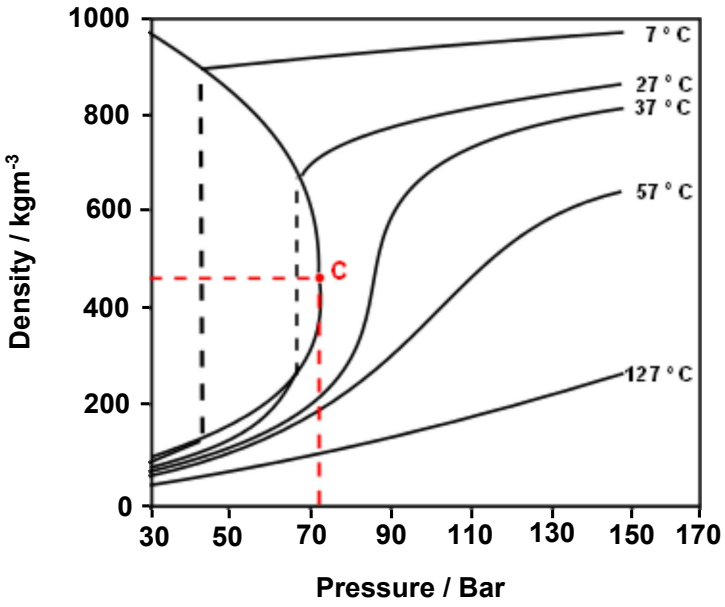

Figure 3.8: Schematic phase diagram of CO_2 [56]. C is the critical point.

While the density of the fluid increases with pressure, the interaction between the CO_2 and the filling molecules does not vary in a straightforward fashion. Figure 3.9 shows that at low densities (A), the interaction is weakly attractive. As the density of the fluid is increased, a point (B) will be reached at which the attractive interaction is maximised.

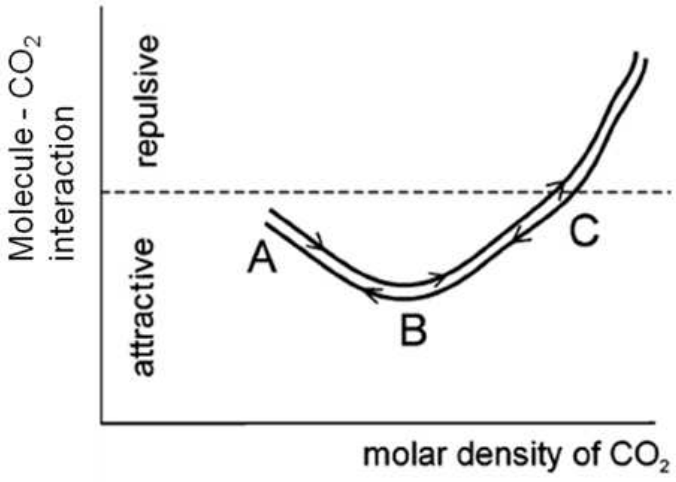

Figure 3.9: Dependency of the solute to solvent interaction as a function of supercritical fluid CO_2 density. The arrows indicate alternating cycle direction (adapted from [15]).

At this point the interaction is such that a thick shell of CO_2 molecules will form around the filling molecule (Figure 3.10 (a)). If the density is increased further, the interaction will become increasingly less attractive and eventually will become repulsive at (C). The repulsive effect will result in a CO_2-deficient region around the filling molecule (Figure 3.10 (b)). This interaction is consistent with a van der Waals type potential, the density of the fluid controlling the distance between the CO_2 and filling molecules. By ramping the pressure of the solution in this way it is possible to selectively tune the solvent-solute interaction. When the pressure is cycled, the above processes are repeated multiple times resulting in a higher filling yield.

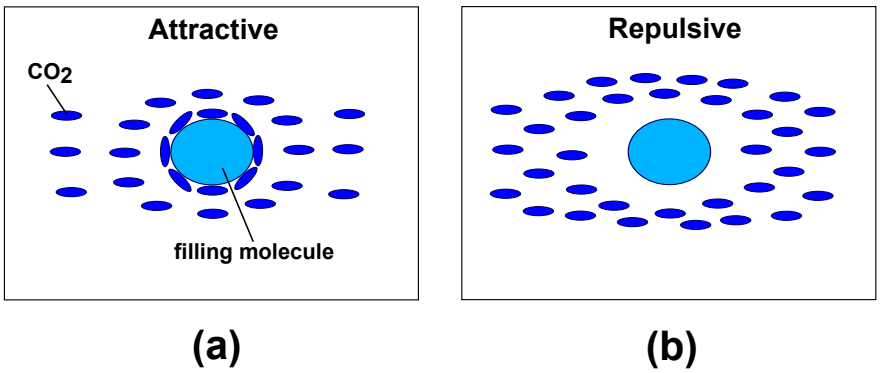

Figure 3.10: Schematics showing (a) attractive, and (b) repulsive interaction between $ScCO_2$ solvent molecules and a solute (filling) molecule.

Further, information from previous work [15] shows that pressure-cycling experiments produce much higher yields of encapsulated C_{60} molecules when compared to static exposures of equal duration [15]. In a pressure cycling experiment, the cycle shown in Figure 3.9 is repeated a number of times.

In the specific case of a solution of CO_2 and C_{60} molecules, following the curve from A to B, the inter-molecular interaction becomes increasingly attractive until a CO_2 density of $\approx$ 440 - 620 kg/m^3, i.e. at 85-95 bar for 40 °C is reached at point B [55,58]. This attractive interaction causes solubilisation of the filling molecules by the supercritical solvent (see part (a) of figure 3.10), and allows them to be carried inside the nanotube. Inside the nanotubes, the molecules will be irreversibly encapsulated.

Increasing the pressure further from B to C results in the interaction becoming increasingly less attractive and eventually negative at C $\approx$ 750 kg/m^3 (above 125 bar at 40 ^{o}C) is reached at point C [55, 58]. The repulsive nature of the interaction at high pressure causes the solvent to release the molecules (see part (b) of Figure 3.10). The solvent should now decouple from the solute and leave the nanotubes. The range of pressures used in the current investigation (100-150 bar) is consistent with this scenario.

Finally, there are some more general considerations regarding the filling process. Due to the larger area of interaction between the encapsulated molecules and the nanotube inner walls, their interaction energy can be very high and can result in irreversible encapsulation inside the tubes.

In contrast, the interaction energy between the CO_2 and the nanotube is much less, and this makes their trapping much less likely: the small diameter of the CO_2 molecules, of only 2.8 Å, allows them to diffuse around the filling molecules, and leave the nanotube through the open nanotube ends or side wall defects in the tube.

Chapter 4

Production of hybrids of nanotubes and organo-metallic molecular systems

This chapter describes the supercritical CO_2 instrumentation and processes developed and implemented in order to encapsulate the chosen organo-metallic systems. This resulted in two variants, a primary one, suitable for air-stable compounds, and another designed for dealing with air-sensitive systems. Preparation procedures applied to the carbon nanotubes prior to the supercritical fluid encapsulation processes, and associated characterisation are also described. Finally, a protocol for the exohedral functionalization of carbon nanotubes is also given.

4.1 Synthesis of carbon nanotubes

The three methods of carbon nanotube synthesis most commonly employed are laser vaporization, arc discharge and carbon vapour deposition (CVD). Each method is quite different and tends to produce SWNTs with different average diameters with different diameter distribution widths and different levels of impurities.

For the experiments in this study a synthesis method which produces a broader diameter distribution is desirable. This is because while the theory discussed in the previous chapter provides an estimate for the optimum filling diameters for each molecule, they are not exact. A broader diameter-distribution should increase the probability of the optimum diameter for each molecule being present in the nanotube samples and provide the opportunity of forming new supramolecular architectures.

4.1.1 Laser vaporization

In the laser vaporization method graphite containing a small amount of embedded transition metal catalyst particles is vaporized using a pulsed laser and condensed into SWNTs. This method tends to produce relatively small amounts of SWNTs and the diameter distribution curve tends to be very narrow [3]. This method would be very useful in experiments where a specific nanotube diameter is desired.

4.1.2 Arc-discharge

One of the most commonly used methods of nanotube growth, in the arc-discharge - method a voltage is applied across two graphite rods separated by a ≈ 1 mm gap. In order to grow single-walled nanotubes, it is necessary to embed catalyst particles in the graphite rod which acts as the cathode - it is upon these particles that the nanotubes grow. The catalyst particles are usually nanoparticles of transition metals such as Co, Ni or Fe [3]. In addition to nanotube deposition, fullerenes and amorphous carbon are also deposited onto the cathode at the same time [3]. The arc discharge method is a high temperature process which requires temperature of ≈ 3000 ^{o} C [3]. The exact properties of the nanotubes that are grown by this method will depend upon the conditions used; however, in general, the average diameter of the nanotubes and the width of the distribution curve tends to be small. The arc-SWNTs used in the experiments of this study were commercially grown by Nanoledge^{TM} and they have an average diameter of 1 nm.

These nanotubes were chosen because their average diameter matches well with the expected optimum diameter (0.8 nm) of the cobalt carbonyl molecules as discussed in the previous chapter.

An example of a nanotube diameter distribution obtained using the arc-discharge method is shown in Figure 4.1 [59]. This distribution shows that although more nanotubes were produced with a diameter of $\approx$ 1.05 nm, a significant fraction were produced which have diameters close to the peak diameter. The diameter distribution is skewed to the left of the peak diameter, favouring narrower nanotubes. This tendency would increase the number of nanotubes with the optimum encapsulation diameter for the cobalt carbonyl molecule and hence could result in an increase in filling yield.

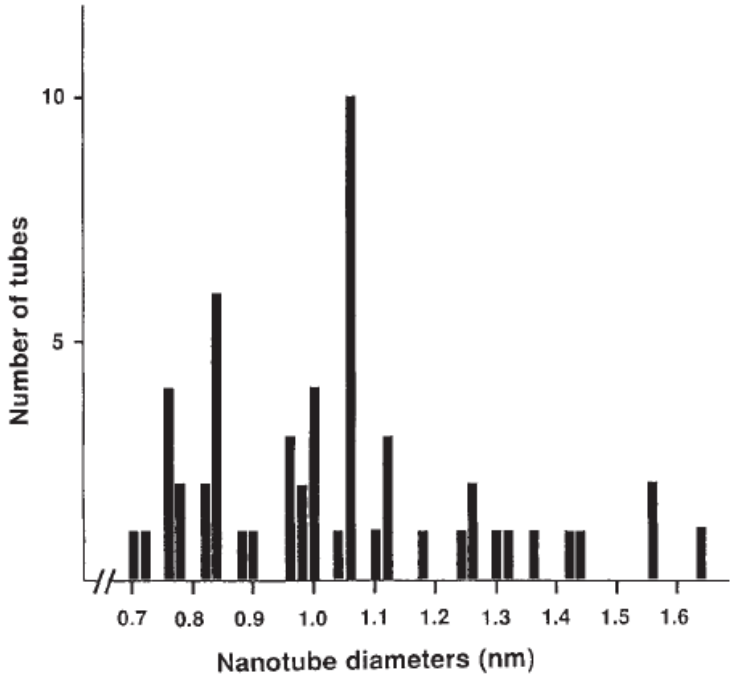

Figure 4.1: A histogram showing the number of nanotubes produced as a function of nanotube diameter for an arc-discharge method using an Fe catalyst [59].

4.1.3 Carbon vapor deposition

The carbon vapor deposition process uses a lower temperature than the arc synthesis method. In this method a gas of carbonaceous material is passed over catalyst nanoparticles, usually of transition metals which are kept at a temperature of $\approx$ 1000 °C in a reaction tube [3]. The CVD method tends to produce SWNTs with larger diameters and broader diameter-distributions than the arc method. Due to the lower temperature, the nanotubes also tend to have a larger density of defects in their structure [3]. In addition to the usual amorphous carbon and catalyst particle impurities, the CVD process tends to result in a greater number of double and multi-walled nanotubes being produced. The CVD nanotubes used in this study were sourced from Nanocyl^{TM}. They have an average diameter of 2.0 nm [60] - this is consistent with the approximate optimum filling diameter of the porphyrin and phthalocyanine molecules.

Figure 4.2 shows the diameter distribution for SWNTs grown by the CVD method using Fe_2O_3 nanoparticles as a catalyst [61] - used here for qualitative comparison with the Nanocyl nanotubes. Comparing Figure 4.2 with Figure 4.1, it can be seen that the diameter distribution obtained by the CVD method is broader than that produced by the arc-discharge method. The greater breadth of CVD distributions means that there should be a significant number of nanotubes with diameters slightly greater and slightly lesser the peak diameter - this should result in there being an ample supply of nanotubes with diameters near to the optimum filling diameters of the porphyrin (2.3 nm) and phthalocyanine (1.8 nm) molecules used in this study.

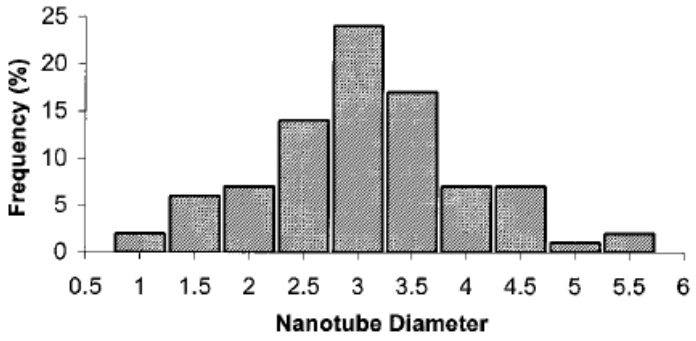

Figure 4.2: A histogram showing the number of nanotubes produced as a function of nanotube diameter for an CVD method using an Fe_2O_3 catalyst [61].

4.2 Purification of carbon nanotubes

4.2.1 Impurities

As-grown carbon nanotubes typically possess a number of impurities, which in the case of CVD-grown nanotubes, can amount to as much as 30 % of the batch material [60]. These impurities are composed of particles of amorphous carbon, residual metallic catalyst particles and carbon onions. A carbon onion is a metal catalyst particle around which a shell of amorphous carbon has formed. A number of purification methods have been developed to remove these impurities - these methods are now described:

(i) 4.2.2 Thermal oxidation

Thermal annealing in an oxidising atmosphere has been shown to be an effective way to remove amorphous carbon from carbon nanotube batches [62]. In this process the nanotube powder is heated at a temperature in excess of 350^o C in air. This process exploits the weaker disordered bonding in the amorphous carbon structures relative to the strong sp^2 lattice bonding in the nanotubes.

The combination of increased reactivity of the weaker bonds at high temperature and the presence of oxygen in the air results in the amorphous carbon being oxidised and removed as either carbon dioxide or carbon monoxide. This process is effective in removing both amorphous carbon particles and the shells of carbon around the carbon onions (where reactivity is increased due to the high curvature). The main drawback of this process is that it can also damage the nanotubes, especially if the
nanotubes possess defects [63].

(ii) 4.2.3 Hydrogen peroxide-based oxidation

Another process which has been shown to be effective in removing amorphous carbon from as-grown nanotubes is oxidation by hydrogen peroxide (H_2O_2) in solution [63]. In this process the H_2O_2 oxidises the amorphous carbon producing either carbon dioxide or carbon monoxide. This method is less aggressive than thermal annealing and hence will result in less damage to the nanotubes.

(iii) 4.2.4 Acid reflux

A simple and effective method to remove residual catalyst particles is to reflux the powder in concentrated hydrochloric acid (HCl) [64]. The HCl dissolves the metal catalyst particles, but does not attack the nanotubes.

4.2.5 Purification procedures adopted

Using a combination of carbon oxidation and acid reflux processes it is possible to remove a great deal of the impurities from as-grown carbon nanotube batches.

Two purification procedures were adopted for application to the nanotubes batches used in the experiments of this study.

The first was more aggressive, and employed a combination of thermal annealing and acid reflux techniques. Use of this procedure resulted in a substantial reduction of the overall mass of purified nanotubes.

The sequence of steps is as follows:

Purification procedure 1

(i) As-grown nanotubes were heated in a solution of 70% concentrated HCl for one hour at a temperature of 105° C in order to remove any exposed catalyst particles.

(ii) The suspension was then filtered with deionized (D.I.) water under vacuum pumping to dilute and remove the acid and left to dry at 90° C over-night.

(iii) The resulting powder was heated in air for 45 minutes at 450° C to oxidize the amorphous carbon and onion cages.

(iv) The dry powder was heated in a solution of 70 % concentrated HCl for one hour at a temperature of 105° C in order to remove the metallic cores of the carbon onions expsoed by the oxidation process.

(v) The suspension was then filtered with D.I. water under vacuum pumping to dilute and remove the acid and left to dry at 90° C over-night.

Purification procedure 2

The second purification procedure used a combination of the hydrogen peroxide oxidation and acid reflux processes. This procedure results in a milder and more selective purification, and a larger quantity of purified nanotubes is obtained.

The sequence of steps is as follows:

(i) As-grown nanotubes were heated in a solution of 70% concentrated HCl for one hour at a temperature of 105° C.

(ii) The suspension was filtered with D.I. water and enthanol mixture under vacuum pumping and left to dry over-night at 90° C.

(iii) The resulting powder was gently sonicated using a low-powered ultrasonic bath in 30 % concentrated H_2O_2 and then left to stir for one month.

(iv) The suspension was filtered with D.I. water (to dilute and remove any remaining H_2O_2) and enthanol under vacuum pumping and left to dry over-night at 90° C.

(v) The dry powder was heated in a solution of 70 % concentrated HCl for one hour at a temperature of 105° C in order to remove the metallic cores of the carbon onions exposed by the oxidation process.

(vi) Step (ii) was then repeated.

4.3 Characterisation of purified nanotubes

Before filling experiments using the commercial arc (Nanoledge) and CVD (Nanocyl) nanotubes were attempted, the quality of the nanotubes was investigated using transmission electron microscopy (TEM). The TEM images obtained, which are discussed below, made it clear that further purification of the nanotube material was necessary - therefore, both types of nanotube were subjected to purification to remove impurities introduced during the production process.

4.3.1 Characterisation of Arc SWNTs

The Nanoledge arc SWNTs were subjected to purification procedure 1 described above. From the TEM images (Figure 4.3) of the nanotube material before and after purification it can be seen that both the amount of amorphous carbon and the number of catalyst particles are greatly reduced post-purification.

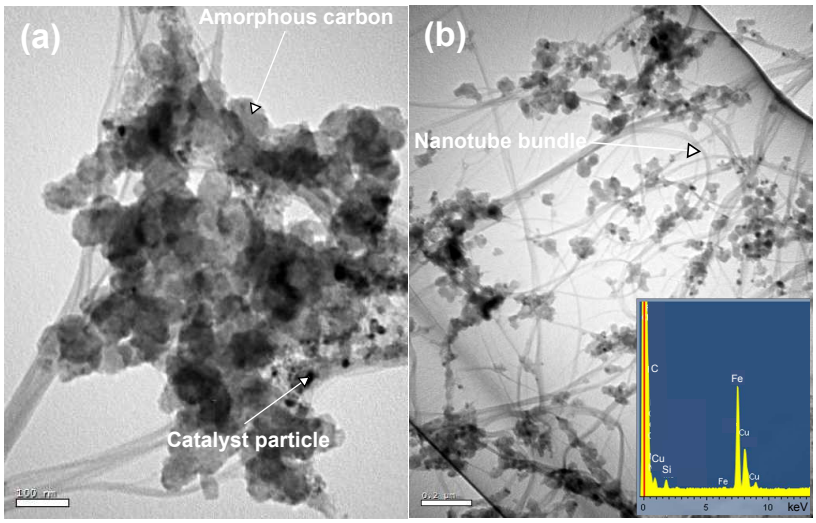

Figure 4.3: Transmission electron microscope (TEM) images of (a) as-grown commercial arc (Nanoledge) SWNTs and (b) after purification using procedure 1. The energy-dispersive x-ray (EDX) spectrum inset into part (b) shows that the arc-discharge nanotube sample still has a significant number of Fe catalyst particles even after purification. The Cu signature originates from the copper TEM grids on which the nanotubes were deposited. The small Si peak is another impurity left over from the growth process.

Amorphous carbon can be identified as irregular lumps of material with a contrast similar to that of the nanotubes. The metallic catalyst particles appear as very dark spots - due to their relatively high atomic number they tend to scatter the electrons of the beam and hence very few electrons are transmitted. The level of magnification shown in these images is too low to see individual SWNTs, and only bundles of nanotubes are visible.

4.3.2 Characterisation of CVD SWNTs

The commercial CVD nanotubes used in this study were purified using both procedures 1 and 2. Figure 4.4 shows the nanotubes before and after purification using method 1.

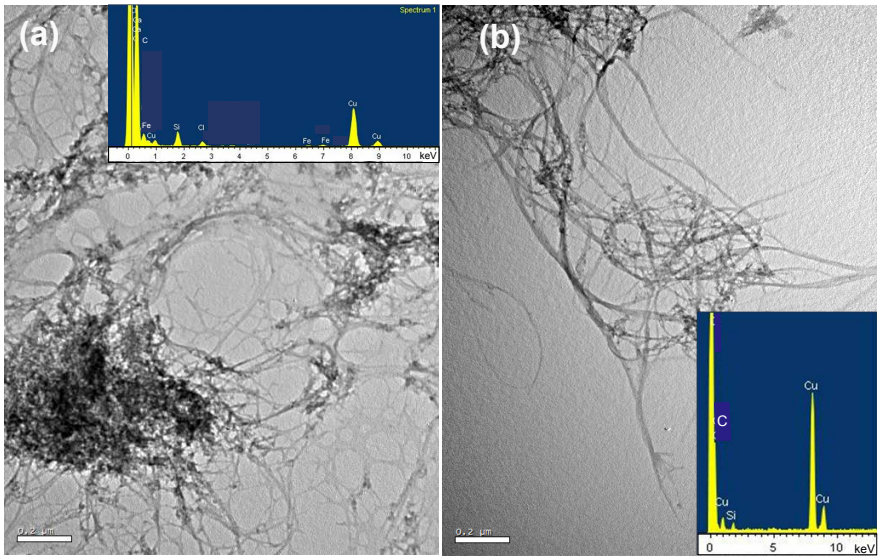

Figure 4.4: (a) as-grown commercial CVD (Nanocyl) SWNTs and (b) after purification using procedure 1. The EDX spectrum inset into parts (a) and (b) shows that the CVD nanotube sample still has Fe catalyst particles present before purification and a negligible number after purification.

After purification using this method there is a clear reduction in both the amount of amorphous carbon and the number of metallic catalyst particles present in the material. Comparing figures 4.4 and 4.3 one can see that the CVD nanotube sample has less metallic particles present than the arc nanotube sample purified with the same protocol. This is due to the presence of a large amount of onions with metallic cores which are produced during the arc-discharge synthesis process, which are difficult to remove.

Figure 4.5 shows the nanotubes before and after purification using method 2.

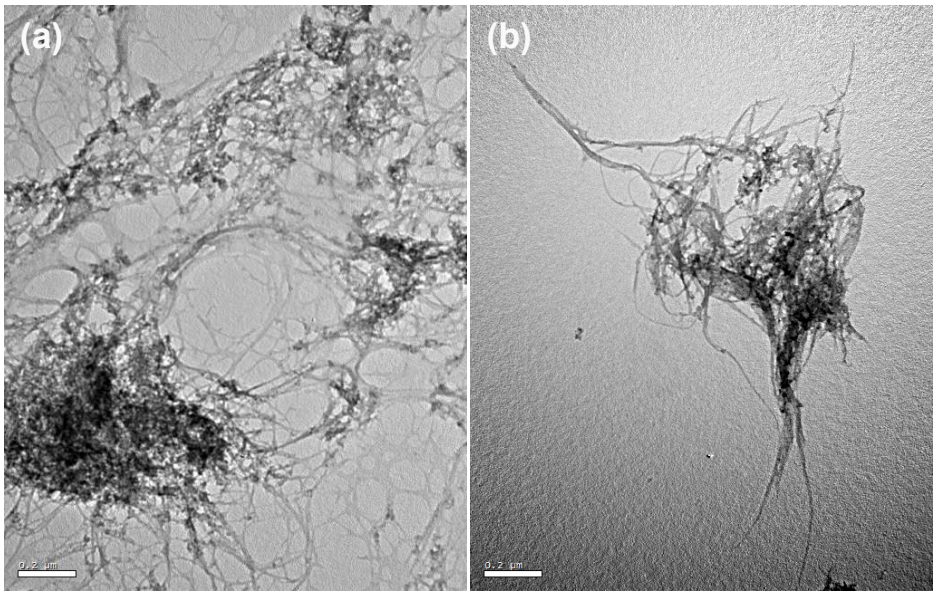

Figure 4.5: (a) as-grown comercial CVD (Nanocyl) SWNTs and (b) after purification using procedure 2

This method also resulted in a significant decrease in the amount of impurities in the material, however, perhaps not as much as achieved using the high temperature annealing process used in procedure 1.

Although purification procedure 1 appears to be more efficient than procedure 2, it was decided that it would be better to use procedure 2 to produce the purified nanotubes to be used for the Raman spectroscopy experiments of this study. It was thought that the hydrogen peroxide-based process would result in fewer defects in the structure of the nanotube and hence create less disruption to the nanotube spectra.

4.4 Nanotube end-opening

When formed, carbon nanotubes have hemi-spherical fullerenes capping their ends. These present a significant barrier to filling molecules and therefore need to be removed before a filling experiment is conducted. A method known to remove these end caps is to heat the nanotubes in air [65].

This process exploits the weaker C-C bonds in the in the end-caps of the nanotubes - the greater curvature and hence greater reactivity results in the carbon atoms in the caps being oxidised by the oxygen in the air and removed. The curvature of the walls of the nanotubes is less than that of the end-caps and hence the walls are stronger and less reactive - this makes them less susceptible to the oxidation process. The main draw-back of this process is the high temperature necessary to remove the end-caps can also damage the walls of the nanotubes. However, this process is necessary if a reasonable filling yield is to be obtained. Before each of the filling experiments conducted in this study the nanotubes were heated in air for 45 minutes at a temperature of 450 ^{o} C, to remove the end caps. The nanotubes to be covered with molecules were not subjected to this process because filling was not the goal.

4.5 Supercritical fluid molecular filling experiments

4.5.1 Equipment set-up

Governed by the specific properties of the molecular systems to be filled, two configurations of the rig have been used. Configuration A (Figure 4.6) is a primary one, compatible with the use of molecules that are not air-sensitive. Alternatively, for molecules that oxidize on exposure to air, configuration B (Figure 4.8) was required. This involved further development of configuration A, so that molecules were kept in a dry solvent (i.e avoiding air exposure) over the whole duration of the filling experiment.

The purpose of the experimental rig shown is to provide and maintain a stable supercritical CO_2 fluid environment with specific user-set pressure and temperature conditions. The various parts of the rig are indicated in the figure and their roles are explained below.

4.5.2 Configuration A

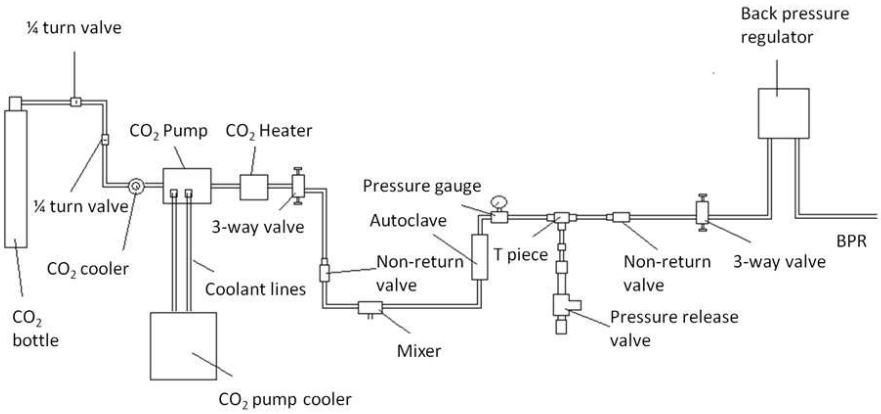

Figure 4.6: Schematic diagram of the supercritical CO_2 rig in its basic configuration, A.

The liquid CO_2 is supplied by a cylinder which is at room temperature and pressurised to approximately 63 bars. Before entering the CO_2 pump, the liquid CO_2 is cooled to 0 ° C, it is then compressed by a liquid-CO_2 pump. In order to access the supercritical fluid state, the CO_2 needs to be compressed to a pressure greater than the critical pressure of 74 bars. After compression, the liquid CO_2 is first heated above the critical temperature of 31 ° C by a dedicated CO_2 heater and then again in the autoclave. The autoclave is a hollow stainless steel cylinder into which the nanotube samples to be filled are inserted. A thermocouple and dedicated heater maintain the sample region at a constant, chosen temperature. A back-pressure regulator maintains a constant system pressure at a user-set value by opening and closing an incorporated needle valve. At the end of the experiment, the waste CO_2 is exhausted through the back pressure regulator to the outside. During the molecular filling experiments conducted using this apparatus, the system pressure was taken through a number of repeated cycles as explained in chapter 3.

The majority of the equipment from which the rig is constructed is computer controlled - this is a very useful feature as it makes lengthly sequences of exact pressure cycles possible. An example of such a pressure cycle is shown in Figure 4.7.

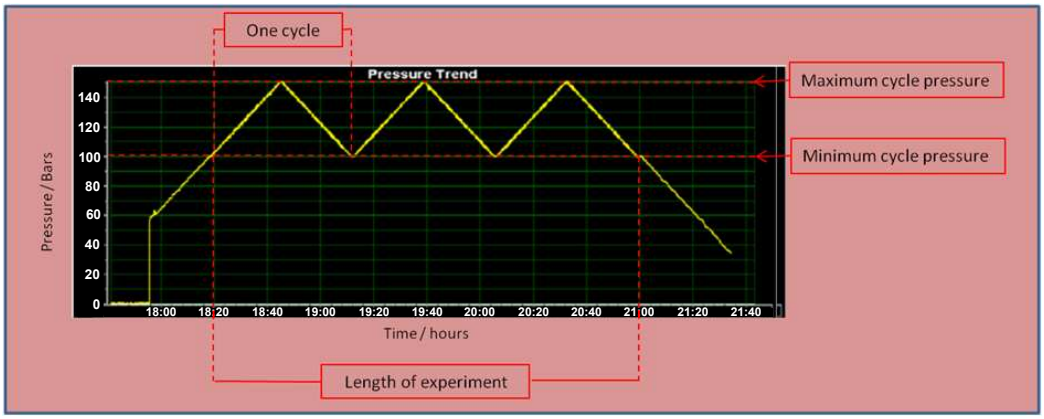

Figure 4.7: Example pressure cycling experiment

Typically, in these experiments a cycle started at a pressure of 100 bars, ramped up to 150 bars and then returned back to 100 bars. The period of time and number of the cycles is different depending on the type of experiment being run. The choice of experimental conditions will be justified in the next section, and depends on the physical processes that govern the nanotube filling.

4.5.3 Configuration B

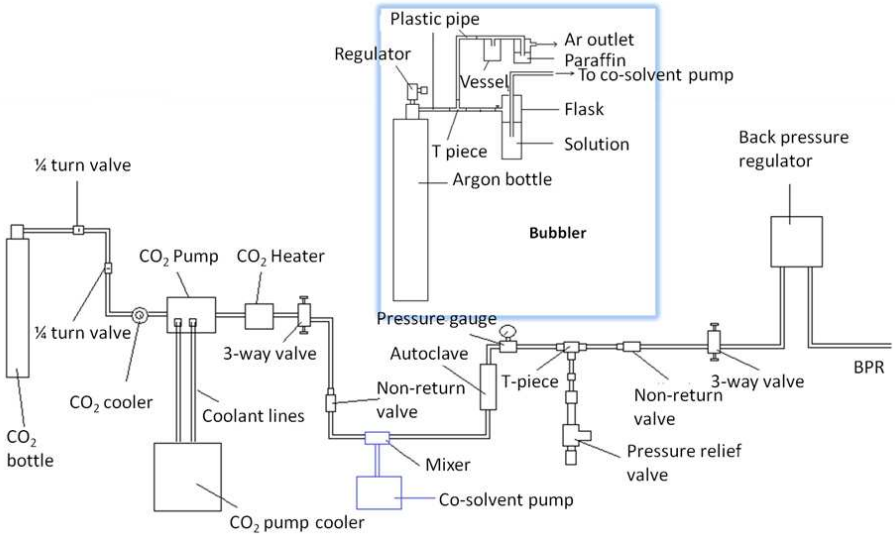

Figure 4.8: Schematic diagram of the rig in the configuration B, for filling from solution.

The filling molecules used in the second type of experiments are extremely sensitive to oxidation. While the experiment is in progress, the solution in which the molecules are dissolved (shown in the photograph in Figure 4.9 as a dark yellow liquid) is stored in an air tight experiment flask. The flask is connected to a supply of argon, this maintains a constant inert atmosphere throughout the experiment. To further reduce the risk of contamination, it was necessary to connect a bubbler to the gas line. This prevents a sudden vacuum from drawing air into the flask and contaminating the solution. The other major additions to the system are a co-solvent pump and a solvent mixer. The co-solvent pump is used to draw the molecule solution from the flask and to add it to the CO_2 pipeline at the mixer. The co-solvent pump is computer controlled and capable of automation. The mixer simply mixes the relatively low pressure solution with the high pressure CO_2. A photograph of the whole set-up is shown in Figure 4.9.

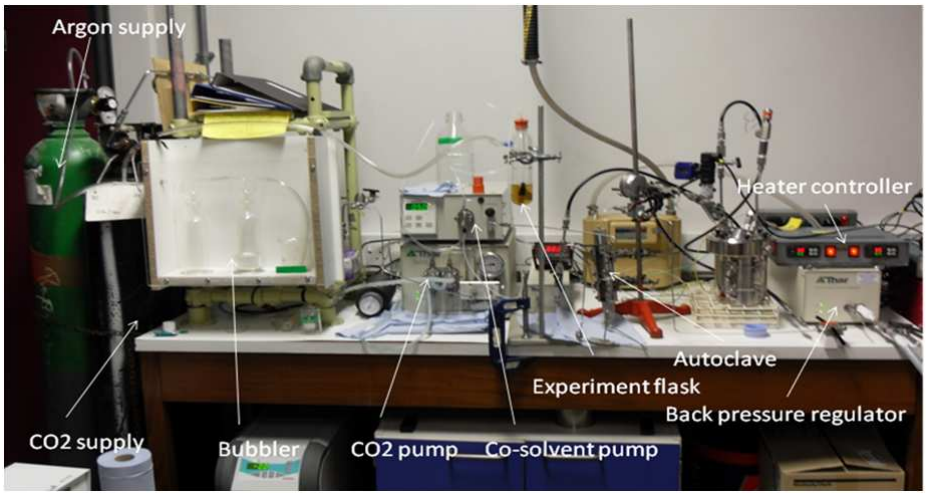

Figure 4.9: Filling from solution experiment in progress with the equipment in configuration B.

4.6 Sample production

Three different types of nanotube/ molecule hybrids were produced: (a) nanotubes endohedrally supercritically-filled from a mixed nanotube/ molecule powder, (b) nanotubes endohedrally supercritcally-filled from a molecular solution and (c) nanotubes exohedrally functionalised on the outer surface with molecules. Nickel tetra phenyl prophyrin (NiTPP), Nickel Phthalocyanine (NiPc) and Aluminium Phthalocyanine Chloride (ClAlPc) molecule powders were purchased from Sigma Aldrich.

4.6.1 (a) $ScCO_2$ filling of nanotubes from powder

This type of experiment involved supercritical filling of CVD SWNTs with the NiTPP, ClAlPc and NiPc organo-metallic molecules. Given that these molecules are not air sensitive, a powder mixture approach was used, with the nanotubes and molecules being mixed prior to being exposed to the $ScCO_2$. Configuration A of the supercritical CO_2 rig was used for the experimental set-up. In this case, the $ScCO_2$ helps the molecules to diffuse inside the nanotube mat and reach the open ends of the nanotubes, from where they are further carried inside the hollow cavity of the nanotube by the supercritical fluid.

Several stages of material preparation were necessary before running the experiment:

(i) CVD SWNTs were purified using either purification method 1 or 2 depending upon whether the sample was to be used for high resolution transmission electron microscopy or resonant Raman studies respectively.

(ii) The purified nanotubes were end-opened using the procedure discussed earlier.

(iii) The molecules to be used in the filling experiment were dissolved in the solvent appropriate to each individual molecule (see Table 4.1) to produce a saturated solution.

Both the NiTPP and ClAlPc dissolved easily in the solvents suggested by literature [39,66]. However, the NiPc molecule did not dissolve well in any of the solvents tried; it was found to partially dissolve in ethanol.

(iv) The purified nanotubes were added to the molecule solutions and together they were mixed by mild sonication and mechanical stirring.

(v) This solution was then drip condensed onto a piece of silicon substrate held on a heated plate at a temperature above the evaporation temperature of the solvent, forming a nanotube/ molecule mat (Figure 4.10 (a)).

Molecule	Solvent
NiTPP	Chlorofrom
ClAlPc	Ethanol
NiPc	Ethanol

Table 4.1: Solvents used for solubilising the molecules [39,66].

When the mat had dried, the silicon substrate was then attached to a sample holder for insertion into the system autoclave. The sample holder rests on the lower frit of the autoclave as in Figure 4.10 (b). The frits are filters with micro-meter sized pores, the lower frit prevents any contamination from the pumps or pipeline from contaminating the system, while the upper frit prevents clumps of the sample from escaping from the autoclave.

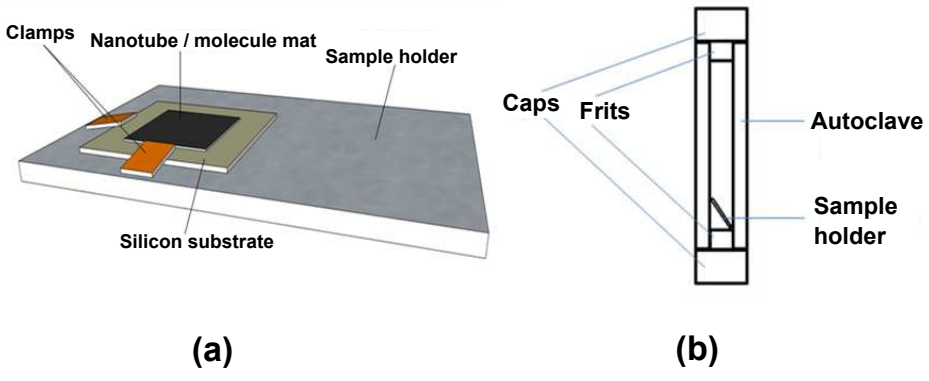

Figure 4.10: (a) Schematic diagram of the sample holder prior to autoclave insertion. (b) cross-section view of the autoclave with the sample inserted.

Pressure cycles between 100 and 150 bars, similar to those shown in Figure 4.7, were run. A typical experiment lasted for a number of days with a number of pressure cycles being carried out; a summary of the experiments conducted is given in Table 4.2. The experiments were run with a fixed sample temperature of 50° C.

4.6.2 Summary of samples produced

Five samples were produced, the two samples destined for HR-TEM study were purified using procedure 1, had shorter filling experiments with fewer pressure cycles and used only the NiTPP molecule. The remaining three samples were purified using procedure 2, had longer filling experiments with a greater number of cycles, and all three of the non-air sensitive molecules were used. These samples were studied using Raman spectroscopy. A summary of the samples produced is given in Table 4.2.

Molecule	Number of cycles	Cycle duration / hours	Future experiments
NiTPP	3	12.5	HRTEM
NiTPP	3	30	HRTEM
NiTPP	10	24	Raman
ClAlPc	9	24	Raman
NiPc	8	24	Raman

Table 4.2: Summary of samples produced by the powder filling experiments.

4.6.3 (b) $ScCO_2$ filling of nanotubes from a molecular solution

For filling of SWCNTs with Cobalt Carbonyl molecules it was necessary to develop a method which avoided contact of the molecules with oxygen, this is because the molecules readily oxidise in air.

For this reason it was decided to use a filling-from-solution method, with the set-up in configuration B. In contrast to the powder filling experiments, the filling molecules in solution are introduced directly to the $ScCO_2$. It was thought that this might have resulted in a greater solubilisation of the cobalt carbonyl molecules and hence might allow the molecules to diffuse through the nanotube mat more easily. Cobalt carbonyl molecules were purchased from Sigma Aldrich.

The nanotubes of this experiment were prepared using the following procedure:

(i) Arc nanotubes material was subjected to purification procedure 1.

(ii) The nanotubes were then end opened using the procedure described earlier.

(iii) Hexane was used to make a suspension of the nanotubes, and this suspension was drip condensed to form a mat on a silicon substrate which was attached to the sample holder.

The main differences between this method and that of the method used in the powder filling experiments is that the molecules were not mixed with the nanotubes directly, and the use of smaller diameter arc-nanotubes.

The creation of the cobalt carbonyl solution using dry hexane (dry hexane being oxygen free) required a completely new method of sample preparation. The oxygen sensitive nature of the filling molecules meant that all the processing stages had to be done in an inert atmosphere. The inert atmospheres for the weighing of the molecules and the subsequent mixing of the molecule solution were provided by the use of a glove box and Schlenk line under a nitrogen atmosphere respectively. The resulting solution was kept under an argon atmosphere for the entire filling experiment, as shown in Figure 4.9. The cobalt carbonyl/ hexane solution was slowly added to the supercritical CO_2 during the filling experiment by the co-solvent pump via the mixer. The type of co-solvent pump used for these experiments is designed to pump solvents such as hexane.

The pressure of the CO_2 was cycled between 100 to 150 bars as with the other powder experiments, however, due to the limited volume of cobalt carbonyl / hexane solution contained in the experimental flask the experiments were limited to cycles of only 50 minutes in duration.

Unfortunately, these experiments were unsuccessful and no useable samples were produced. This resulted from the cobalt carbonyl/ hexane solution causing the valves in the co-solvent pump to block and hence causing the pumping to stop. It was necessary to dismantle part of the apparatus and send the pump away for costly repairs. In an attempt to overcome this problem, a number of these experiments were conducted, with both dilute and very dilute solutions; however, the result was the same each time. It was decided that in order to save time and avoid costly repairs, that it was best to concentrate on the experiments using the air-stable molecules and to abandon air-sensitive cobalt carbonyl molecules as filling materials.

4.6.4 (c) Exohedral functionalisation of SWNTs

These experiments produced CVD SWNTs with their exterior surfaces covered with each of the air-stable molecules. The procedure used to create these samples is as follows:

(i) CVD SWNTs were purified using purification method 2.

(ii) The molecules to be used to produce the nanotube hybrid samples were dissolved in the solvent appropriate to each individual solvent (see Table 4.1) to produce a saturated solution.

(iii) The purified nanotubes were added to the molecule solutions and together they were mixed by mild sonication and stirred mechanically for several days.

(iv) This solution was then drip condensed onto a piece of silicon substrate held on a heated plate at a temperature above the evaporation temperature of the solvent, forming a nanotube/ molecule mat.

A method similar to the one described has been found to result in nanotubes with a good coverage of molecules [42].

The key differences between the samples production methods for covered samples are that the samples were not end-opened prior to being covered and the covered SWNTs were not exposed to $ScCO_2$. The exclusion of these two steps should ensure that the number of molecules attached to the outer surface of the nanotubes should far exceed those encapsulated inside which may have entered through defects in the walls of the nanotubes. The samples produced by this method were investigated by resonant Raman spectroscopy.

It is important to note here that the nanotubes used to create these samples were from the same batch as those used to make the $ScCO_2$ filled from powder samples, matched by molecule. This means that it is reasonable to compare the Raman spectra of SWNTs filled and covered with the same molecular system. However, the nanotube batches used to form the hybrid samples were dissimilar between molecular types and therefore cannot be compared reliably. This is because a Raman spectrum acquired from SWNTs from batches which have undergone a greater amount of purification may be slightly different to a spectrum acquired from to an earlier batch which is less purified.

4.7 Removal of extraneous molecular material

After each nanotube filling or covering experiment, the samples were washed using the appropriate solvent for each individual molecule Table 4.1. This process was necessary to remove excess (i.e. unattached) molecules in the sample. Excess molecules can cause the resonant Raman spectra of nanotube/ molecule hybrid samples to be dominated by the spectrum of the molecules. The washing was effected by filtering the sample with the appropriate solvent (i.e. the solvent which solubilised the respective molecule) under vacuum pumping until the filtered solvent became colourless. The resulting powder was then washed with water and dried over-night at 90^{o} C.

Chapter 5

HRTEM investigations of the internal structure of hybrids of nanotubes and organo-metallic molecular systems

We demonstrate through High Resolution Transmission Electron Microscopy (HRTEM) the successful encapsulation of large, planar organo-metallic molecules (larger than in previous works) by SWNTs using a supercritical CO_2 based method. Due to their size (≈2 nm across), such molecular systems are expected to be difficult to encapsulate using more standard, thermal diffusion-based procedures. Encapsulation was obtained in nanotubes with a wide range of diameters, including diameters less than an optimum value resulting from geometrical considerations. Unlike in other works, HRTEM revealed row-like ordering of the organo-metallic molecules in nanotubes with diameters close to the optimum value. Confinement by the nanotube template appears to play a role as templates of larger diameters did not induce ordering.

5.1 High Resolution Transmission Electron Microscopy

High resolution transmission electron microscopy (HRTEM) is a very useful technique for studying carbon nanotubes - it can be used to identify the presence of nanotubes in a sample, perform measurements of the diameters of nanotubes in a sample to provide statistics for diameter distributions and to identify structural defects [23].

Transmission electron microscopy is a direct imaging technique [23] which allows for the interior of the nanotubes to be probed. This makes it ideally suited to characterising the internal structure of carbon nanotube hybrids.

Figure 5.1 shows a schematic drawing of the most important components of a TEM.

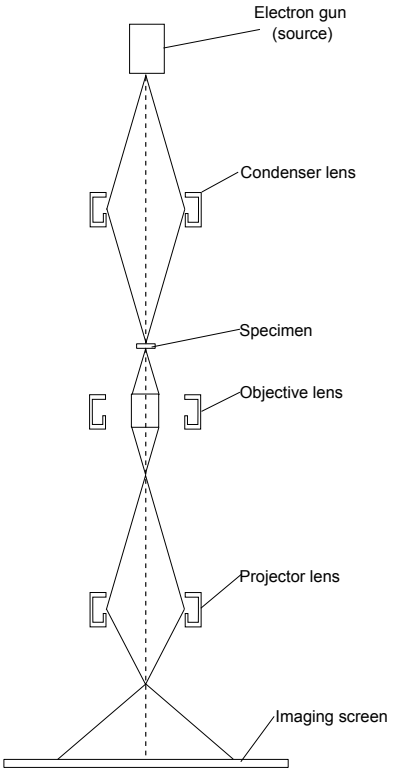

Figure 5.1: Schematic diagram showing the primary components of a TEM, including the most important magnetic lenses, specimen and imaging screen (based upon [67]).

A TEM works by exploiting the particle wave duality of electrons, which is described by the de Broglie relationship:

$$\lambda_e = \frac{h}{m_e v}, \tag{5.1}$$

where λ_e is the effective wavelength and v is speed of the electrons in the TEM beam, m_e is the mass the electron, and h is Planck's constant [67].

With sufficiently high electron velocities it is possible to obtain effective wavelengths of less than an angstrom, and hence to resolve structures much smaller than possible with an optical microscope.

Electrons are accelerated in the electron gun of the TEM by a voltage V. This is the source of the radiation which will illuminate the sample to be investigated. An electron accelerated by a voltage V will gain a kinetic energy described by $\frac{1}{2}m_e v^2 = eV$, where e is the charge of the electron. From which: $v = \sqrt{\frac{2eV}{m_e}}$. Substituting this equation for v in equation 5.1 gives: $\lambda_e = \frac{h}{\sqrt{2m_e eV}}$. Putting in the values for the constants, the following expression is obtained: [67]:

$$\lambda_e = \frac{12.3}{\sqrt{V}}\text{Å}. \tag{5.2}$$

It is clear that the larger V becomes the smaller the effective wavelength of the electrons becomes. For example for an acceleration voltage of 100 kV, $\lambda_e = 0.039$ Å. If the resolution of a TEM depended entirely upon the effective wavelength of the electrons being accelerated, it could achieve sub-atomic resolution. However, the main limit to the resolution of a TEM is the quality of the magnetic lenses which guide and focus the electron beam.

The condenser lens regulates the convergence of the illuminating beam on the specimen. The objective lens focuses the electron beam which has passed through the specimen and provides the first magnification of the image produced. The projection lens magnifies a portion of the magnified image further to form the final image.

The lens which has the greatest effect on the resolution of the image formed is the objective lens; it is the most critical component of a TEM [67]. There are a number of intrinsic aberrations to electron optics which cannot be corrected, but their effects can be minimized. The most important is known as spherical aberration [67] - it is produced by the geometry of the lens field. It occurs along the axis of the beam and results from the lens further away from the centre of the beam having a greater refractive power and hence shorter focal length. In a modern HRTEM system with a suitable sample it is possible to obtain minimum resolutions in the order of a few angstroms.

Images are obtained from a TEM by an imaging system which converts the electron radiation into visible light such as a fluorescent viewing screen [67].

Details of the images produced are due to variations in specimen contrast [67]. When the electrons of the beam transit through a specimen, a fraction will be scattered by the material present. If scattered by a large enough angle, the electrons are lost from the beam and a corresponding loss of beam intensity results. The amount of scattering which occurs at a given point in the specimen is dependent upon the physical density and thickness of the material there. In the images shown in this chapter, bright regions indicate high electron transport and low scattering, while dark regions indicate a high level of electron scattering and a low level of transmission.

In the TEM study of carbon nanotubes the factor most likely to result in specimen damage is exposure of the nanotubes to the electron beam. This is especially true for nanotubes studied under HRTEM conditions using acceleration voltages in excess of 100 keV.

Damage to the sample occurs through inelastic scattering between the electrons of the beam and the material of the specimen. The amount of damage done to the sample depends most of all upon the beam current and the exposure time. The minimum beam intensity required to form a usable image limits how far the beam current can be reduced, therefore when imaging samples it is wise to minimize the duration for which the sample is exposed to the beam.

Irradiation of carbon nanotubes by an electron beam results in structural defects and eventually destruction of the nanotube.

5.2 Equipment and experimental methods

SWNTs filled with NiTPP molecules were sonicated in chloroform using an ultra-sonic probe to form a well dispersed and de-bundled solution. Drips of this solution were deposited onto lacey carbon film TEM grids. Lacey carbon film grids are formed from very thin films of carbon which possess irregular holes. The best contrast of the interior of the filled nanotubes is obtained from individually separated nanotubes which are suspended across these holes.

HRTEM was performed by Dr. Adelina Ilie using two microscopes at the University of Oxford, a JEOL 3000F field-emssion gun (FEG) microscope and a 4000HR with a LaB_6 source, both operated at 100 keV. The 3000F microscope had a spherical aberration coefficient (C_s) of 0.57 mm giving it a point resolution of $\approx$ 0.225 nm at 100 keV, while the 4000HR had a substantially less good resolution due to higher energy spread and beam divergence (see Table 5.1). Nevertheless, the resolution of the 4000HR was sufficient to allow one to observe the contour of the encapsulated molecules (see section 5.4). The majority of the images in this study were taken with the 4000HR microscope.

Microscope	Spherical aberration coefficient / mm	Defocus spread / nm	Energy spread / eV	Beam divergence / mrad
4000HR (LaB_6 source)	0.9	10	1	1
3000F (FEG)	0.6	4	0.1	0.15

Table 5.1: Microscope parameters for the two HRTEMs used in this study.

The 100 keV energy of the electrons is slightly above the knock-on threshold of ≈86 keV for carbon atoms in pure carbon nanostructures [68,69], such as empty SWNTs, and is considered as appropriate for routine images of such nanostructures [68]. In order to reduce the rate of knock-on displacement of carbon atoms [69], the irradiation dose was kept low. Calculations based upon Ref. [69] show that at 100 keV, under beam current densities of 0.4 to 2 A/cm^2 (as used here), the displacement rate of carbon atoms, p, ranges between 3.6×10^{-5} to $1.8 \times 10^{-4} s^{-1}$; this is equivalent to saying that each carbon atom under the beam has been displaced once in $1/p$ ranging from 28000 s (for the lowest dose), to 5600 s (for the highest dose) [70]. These values compare well with our observation times, which were kept low, typically, to only several minutes.

To compare with the experimental images, HRTEM images were simulated. For this, structural models of carbon nanotubes with encapsulated organo-metallic molecules were generated with Crystal Maker [71], while their image simulations were performed with SimulaTEM [72]. Sets of focal series were produced with the molecules in different conformations.

Generating focal series implied that the focal length was varied from under focused to over focused. This was done in order to minimise the effect of the spherical aberration C_s. At the so called Scherzer focus z_s given by:

$$z_s = -c\sqrt{C_s\lambda} \tag{5.3}$$

with c a constant between 1.0 and 1.2, the image of a weak phase (thin) object, such as a carbon nanotube is intuitively interpretable [73].

5.3 HRTEM of related systems

Prior work on organometallic systems close in size to those used in this study will now be discussed. For all encapsulated systems, when determining the optimum filling diameter for a particular molecule it is necessary to consider both the geometry of the molecule and the interaction between the van der Waals surface of the molecule and that of the interior of the nanotube in which they are to be encapsulated. In general the optimum filling diameter of the nanotube is given by the equation 3.3.

In a study by Schulte *et al* [36], roughly square CoPc molecules with a corresponding van der Waals surface of $\approx 1.1nm^2$ in area [74] and 1.5 nm across the diagonal were encapsulated inside carbon nanotubes [36] (see Figure 5.2 (a)). With the dimensions quoted, the CoPc molecule would have d_{optimum} of $\approx$ 1.4 nm for side-on filling (Figure 5.2 (c)) and an $d_{\text{optimum}}\approx$ 1.8 nm for face-on filling (Figure 5.2 (d)). CoPc molecules were found to be encapsulated with a high yield inside of nanotubes of 2.2 and 2.6 nm in diameter and to a lesser extent inside of nanotubes with $d = 1.5$ nm [36]. The higher filling yield observed in the larger diameter nanotubes is attributed to greater freedom of entry for the molecules into the interior of the nanotubes [36]. The authors also deduced that in nanotubes with $d < 1.8$ nm the molecule will only fit inside the molecule if inclined at an angle. We note that this might be due to the rather rigid structure of the phthalocyanines; the six-member ring appendages are linked through two C-C bonds to the phthalocyanine body which does not allow significant distortion outside of the plane of the molecule.

The authors did not observe any significant ordering of the CoPc encapsulates in any of the nanotube templates, from narrow to wide diameter, based on HRTEM evidence (see Figure 5.2 (a)), though some ordering was inferred from near-edge X-ray absorption fine structure (NEXAFS) investigations.

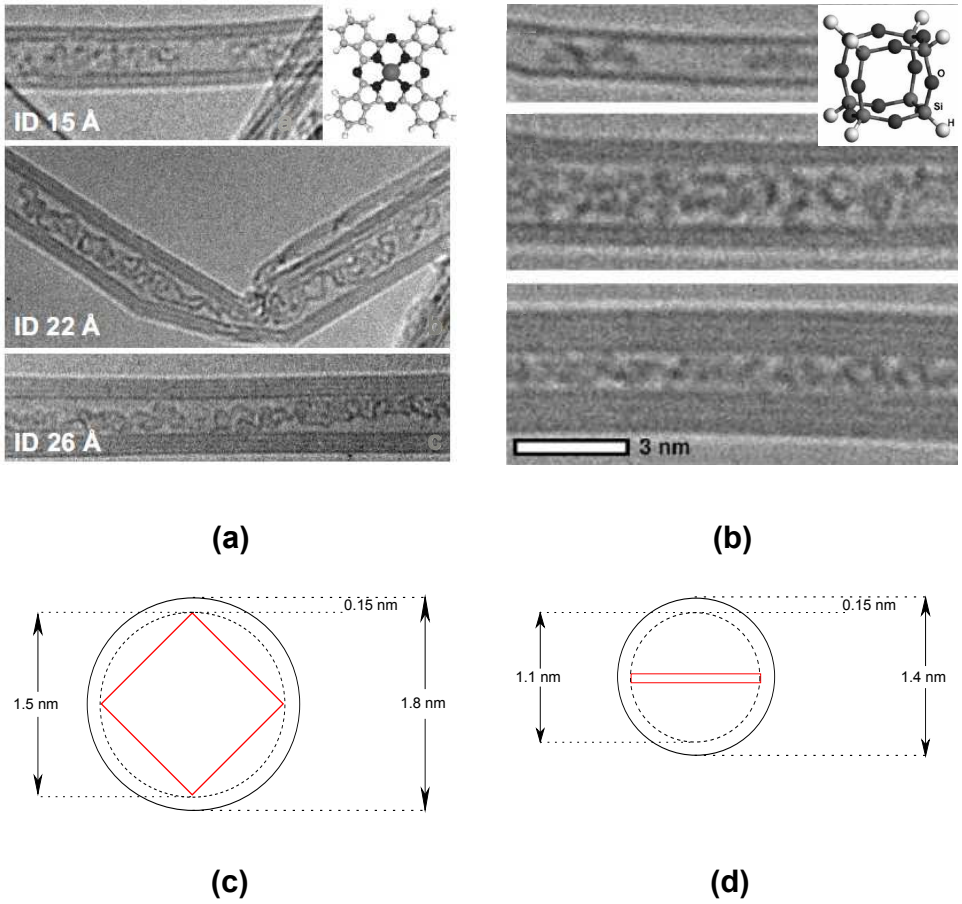

Figure 5.2: HRTEM images of carbon nanotubes encapsulated with CoPc molecules [36] (a) and $H_8Si_8O_{12}$ [34] (b). Schematic diagrams of the molecules [34, 36], are shown as inserts. (c) and (d) show side-on and face-on contours of the CoPc molecule inside of an optimum diameter SWNTs respectively.

In a similar study by Wang *et al* [34] both SWNT and MWNTs were filled with roughly cubic $H_8Si_8O_{12}$ molecules (see Figure 5.2 (b)). The van der Waals diameter of the molecule was calculated to be 0.9 nm with a resulting optimum diameter of 1.2 nm across the diagonal of one side of the cube [34]. They found that SWNTs of greater than 1.2 nm were filled to a high degree with $H_8Si_8O_{12}$ molecules. The lack of aromatic appendages meant that no self-assembly inside of the nanotubes templates occurred for these molecules.

Both systems shown in Figure 5.2 are being used for comparison with our own experimental images.

5.4 Structural characterisation of hybrids of SWNTs and endohedral NiTPP

The NiTPP molecule is a roughly square molecule, its van der Waals surface measures 2.0 nm across the diagonal of the molecule and 1.4 nm along the side - the molecule is shown schematically in Figure 5.3 (a).

With these considerations in mind, there will be two optimum diameters for the NiTPP molecule, one measured using the dimension of the side of the molecule and another using the diagonal. A molecule that might not fit face on may fit side on. If the molecule enters face on, $d_{diagonal}$= 2.0 + 2×0.15 = 2.3 nm is the optimum diameter (see Figure 5.3 (b)). The same optimum diameter would be valid if the molecule was to be rotated through 90 degrees about an axis normal to the nanotube axis - we call this encapsulation along the diagonal of the molecule. It is also possible for the molecule to enter narrower nanotubes if it enters side on, in this case the optimum diameter d_{side}= 1.4 + 2×0.15 = 1.7 nm (see of Figure 5.3 (c)).

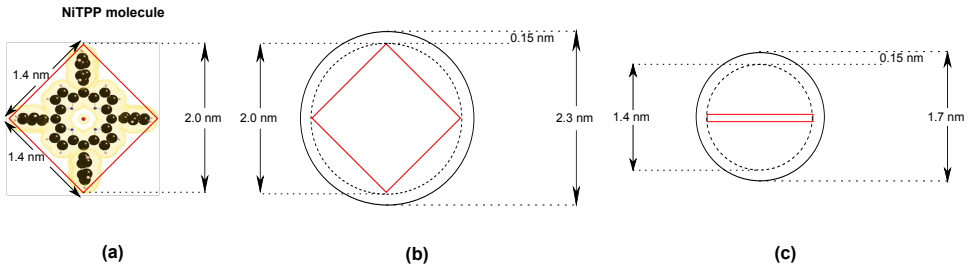

Figure 5.3: Schematic diagrams of (a) the van der Waals surface of the NiTPP molecule (based upon [37]) and the optimum nanotube diameters for (b) face-on and (c) side-on encapsulation.

Figure 5.4 shows encapsulation of NiTPP molecules inside of nanotubes around the optimum diameter for encapsulation along the diagonal - measurements of the nanotube diameters were obtained using Gatan Digital Micrograph analysis software.

High yield and continuous filling is observed for nanotubes with d >2.3 nm - this is consistent with a greater freedom of entry for the molecules in these wider nanotubes. Unlike the CoPc molecules from [36] (Figure 5.2 (a)), the NiTPP molecules appear to organize with a certain degree of ordering forming rows of molecules showing diamond-like units. This suggests encapsulation of the NiTPP along its diagonal, as shown in Figure 5.4 (d). In this case, molecules may assemble via the π-stacking of their six member ring appendages as proposed schematically in Figure 5.4 (e).

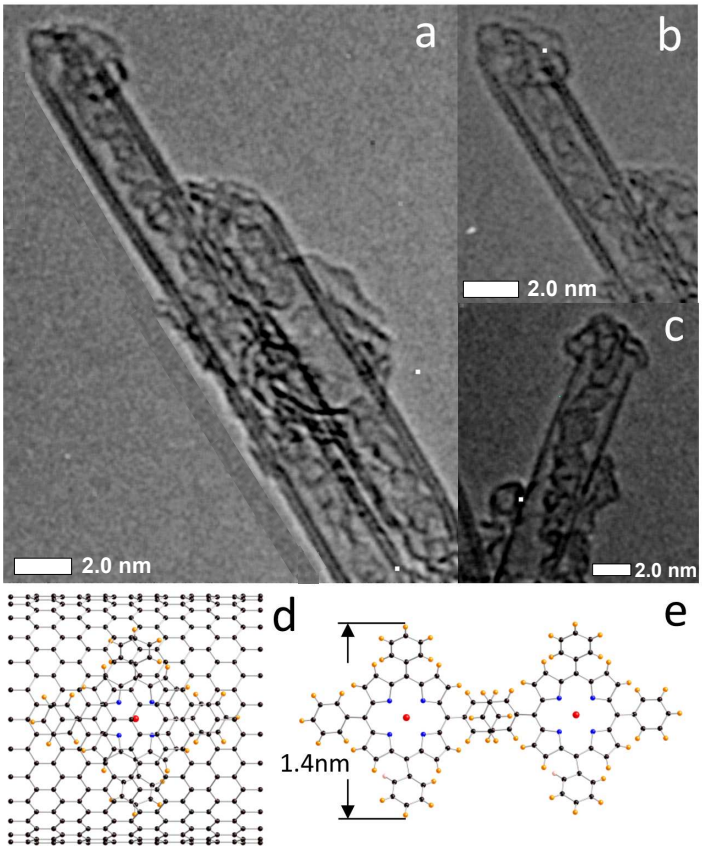

Figure 5.4: HRTEM of NiTPP - filled nanotubes with diameters greater than 2.3 nm, i.e. above the threshold for diagonal encapsulation. (a) Long continuous filling within a 2.3 nm diameter SWNT; (b) part of the same filling as in (a) with the row of molecules shifted towards the center of the nanotube. (c) NiTPP inside of a 2.7 nm diameter nanotube. (d) Schematics of diagonal encapsulation of the NiTPP. (e) Proposed π-stacking of NiTPP molecules.

Focal series (Figure 5.5) have been simulated in order to propose an assignment to the conformation of the NiTPP molecules inside of the nanotubes from Figure 5.4.

Defocusing distance was varied in steps of 5 nm above and below the Scherzer focus. The images at the Scherzer focus (see section 5.2) are the ones framed in red.

Figure 5.5 (c) shows the molecule in side-on entry inside of the nanotube, with the six-member ring appendages roughly perpendicular to the central body of the molecule, as in free-form, while 5.5 (b) shows the appendages being rotated to roughly align to the plane of the body of the molecule. This rotation has been performed as none of the experimental images show the dark contrast that accompanies the appendages positioned as in Figure 5.5 (c).

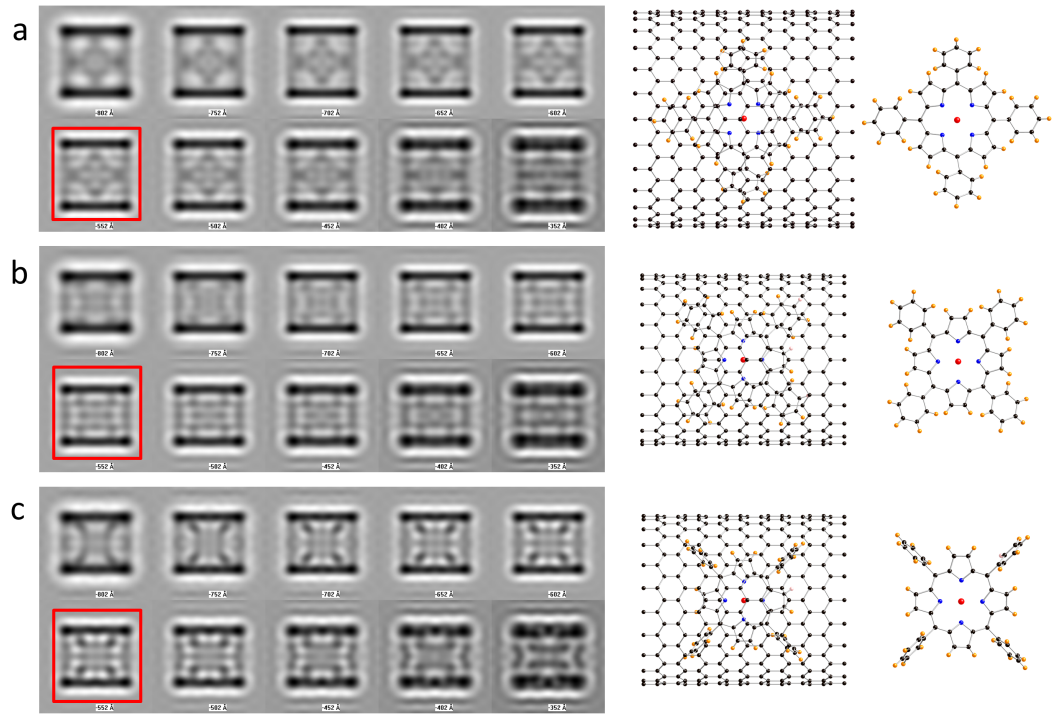

Figure 5.5: HRTEM simulated images of NiTPP entering SWNTs along diagonal (a) and side-on (b, c), respectively. Defocus varied in steps of 5 nm above and below the Scherzer focus, located at -57 nm. Larger nanotubes are needed to accommodate the molecule when entering along the diagonal. Parameters used for the simulation are those of the 4000HR microscope. In red, Ni atoms; in blue, N; in black, C; and in orange, H.

We note that the appendages of the TPP molecules are expected to be more flexible than those of the Pc molecules (see Figure 5.2 (a)) due to just a single C-C bond with the body of the molecule.

It is in this conformation of the appendages that non-metallic (un-chelated) TPP self assembles with other TPP molecules to form J-aggregates in unconstrained environments [75] (see Figure 5.6).

In unchelated TPP-based J-aggregates the assembly occurs through π-stacking between the appendage of one molecule and the central body of the neighbouring one.

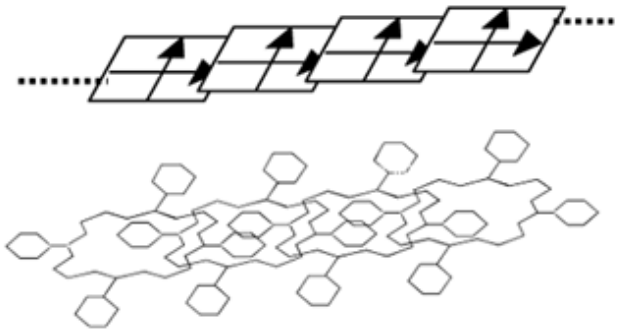

Figure 5.6: Unchelated TPP self-assembled into J-aggregates (based upon [75]). The top diagram shows sliding of the molecules along two directions in order to produce π-stacking.

However, as noted in chapter 3 section 3.3, the presence of the central metal, as in our case, disrupts this π-bonding; the remaining possibility is π (AB-) stacking through appendages of adjacent molecules.

Figure 5.7 demonstrates that NiTPP encapsulation has been achieved using $ScCO_2$ as a transporting medium in a large range of diameters, sub- and above d_{optimum}. Encapsulation in a sub-optimum diameter of 1.3 nm (Figure 5.7 (a)) has been observed only occasionally, therefore it has a low yield. In addition, even when encapsulated inside of a nanotube the filling is sparse and the molecules, seen in side view, seem highly distorted. Figure 5.7 (c) shows that encapsulation of molecules in much larger diameters than d_{optimum} is not conducive of ordering, potentially due to having relaxed the spatial constraint imposed by the nanotube template. Based upon the HRTEM evidence gathered, it appears that ordered assembly in a single row (Figure 5.7 (b)) is highly favoured when the molecules are constrained in nanotubes with diameter close to d_{optimum}.

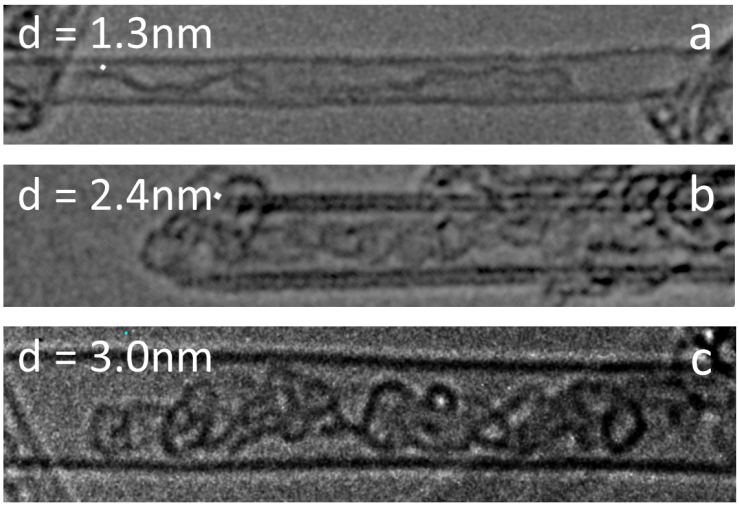

Figure 5.7: Experimental HRTEM images of NiTPP encapsulated inside of three types of nanotube templates: with $d < d_{optimum}$ (a), (b) $d \approx d_{optimum}$, and (c) $d > d_{optimum}$.

Ordering has been observed in TEM also when small rectangular perylene-3,4,9,10-tetracarboxylic dianhydride (PTCDA) organic molecules were encapsulated [76]. In this case doubly stacked molecular structures were obtained. The observation of the ordering in Figure 5.7 (b) might be favoured also by the lower electron doses used in this study. In contrast, in [36] ordering of CoPc was not observed directly by HRTEM. It has been suggested by [36] that the ordering may have been destroyed by interaction between the electron beam of the TEM and the encapsulated molecules. This effect was minimized in our work by careful choice of low electron beam doses (see section 5.2).

Chapter 6

Resonant Raman spectroscopy of filled carbon nanotubes

In this chapter Raman spectroscopy is employed to investigate the electronic properties of SWNTs both endo-and exohedrally functionalized with planar organo-metallic molecules. Changes in both the radial breathing mode (RBM) and G bands are observed upon functionalisation. The changes in the positions of the nanotube G bands, known to be sensitive to charge transfer-induced strain, are discussed in terms of charge transfer from the molecules to the nanotube. Changes in G band peak position are also discussed in terms of structural strain induced in the nanotube by the encapsulation process.

6.1 Introduction to the Raman effect

6.1.1 Raman-active molecules - a classical treatment

When a molecule is subjected to irradiation with an electromagnetic wave with a frequency ν, the oscillatory electric field $\vec{E}$ of the electromagnetic wave slightly changes the distribution of the electrons within the molecule. This causes a dipole moment $\vec{P}$ to be induced in the molecule. $\vec{P}$ is proportional to $\vec{E}$ and can be expressed as:

$$\vec{P} = \alpha\vec{E}, \tag{6.1}$$

where the constant of proportionality α is the polarizability of the molecule. The polarizability can be thought of as how easily the electron cloud of the molecule can be distorted. As both the $\vec{E}$ and the molecule are three dimensional, α is a tensor quantity. For simplicity, we shall limit our discussion here to one dimension. Substituting the wave equation of an oscillating electric field $E = E_0 Cos(2\pi\nu t)$ into equation (6.1) the following expression is obtained:

$$P = \alpha E_0 Cos(2\pi\nu t), \tag{6.2}$$

where E_0 is the maximum amplitude of the oscillatory electric field and t is time. In a Raman-active molecule, the polarizability of the molecule is linked to the vibrational state of the molecule, therefore it is necessary to add an additional term to α. The polarizability of the molecule is split into two components, one which is independent of molecular vibration α_0, and a second which is a sum of terms having the periodic time dependence of the normal frequencies of the system under consideration and which changes with the molecular vibration α_{n}. The polarizability is given by

$$\alpha = \alpha_0 + \sum \alpha_n cos 2\pi\nu_n t \tag{6.3}$$

The normal frequencies ν_n may be the rotation or vibrational frequencies of the system under study. Now substituting equation (6.3) into equation (6.2) the following equation for the dipole moment of the molecule can be obtained:

$$P = \alpha_0 E_0 Cos(2\pi\nu t) + \frac{1}{2} E_0 \sum \alpha_n [Cos 2\pi(\nu - \Delta\nu_n)t + Cos 2\pi(\nu + \Delta\nu_n)t] \tag{6.4}$$

The first term of the expression describes the dipole moment of the molecule oscillating with the same frequency as that the electric field of the incident electromagnetic wave ν_0. It is well known from the electromagnetic theory of waves that an oscillating dipole emits electromagnetic radiation the frequency of which is that of the dipole. There is no discrepancy between the frequencies of the incident and scattered radiation, therefore this term of the expression simply describes Rayleigh scattering.

The second term contains a component that refers to vibrations at two different frequencies $(\nu - \Delta\nu_n)$ and $(\nu + \Delta\nu_n)$, these account for the Stokes and anti-Stokes Raman bands respectively. This equation reveals the main pre-requisite for Raman scattering to occur - for the Raman effect to occur, the factor $\sum \alpha_n$ must be non-zero - it means that the vibrational modes of a molecule are Raman-active only if vibrational displacement of the molecule results in a change in the polarizability. The practical consequence of this selection rule is that a molecule could have a large number of possible vibrational modes but only a subset of these will be Raman active [77].

The problem of describing the allowed normal modes lends itself to group theory, with its (molecular) point groups and associated symmetry elements. In particular, the following rule applies; if the symmetry group of a normal mode is the same as the symmetry group of a quadratic form (x^2, xy etc.) then the mode is Raman-active [20]. For example, in the case of carbon nanotubes, for 1^{st}-order Raman processes, the Raman active modes have group symmetries A, E_1 and E_2 [28].

6.1.2 Photonic scattering processes

While classical electromagnetic theory provides a thorough view of the Raman effect, there are however, some effects that classical theory alone cannot explain. For example, classically speaking the molecule can vibrate at any frequency, while in reality that is not the case. A quantum mechanical treatment provides a clearer view of the situation.

When a Raman-active material is irradiated with light of frequency ν_0 a vast number of photons with quantised energy $\epsilon_0 = h\nu_0$ pass through the material unhindered. However, a fraction of the photons are reflected away from the main direction of propagation, i.e. are scattered. The majority of the photons undergo elastic (or Rayleigh) scattering in which a photon with an energy ϵ_0 incident upon the material is absorbed by the material, exciting an electron from the ground state to a virtual state ϵ_r. There is then a rapid decay from this state down to the ground state - a photon with a quantised energy of ϵ_s is emitted as a result (see Figure 6.1).

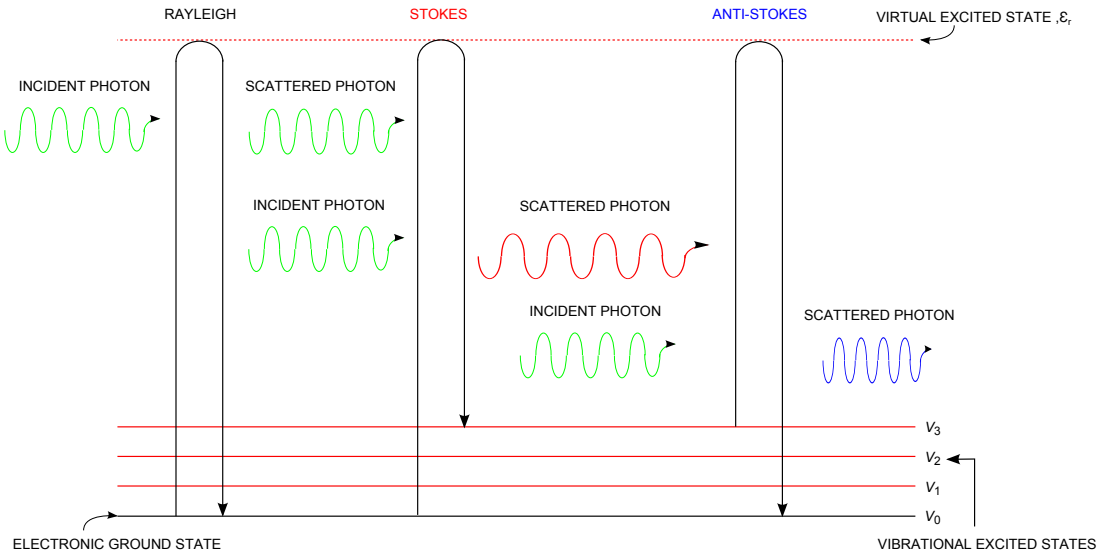

Figure 6.1: The three possible ways light can scatter from a Raman-active material (based upon [78]).

The process is elastic, therefore there is no difference $\Delta\epsilon$ between the energy quantra of the incident and scattering photons, such that the following expression is true:

$$\Delta\epsilon = \epsilon_0 - \epsilon_s = 0 \tag{6.5}$$

A small fraction of the scattered light undergoes Raman scattering, which is an inelastic process. In this effect, incident photonic energy is either reduced or augmented by the interaction with the material. This energy change is accounted for by a quantised electronic change in the vibrational energy state of the molecule.

There are two components to Raman scattered light, one which results from vibrational quatra $\Delta\nu_{\mathrm{n}}$ being gained by the material from an incident photon and a second where the opposite is true - they are known as Stokes and anti-Stokes scattering repectively.

If the material absorbs an incident photon of energy ϵ_0 and is excited from the ground state to a virtual state ϵ_{r}, the material rapidly decays from the virtual state down to a vibrationally excited state ν_{n}, emitting a photon with a lower energy ϵ_{s} in a random direction in the process; this is Stokes scattering. The energy difference between the incident and scattered photon is non-zero and given by the following relation:

$$\Delta\epsilon = \epsilon_0 - \epsilon_{\mathrm{s}} = +\Delta\nu_{\mathrm{n}}, \tag{6.6}$$

where $\Delta\nu_{\mathrm{n}}$ is a quantum of vibrational energy in the material.

In Stokes scattering a quantum of vibrational energy $\Delta\nu_{\mathrm{n}}$ has been imparted to the material, and as a result of the conservation of energy, the scattered photon has lower energy than that of the incident. The material is left in a vibrationally excited state.

In anti-Stokes scattering the opposite situation occurs - initially the material exists in a vibrationally-excited state. Incident radiation excites the material from a vibrationally excited state ν_{n} to a virtual excited state ϵ_{r}. The material rapidly decays from the virtual excited state down to the electronic ground state of the material via the emission of a scattered photon with energy ϵ_{s}. The anti-Stokes scattered photon is of a higher energy than that of the incident, such that the energy difference between the two is described by the following expression:

$$\Delta\epsilon = \epsilon_0 - \epsilon_{\mathrm{s}} = -\Delta\nu_{\mathrm{n}}. \tag{6.7}$$

In anti-Stokes scattering, the material has lost a quantum of vibrational energy $\Delta\nu_{\mathrm{n}}$ and is left in a lower vibrational state.

There are different orders of Raman scattering - in 1st order Raman scattering, the incident photon gives energy to a single vibration, where as in 2nd order Raman scattering an incident photon gives energy to two vibrations.

6.1.3 A typical Raman spectrum

Materials are usually in the ground vibrational state, as a result Stokes scattering occurs far more often that anti-Stokes scattering. For this reason Stokes scattering is usually what is measured in Raman spectroscopy experiments [79]. The value that is measured in a typical Raman spectrum is called the Raman shift, this is simply the energy difference between the incident and scattered light but in terms of wavenumber k, such that the Raman shift is given by the following:

$$\Delta k = k_0 - k_\mathrm{s} \tag{6.8}$$

The energy difference $\Delta\epsilon$ is related to the Raman shift by the Δk by the following equation:

$$\Delta\epsilon = \frac{hc}{2\pi}\Delta k, \tag{6.9}$$

where h is Planck's constant and c is the speed of light in vacuum.

In a typical Raman spectrum, the intensity of light scattered from the sample is plotted as a function of Raman shift. By convention, Raman shift is measured in units of cm^{-1}.

The Raman shift from Stokes scattered light is measured from zero up to some maximum value imposed by limitations of the detector used to acquire the spectrum. The Raman shift increases with wavenumber, a large Raman shift indicates that a large amount of the energy of the incident photon has been converted into vibrational energy in the material.

Every molecule or nanoscale structure has a unique set of allowed Raman-active vibrational modes - these result in a set of bands in the Raman spectrum which are individual to that material. The intensity of these bands provides information about the photon-material interaction occurring in the sample. For example, a high intensity band is an example of a situation where there is a strong energy exchange between the incident photons and material.

6.1.4 Resonant Raman scattering

A powerful technique which is very useful for poorly scattering samples is Resonant Raman spectroscopy. The resonant Raman effect occurs when the energy of the incident light is approximately equal to an electronic transition energy of the sample. Here the virtual excited state ϵ_{r} of the regular Raman effect has been replaced by an actual excited state ϵ_{n}, this results in a massive increase in the intensity of the Raman scattered light. As well as the obvious benefit of greatly increased Raman-band intensities, through careful selection of the wavelength of the incident light the resonance effect can be used to selectively study the substructure of large molecules [20]. With the easy access to lasers which can provide monochromatic beams of coherent light at a range of wavelengths, Resonant Raman spectroscopy has become a widely used and very useful analytical technique.

6.2 Resonant Raman spectroscopy of SWNTs

Carbon nanotubes are one dimensional quantum systems, as such their electronic density of states is distributed into quantised functions called van Hove singularities (see section 2.3.4). If an electronic transition occurs in a carbon nanotube, it must be from a van Hove singularity in the valence band to a van Hove singularity in the conduction band, or vice versa, while also obeying the selection rules.

The selection rules for optical transitions in carbon nanotubes depend upon a number of aspects:

(i) The initial electronic state before the transition takes place.

(ii) The linear polarisation direction of the incident photon which will cause the transition.

(iii) The symmetry of the phonon produced.

In general, the selection rule for optical transitions between the van Hove singularities of the SWNT valence and conduction bands, ${E_\mu}^{V}$ and ${E_\mu}^{C}$ respectively, is given by ${E_\mu}^{V} \rightarrow {E_{\mu'}}^{C}$, where μ and μ' are the initial and final states respectively. Here $\mu' = \mu$ for incident light polarized along the axis of the nanotube (z axis) and $\mu' = \mu \pm 1$ for light polarized normal to the surface of the nanotube (x axis) [28].

When Resonant Raman spectroscopy is used to probe carbon nanotubes, a resonance condition can be achieved when the excitation energy of the probe laser matches that of the energy gap separating opposite van Hove singularities. When resonance is achieved the signal from the carbon nanotubes is greatly enhanced. If the laser excitation energy does not match an allowed transition energy, then no enhancement in the nanotube Raman signal will be obtained [28].

6.2.1 Resonant Raman spectra of SWNT

The modes expected from a typical Resonant Raman spectrum are shown below in Figure 6.2, which is an example spectrum of bundles of Nanocyl NC1100 nanotubes. The spectrum was acquired with a laser of excitation energy $E_{Laser} = 1.59$ eV. The most prominent modes have been labelled.

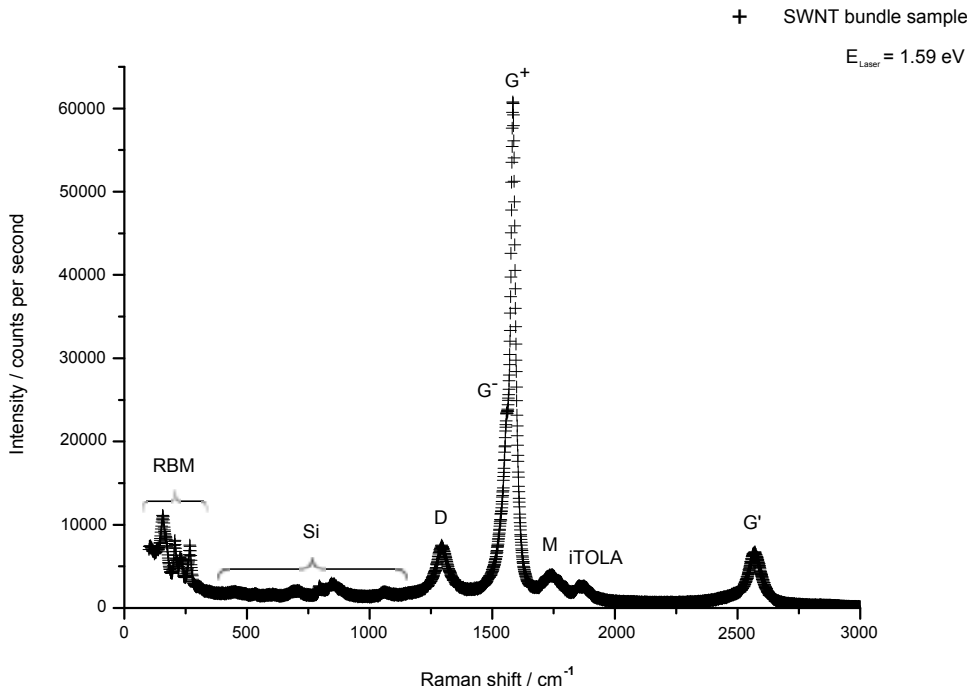

Figure 6.2: Resonant Raman spectrum from a Nanocyl NC1100 bundle sample. The spectrum shows the radial breathing modes (RBM), D-band, G-Band and G' band features - the weaker M-band and iTOLA second-order modes are also observed. Signals from the oxidised silicon substrate upon which the samples sit are also present.

The most common features observed in Raman spectra of SWNTs are listed in Table 6.1. Both first and second order Raman processes are present in the spectrum shown in Figure 6.2 - schematic diagrams showing the processes involved are shown in Figure 6.3.

Mode	Frequency ω_0 / cm^{-1}
RBM	0 to 350
D	1350
G^+	1590
G^-	1570
M	1760
iTOLA	1860
G'	2700

Table 6.1: Commonly observed features in the Raman spectra of SWNTs [28].

The modes of both the RBM and G bands originate from a 1^{st} order Raman scattering process. In 1^{st} order Raman scattering, one lattice phonon is created by inelastic scattering between the crystal lattice and a laser photon. A unique point of 1^{st}-order scattering is that after photo-absorption, the position in reciprocal space of the excited electron (e^-) k, should be the same as the hole (h^+) left behind, such that the wavevector of the phonon q = 0 - this process is shown schematically in Figure 6.3 (a) [80].

The D, M, iTOLA and G$'$ modes shown in Figure 6.2 and Table 6.1 all originate from 2^{nd} order Raman scattering processes. In second order Raman scattering, one phonon is produced, however, more than one scattering process is in operation - electrons are scattered also.

The phonons produced in the 2^{nd}-order processes have non-zero lattice wavevectors, such that $q \neq 0$.

While $q \neq 0$, for Raman scattering to occur it is still necessary for the phonon to return to point k, in order for the electron and hole to recombine and emit a Raman scattered photon.

There are two types of second order Raman scattering, the so called 1-phonon scattering process, where the phonon produced also elastically scatters an excited electron (Figure 6.3 (b) and (c)) - such a process is responsible for the nanotube D mode. It is possible to have both inter (Figure 6.3 (b)) or intra (Figure 6.3 (c)) valley scattering. Scattering is intra-valley if the scattering event is restricted to the vicinity of the K or K' lattice points, and inter-valley if phonon scattering takes place between K and K' or K' and K points [28].

In 2nd order scattering, two phonons are produced (Figure 6.3 (d)) [28,80].

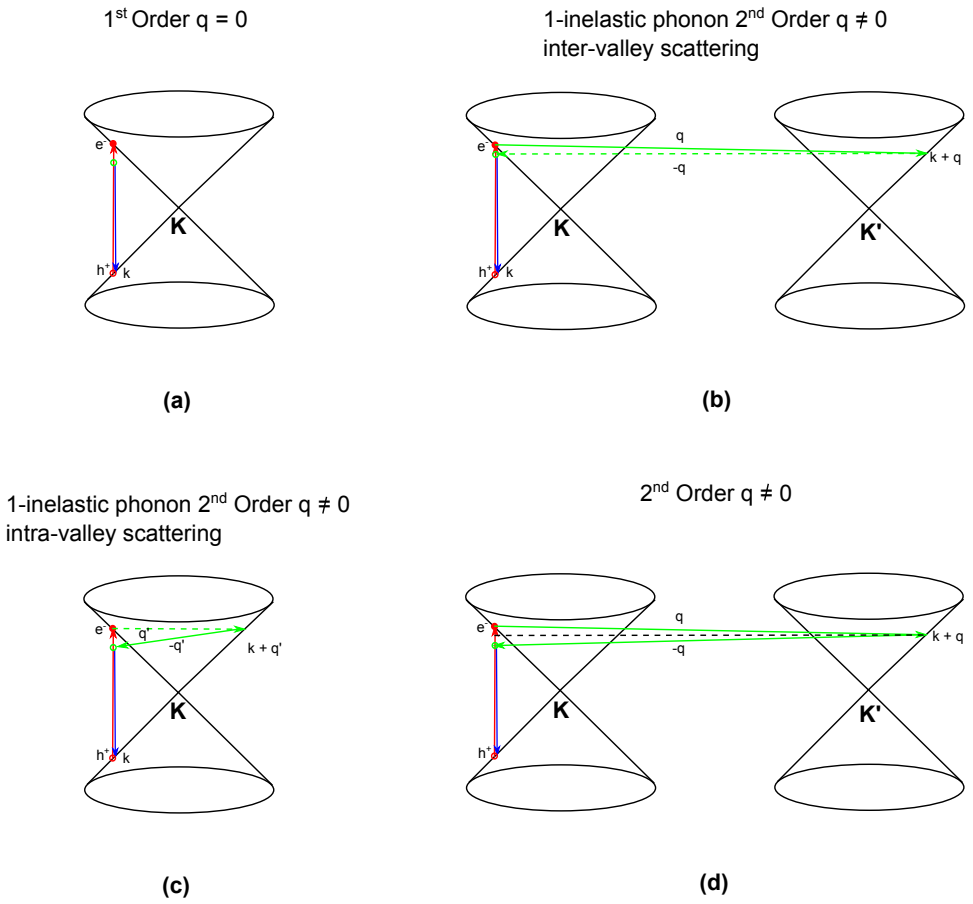

Figure 6.3: Schematic diagrams of 1st and 2nd order resonant Raman scattering processes of carbon nanotubes. Here, k is the point in reciprocal space at which the electron existed before being excited, the e^- and h^+ label the excited electron and hole created as a result of the scattering process, K and K′ are points of high symmetry in the graphene Brillouin zone; q is the wavevector of the phonons produced during the Raman scattering processes. The solid and dotted green lines represent inelastic and elastic scattering processes respectively. The black dotted line is a guide to the eye for the mid-point between two inelastic scattering processes. (a) Shows first order Raman scattering, while (b) and (c) show 1-inelastic phonon second order inter and intra valley scattering respectively; (d) shows second order scattering with two inelastic phonons (based upon [80]).

Each vibrational band will now be discussed with a focus upon the useful information which they can provide upon the mechanical and electrical properties of SWNT's. The RBM and G band features show the greatest sensitivity to molecular doping [28], therefore a great deal of attention will be given to them in the remainder of the chapter.

6.2.2 Radial breathing modes (RBM) of SWNTs - 0 to 350 cm^{-1}

The RBM of a SWNT results from the coherent oscillation of the nanotube side-walls, such that they appear to be breathing - a schematic representation is shown in Figure 6.4. They are low frequency modes and occur at Raman shifts from approximately 0 to 350 cm^{-1}.

Radial breathing modes are extremely diameter-dependent, and the Raman shift ω_{RBM} at which they occur is inversely proportional to nanotube diameter d such that the following expression is true [28]:

$$\omega_{\mathrm{RBM}} = \frac{A}{d} + B, \tag{6.10}$$

where A and B are constants to be determined experimentally. It has been found that, for SWNTs with d = 1.5 ± 0.2 nm, values of A = 234 and B = 10 cm^{-1} accurately predict the ω_{RBM} at which a SWNT of d will be located in the spectrum [28]. Here B is an up-shift to account for tube-tube interactions due to bundling. For the usual diameter range of 1.0 > d > 2.0 nm these two parameters are accurate. However, for d < 1.0 nm the constants become increasingly less valid, this because curvature effects begin to have a significant effect on the SWNT properties. In addition, for SWNT with d > 2.0 nm, accurate assignment of the ω_{RBM} becomes increasingly difficult as d gets larger; this is because the intensity of the RBM feature is weak [28].

The diameter distribution of Nanocyl nanotubes used in this study is peaked at 2.0 nm [60]; this means that the RBMs of the SWNTs at and above the peak diameter will be difficult to observe and that the majority of the observable RBMs will come from SWNTs on the lower diameter side of the distribution.

If the allowed electronic transitions of the SWNTs being probed are known, the above equation can be used to determine the diameters of SWNTs present in a mixed sample of SWNTs and whether or not they are in resonance with the probe laser.

Radial breathing modes of high intensity indicate that a large number of SWNTs of a particular diameter are in resonance with the laser.

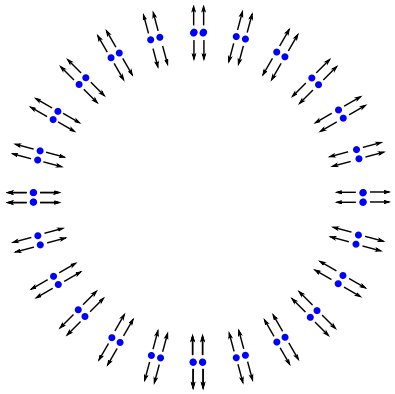

Figure 6.4: Schematic diagram of the motion of the atoms in a carbon nanotube undergoing radial breathing [81].

RBM data analysis

A spectrum showing the RBM modes of a typical SWNT bundle is shown in Figure 6.5. It can be seen from this graph that the RBMs have a low value of the Raman shift and extend from approximately 100 to 350 cm^{-1} - the low wavenumber cut-off (100 cm^{-1}) is due to the notch filter used in the experiments. The line-shape of an individual SWNT RBM is symmetrical and possesses a Lorentzian character [28]. The RBM spectrum of a sample containing many individual SWNTs can be fitted well by the superposition of a number of Lorentzian line shapes. The typical RBM spectrum shown in Figure 6.5 is fitted very well by a superposition of seven Lorentzian lineshapes centred at 104 cm^{-1}, 131 cm^{-1}, 163 cm^{-1}, 210 cm^{-1}, 234 cm^{-1}, 268 cm^{-1} and 305 cm^{-1}. However, the broad peak centred at 104 cm^{-1} is likely to be due to a background from Raleigh scattering. The small peak centred at 131 cm^{-1} may be real but its proximity to the Raleigh background makes the fitting dubious. Using equation 6.10, the diameters of these SWNTs are calculated to be 2.5 nm, 1.9 nm, 1.5 nm, 1.2 nm, 1.0 nm, 0.9 nm and 0.8 nm respectively.

This data fitting allows for accurate indentification of position, width and relative intensity of the RBM's. Both the RBM's originating from metallic and semiconducting SWNT's can be fitted by Lorentzian line shapes.

It has been found that no significant shifts in the peak positions of RBMs occur due to bundling of the SWNTs [82].

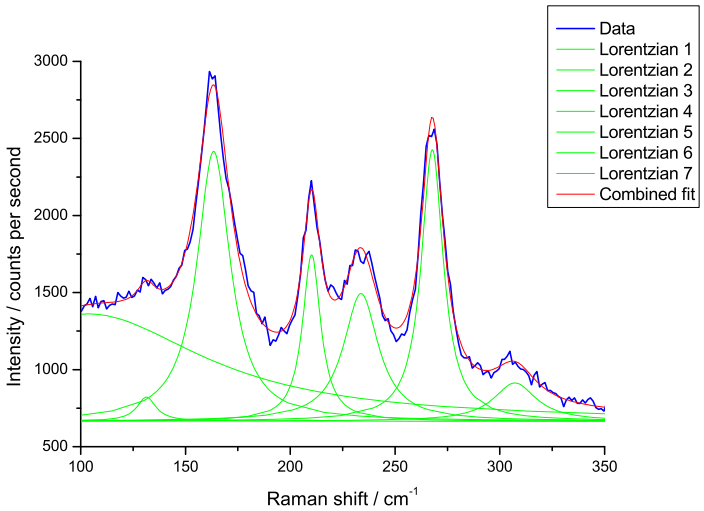

Figure 6.5: The RBMs of a resonant Raman spectrum acquired from a Nanocyl NC1100 bundle sample with a laser with E_{Laser}=1.59 eV. The spectrum shows seven distinct radial breathing modes, each fitted with a Lorentzian line-shape.

6.2.3 The G band of SWNTs - ≈ 1580 cm^{-1}

The G mode of a SWNT is a result of the vibration of the carbon atoms that make up the frame of the nanotube. The G mode in graphite results from optical phonons between two dissimilar carbon atoms (i.e. one atom from each sub-lattice see section 2.2.1) in the graphene unit cell. In graphitic materials the G mode exhibits a single Lorentzian shaped peak at 1582 cm^{-1} which is related to in-plane vibrations of the carbon atoms [28].

In carbon nanotubes the picture is more complicated - instead of a single vibrational mode there is a band formed from a number of sub-modes, the two most intense modes are labelled G^+ and G^- [28]. The G^+ mode results from the vibrations of carbon atoms along the length of the nanotube and is generally peaked at ≈ 1590 cm^{-1}.

The slightly lower frequency G$^-$ mode is generally found at $\approx$ 1570 cm^{-1} and results from vibrations of carbon atoms along the circumferential direction of the SWNT - a schematic representation of the direction of vibration of the carbon atoms in the G^- and G^+ nanotube modes is shown in Figure 6.6.

The lower intensity peaks of the G band, such as those located at approximately 1526 and 1606 cm^{-1}, result from phonons belonging to symmetry groups, such as the E_2 group, that do not couple as well to the incident laser photons.

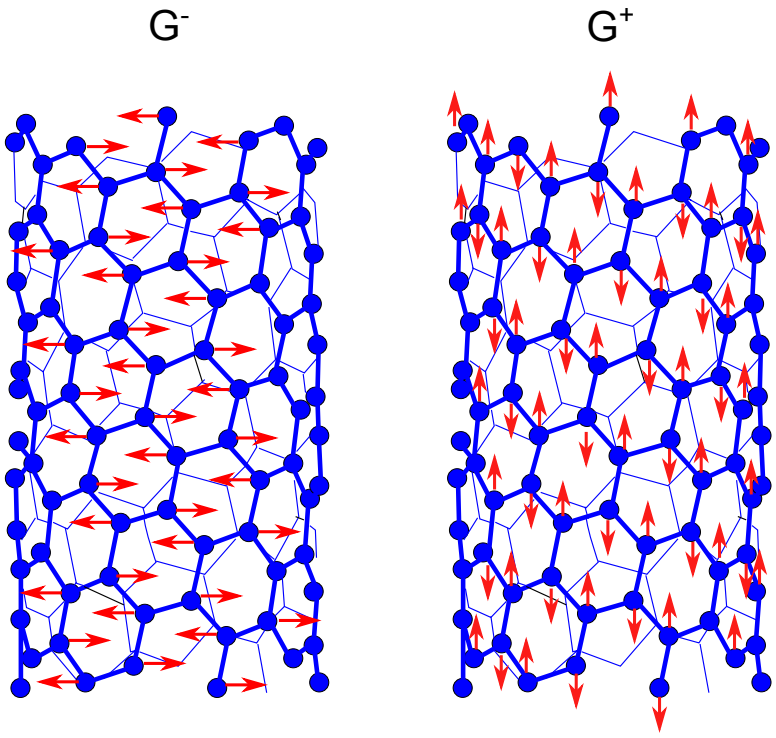

Figure 6.6: Directions of vibration of carbon atoms in the G^- and G^+ Raman modes (based upon [83]).

G band analysis

In a SWNT bundle one can expect to find nanotubes of various diameters and electronic types. Unlike in the RBM mode case, the modes of the G band have to be fitted differently depending upon whether the metallic or semiconducting SWNTs are present - the metallic and semiconducting G bands are quite dissimilar in both appearance and position. Two examples of resonant Raman spectra of individual semiconducting and metallic SWNTs are shown in Figure 6.7.

The two most intense modes of the G band are the G^- and G^+ modes. The G^- and G^+ modes of a semiconducting SWNT can be fitted well by two Lorentzian lineshapes with the G^+ and G^- modes centred at approximately 1570 cm^{-1} and 1590 cm^{-1} respectively [28]. It can clearly be seen from the figure that the intensity of the G^+ mode is far greater than that of the G^- mode - this is a typical feature of semiconducting G bands. In order to obtain a good fit to the entire G band of semiconducting nanotubes it is necessary to include a number of weaker modes such as those centred at 1554 cm^{-1} and 1601 cm^{-1} [28].

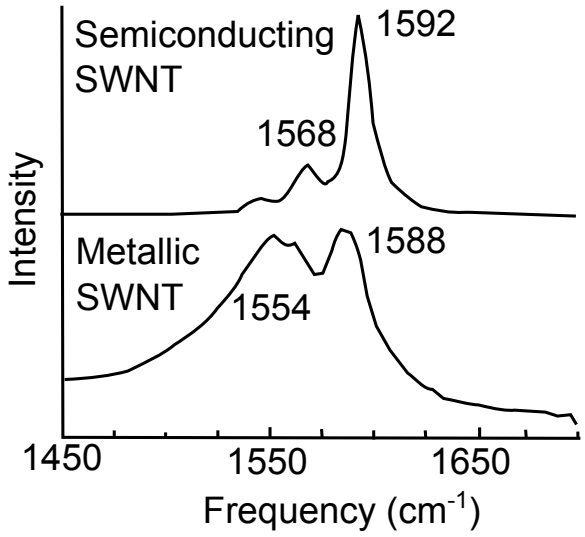

Figure 6.7: G bands for individual semiconducting and metallic SWNTs (based upon [28]).

In contrast to the G band of a semiconducting SWNT, the G band of metallic SWNTs require two dissimilar lineshapes to be used to fit the band effectively. The metallic G^+ mode is symmetrical and can be fitted by a Lorentzian line shape centred at approximately 1588 cm^{-1}, a clear down-shift relative to the equivalent semiconducting peak. The G^- mode is asymmetric, tailing towards low Raman shift and is centred at approximately 1550 cm^{-1} - in contrast to the semiconducting G^- mode, the metallic counterpart often possesses an intensity equal to or greater than that of the G^+ mode. The G^- mode can be fitted by an asymmetric Breit-Wigner-Fano (BWF) lineshape - the BWF line shape shape results from coupling of the discrete phonons to an electronic continuum [84]. This holds for bundled nanotubes as is the case for the nanotubes used in this study. The presence or lack of a BWF profile would help to discriminate from the semiconducting bands in this region.

The clear differences in line-shape and peak positions between the two electronic types of SWNTs mean that the type of an individual tube can be easily identified by its G band. When the two different electronic types are mixed, as with a bundled sample, the resulting G band will be formed from a mixture of lineshapes of the G bands of the two types. The extent to which one type will dominate the spectrum over the other will depend upon which is closest to resonance with the laser excitation energy. The G band of a mixed bundle sample is shown in Figure 6.8.

A number of observations can be made from this spectrum, firstly that the modes of both semiconducting and metallic SWNTs are present in the G band of the bundle and the combined fit matches the experimental data very closely. The G^- (BWF fitted line) and G^+ modes assigned to metallic nanotubes are positioned at 1540 cm^{-1} and 1570 cm^{-1} respectively; the modes assigned to semiconducting nanotubes are positioned at 1564 cm^{-1} and 1594 cm^{-1} respectively.

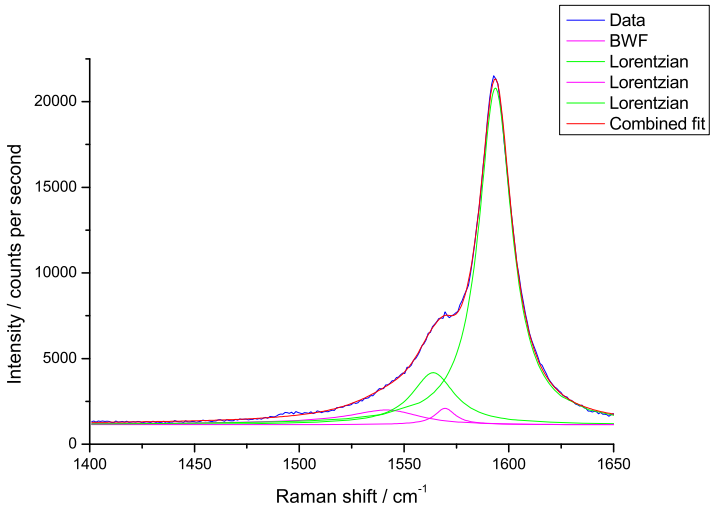

Figure 6.8: The G band of a resonant Raman spectrum acquired from a Nanocyl NC1100 bundle sample with a laser with $E_{Laser} = 2.34$ eV. The spectrum shows four distinct modes, two G^+ and two G^- modes. The two modes belonging to metallic nanotubes (shown in magenta) are of low intensity when compared with the dominant semiconducting modes (shown in green).

The G^- (BWF fitted line) and G^+ modes assigned to metallic nanotubes are positioned at 1540 cm^{-1} and 1570 cm^{-1} respectively; the modes assigned to semiconducting nanotubes are positioned at 1564 cm^{-1} and 1594 cm^{-1} respectively. The positions of the G^- and G^+ modes assigned to semiconducting nanotubes match very well with the example shown in Figure 6.7. However, the modes assigned to metallic nanotubes do not match as well. This is most probably due the difficulty of fitting the metallic modes to a spectrum where the semiconducting modes are much more intense. The dominance of the semiconducting modes implies that there are a greater number of semiconducting SWNTs in resonance with the laser.

6.2.4 The D band of SWNTs - ≈ 1350 cm^{-1}

The SWNT D band (see Figure 6.2) results from the vibration of sp^3 hybridized carbon atoms and as such is an indication of the amount of disorder in the nanotubes structure. The intensity of the D mode is usually compared to that of the G^+ mode, a large value of D/G would be a indication of a significant amount of disorder in the nanotube.

6.2.5 The effects of doping on the vibrational modes of SWNTs

The SWNT Raman bands highlighted in this chapter are all sensitive to doping, with the different types of doping causing changes in either the position or intensity of the sub-modes. There are two ways in which SWNTs are routinely doped, n-type doping where electrons are transferred from the dopants to the SWNT and p-type doping where the opposite occurs. The other mechanism which can affect the Raman modes of SWNTs is the method by which the dopant molecules are attached to the structure of the SWNT. Dopants can be attached by either covalent bonding or in the case of aromatic dopant molecules by π-π stacking (see section 3.1). The types of doping and the mechanisms by which the dopants are attached to SWNTs will now be discussed in detail with a focus upon how the SWNT Raman-active modes are affected.

Attachment mechanisms

It has been observed in a number of studies that covalent bonding between dopant atoms or molecules and the side-walls of SWNTs resulted in a significant increase in the intensity of the SWNT D band [85–90]. This increase in intensity has been explained in terms of a disruption to the hexagonal structure of the SWNT side-walls caused by the change from sp^2 to sp^3 hybridized bonding [87, 89].

In contrast to covalent bonding, π-π stacking between aromatic dopant molecules and SWNT side-walls was found not to affect the intensity of the SWNT D band [89].

By comparing the ratio between the SWNT D and G bands before and after dopant molecules are bonded to SWNTs it is possible to determine which type of bonding has occurred.

Doping effects

Changes in both the positions and intensities of SWNT G^- and G^+ have been observed when p-type dopants were added to the sidewalls of SWNTs [91–93]. Up-shifts in the positions of both the G^- [91] and G^+ modes ranging from $3 - 9$ cm^{-1} were observed in both semi-conducting and metallic SWNTs upon doping [91–93]. These up-shifts in the positions of the G modes were attributed to electron transfer from the SWNTs to the dopants [92,93]. They have been explained in terms of a hardening or stiffening of the sp^2 hybridized bonds between the carbon atoms in the structure of the SWNTs [93].

In addition to the peak up-shifts observed in both types of SWNT, a significant decrease in the intensity of the G^- mode of metallic SWNTs was also detected [91, 93]. In one case, where SWNTs were filled with nickel halogenides, unfilled SWNTs showing a metallic signature were observed to change to semiconducting upon doping with the filling [91], a clear indication of significant charge transfer. There is also some evidence of p-type doping resulting in decreases in the intensities of RBMs originating from metallic SWNTs [91].

In similarity to p-type doping, changes in the position and intensities of SWNT G modes were observed when n-type dopants were attached to the nanotube side-walls. However, in contrast to the p-type doped SWNTs, n-type doped SWNTs show a down shift in the positions of the G^- [94–98] and G^+ [95–98] modes. These peak shifts range from $1 - 10$ cm^{-1} and $1 - 5$ cm^{-1} of the G^- and G^+ modes respectively [94, 96–98].

These charge-transfer related down-shifts in peak position have been explained in terms of a weakening of the sp^2 hybrized bonds between the carbon atoms in the nanotube structure [95, 96, 98].

In contrast to p-type doped metallic SWNTs, the intensity of the G^- modes of n-type doped SWNTs were found to be significantly enhanced upon doping [91, 95, 96, 98] - this again was attributed to charge transfer. The increase in intensity has been explained in terms of a greater number of valence electrons being available for interaction with SWNT phonons [97].

In conclusion, through careful analysis of the positions and intensities of the SWNT G and RBM bands before and after doping it is possible to determine whether charge transfer has occurred and which type of doping is in effect.

6.2.6 Resonance conditions

In a sample of SWNTs with a range of diameters present, only those which have allowed energy transitions matching the energy of the probe laser will resonate.

The resonant Raman spectra shown in this chapter were acquired using a Renishaw inVia Raman Microscope with a laser emitting light with a single photon energy of E_{Laser} = 1.59 eV with a maximum power of 350 mW, a laser emitting light with a single photon energy of E_{Laser} = 2.34 eV with a maximum power of 350 mW and a laser emitting light with a single photon energy of E_{Laser} = 3.83 eV with a maximum power of 300mW, attached.

The Renishaw spectrometer was operated with a 20x microscope objective lens when the 1.59 and 2.34 eV lasers were used; the area of the laser spot at the point of focus on the sample for these two lasers was 50 μm^2, resulting in an energy density of 7.0 x 10^9 Wm^{-2} on the sample.

When the 3.83 eV laser was used, the Renishaw spectrometer was operated with a 40x ultra violet compatible microscope objective lens; the area of the laser spot at the point of focus on the sample was 45 μm^2, resulting in an energy density of 6.7 x 10^9 Wm^{-2} on the sample.

The calculated energy densities assume no power loss from the laser beam as it passes through the various optical components of the spectrometer; however, in practice, such losses will occur. The losses will be greater for the ultra violet light of the 3.83 eV laser due to the higher absorption of U.V. by some of the components.

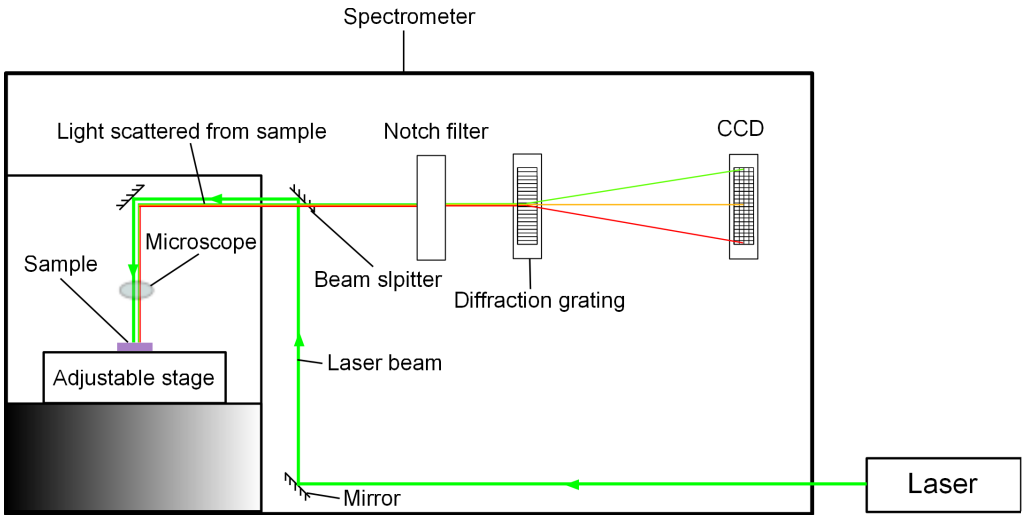

Figure 6.9: A schematic diagram of the Raman spectrometer used in this study. A laser beam is shown in green and the light back-scattered from the sample is shown multi-coloured.

The spectrometer used to acquire the Raman data analysed in this study is shown schematically in Figure 6.9.

The beam from the laser enters the spectrometer where it is deflected by mirrors to reach a beam-splitter - this deflects majority of the light from the beam through the microscope of the system to arrive at the sample which sits upon an adjustable stage.

Light which is back-scattered by the sample (both Rayleigh and Raman scattering) enters the microscope, passes back through the beam splitter and is then incident upon a notch filter - the notch filter attenuates greatly the comparatively intense Rayleigh-scattered light and lets through the lower frequency Raman-scattered light.

After passing through the notch filter, the spectral frequencies of the remaining scattered light are separated out by a diffraction grating - this light in turn falls upon a charge coupled device (CCD) where the intensities of the individual spectral frequencies are recorded. The data from the CCD is processes by software installed on the PC of the system.

Electronic considerations

The allowed transition energies in SWNTs are primarily dependent upon diameter. Using the general expression for the energy dispersion for SWNTs (see section 2.3.3) it is possible to calculate the allowed electronic transition energies of individual SWNTs using their n and m numbers and plot them as a function of nanotube diameter. Such a graph is known as a Kataura plot. An example Kataura plot [99] is shown in Figure 6.10 (a). In this plot the allowed transition energies of a large number of SWNTs have been plotted as a function of diameter.

A Kataura plot covering the range of diameters and laser excitation energies used in a study is very useful in enabling one to identify the electronic type (i.e. metallic or semiconducting) of a SWNT with a certain diameter which is in resonance with particular laser excitation energy.

The carbon nanotubes used in this study are Nanocyl NC1100 SWNTs [60]. They were grown using a carbon vapour deposition (CVD) technique and have an average diameter of 2.0 nm [60] - an example diameter distribution for these nanotubes is shown as a blue curve on the modified Kataura plot shown in Figure 6.10 (b). This curve is based upon a Gaussian function fitted to the diameter distribution of the CVD grown SWNTs of reference [61]. When used in conjunction with a Kataura plot like that shown in Figure 6.10 (a) it is possible to identify the electronic types of the SWNTs likely to be in resonance with a particular laser by matching up the nanotube diameters (d) with the photon energy of the laser E_{Laser}. However, it is also necessary to take the bundled state of the nanotubes into account. Calculations have shown that the van Hove singularities of SWNTs are shifted by as much as 100 meV upon aggregation into bundles [100]. Practically, this is observed as a red-shift in the absorption spectra of bundles of nanotubes [101]. This means that the allowed transition energies of individual SWNTs shown in the Kataura plot (Figure 6.10 (a)) are 0.1 eV higher than what would be expected for bundled nanotubes - this has been taken into account in the modified Kataura plot shown in Figure 6.10 (b).

This will affect which nanotube diameters are in resonance with the laser, although it can be seen from the Kataura plot that the electronic type (semiconducting or metallic) of nanotube in resonance will be the same.

In addition to the effects of nanotube bundling, it is also necessary to include the nanotubes which are in resonance with the outgoing photon scattered from the nanotube G modes, of energy E_{ii} = E_{Laser} - E_{phonon}, with $E_{phonon} \approx 0.2$ eV [102]. Bands have been added to the modified Kataura plot shown in Figure 6.10 (b) to account for this.

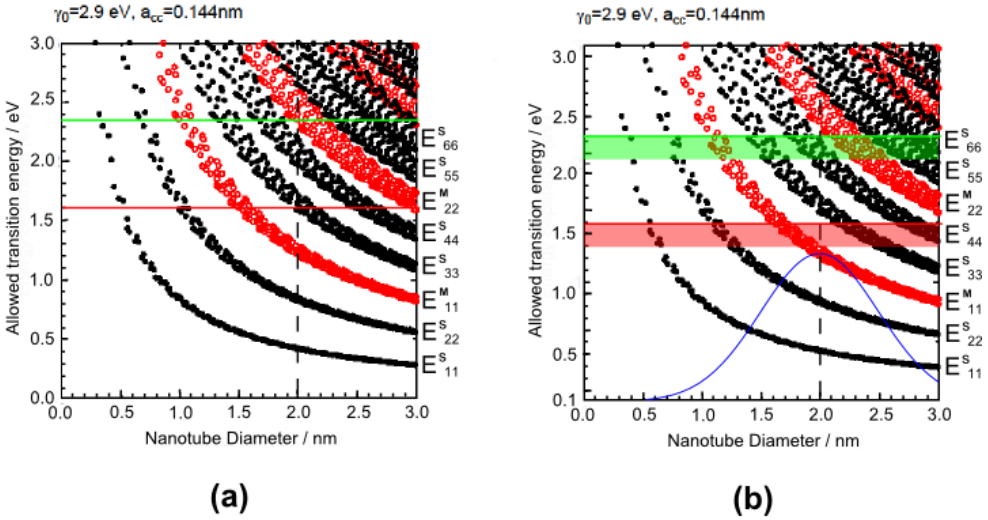

Figure 6.10: (a) The allowed electronic transition energies E_{ii} vs. nanotube diameter d for SWNTs calculated using the nearest-neighbour tight binding method, with the transfer integral γ_0 = 2.9 eV , the carbon-carbon distance $a_{C\text{-}C}$ = 0.144 nm, and neglecting nanotube curvature effects (based upon [99]). The superscript of the energy, E, refers to either semiconducting (S) or metallic (M) nanotubes, while the subscript refers to the electronic transition from the initial state (i) to a symmetric final state (i). The closed black and the open red circles indicate semiconducting and metallic SWNTs respectively. The red and green lines indicate the excitation energies of the red and green lasers used to probe the samples. (b) In this diagram, the plot has been shifted down by 0.1 eV to take into account the increase in the energy of the electronic transitions due to nanotube bundling. The laser lines have been replaced by bands to represent the possibility of resonant scattering between the nanotube electronic transitions and the Raman scattered photons from the G modes. A curve based upon a Gaussian fit to the CVD nanotubes of [61], has been included in blue to indicate the nanotube diameters which will contribute most to resonance.

The photon energies of the red (E_{Laser}=1.59 eV) and green (E_{Laser}= 2.34 eV) lasers used in this study have been added to Figure 6.10 with the appropriate colours.

(i) E_{Laser} = 1.59 eV It can be seen that with a d ≈ 2.2 nm the E^{S}_{33} semiconducting allowed transition energy will be in resonance with the red laser. With this in mind, one would expect the resonant Raman spectra acquired using this laser to have a predominantly semiconducting character. However, it is likely that there may also be a contribution from the E^{M}_{11} allowed transition originating from metallic SWNT with diameters of ≈ 1.7 nm which might lend the spectra some metallic character.

(ii) E_{Laser} = 2.34 eV The photon energy of the green laser is greater than that of the red laser. At this higher energy the SWNT allowed transition energy bands are much more tightly bunched. It can be seen from the figure that the resonance window is centred between the E^{M}_{22} metallic and E^{S}_{44} semiconducting transitions and therefore it is likely that the Raman spectra acquired using this laser will have a mixed character. Due to the tight bunching of the allowed transitions it is likely that significant contributions will also originate from the E^{S}_{44} and E^{S}_{33} semiconducting allowed transitions of SWNTs with diameters of slightly less than or greater than 2.0 nm. With this in mind one would expect resonant Raman spectra acquired with a green laser to have a mixed character with contributions from both semiconducting and metallic SWNTs, but the semiconducting character will probably dominate.

(iii) E_{Laser} = 3.83 eV A U.V. laser with a photon energy of 3.83 eV was also used in this study. This energy is beyond the range of the Kataura plot shown in Figure 6.10, however, SWNT transitions exist at this energy. At this energy the SWNT electronic transitions are even more tightly packed. As a result it is likely that in similarity to the situation with the green laser the resonant Raman spectra acquired using the U.V. laser will be composed of contributions from both semiconducting and metallic SWNTs.

Modal considerations

When considering the expected resonant Raman spectra one would expect to acquire for a SWNT sample containing a range of diameters it is necessary to bear in mind the resonance of the individual bands.

For example, in the case of the SWNTs used in this study, the largest contribution to the Raman G bands will originate from SWNTs with a diameter of approximately 2.0 nm. Intuitively, one might expect the same to be true for the RBM band, however, this is not the case. It was mentioned in section 6.2.2 that the RBMs of SWNTs with diameters of greater than 2.0 nm do not resonate well [28], with the intensity of the mode varying inversely to nanotube diameter. Therefore, the strongest modes will originate from SWNTs with d $<$ 2.0 nm.

6.3 Experimental considerations

Nanocyl SWNTs were functionalized both endohedrally using the $ScCO_2$ method, and exohedrally using a solution mixing method (see chapter 4, section 4.6). The molecules used to form the SWNT/molecules samples are those described in chapter 4, section 4.6.

These two methods were utilised to produce powders of SWNTs filled and covered with molecular systems respectively. After a washing process to remove any excess molecules (see chapter 4, section 4.7) the hybrids of SWNTs/molecules samples were drip condensed onto SiO_2/Si substrates producing mat samples.

In this study evidence of charge transfer from the dopant molecules attached to the interior and exterior surface of the SWNTs has been sought from changes in the peak positions and relative intensities of the SWNT Raman-active modes. As such it was first necessary to investigate and discriminate the possible environmental sources which could give rise to such changes in the peak positions and hence confuse charge transfer-induced changes.

6.3.1 Environmental effects upon the resonant Raman spectra of SWNTs

In this section the environmental effects which can cause perturbations to the resonant Raman spectra of SWNTs will be discussed. There are three main environmental effects which can cause varying degrees of change to the resonant Raman spectra of SWNTs, they are: (i) effects of contact with the substrate, (ii) thermal effects and (iii) the effects of the vibrational modes of foreign systems. The latter will be discussed in a separate section.

6.3.2 (i) Effects of contact with the substrate

It has been observed at the individual SWNT level that contact with a substrate, for example silicon, can cause strain induced changes in the resonant Raman spectrum of the nanotube. This is seen as an up-shift of both the D and G bands of the SWNT, and a modification of line-shape of the G band. The RBM is unaffected [103].

The SWNT samples used in the present study are bundled and form a layer of a significant thickness on top of a SiO_2/Si substrate. The bundled nature and layer thickness make such contact induced strain effects highly unlikely and bundling will be the dominant effect.

6.3.3 (ii) Thermal effects

The environmental factor which has the most significant effect on the resonant Raman spectra of SWNTs results from fluctuations in temperature. There are a number of ways in which the temperature of a SWNT sample can induce perturbations to the acquired spectra. The most commonly reported is a downshift with increasing temperature in the radial breathing modes, D and G modes [102–111].

This effect has been observed in the spectra of SWNTs heated by a laser and by conventional means [105].

Indeed, upon laser illumination of the SWNT samples used in this study with increasing laser power, down-shifts in the peak positions of the radial breathing modes and G modes were observed. The extent of the observed down-shift was directly related to the power of the laser. Radial breathing modes and G modes acquired using a E_{Laser} = 2.34 eV laser set to a range of powers are plotted in Figure 6.10.

It can be seen from the spectra that the down-shift in peak position of both the radial breathing modes and G modes become increasingly large as the laser power is increased from 10 % to 50 % of the maximum power. It can also be seen that the maximum down-shift is more pronounced in the G mode (22 cm^{-1}) than the RBMs (3 cm^{-1}). The down-shifts in peak position have been attributed mainly to the weakening of the C-C bonds between the carbon atoms of the SWNT and weakening of the van der Waals bonds between the SWNTs forming bundles [108].

Spectra acquired from samples after they had been left to cool were found to exhibit some differences compared to the spectra acquired before the heating series was conducted. Changes were observed in the relative shapes and intensities of both the RBM and G bands, together with the appearance of additional modes in the RBM band.

The other way in which heating effects can perturb SWNT spectra is by introducing variations in the relative peak intensities of the RBMs [104, 106, 107, 109]. This effect has been observed in Figure 6.11 - as the power of the illuminating laser was increased the relative intensities of the RBMs change and in some instances, new modes appear.

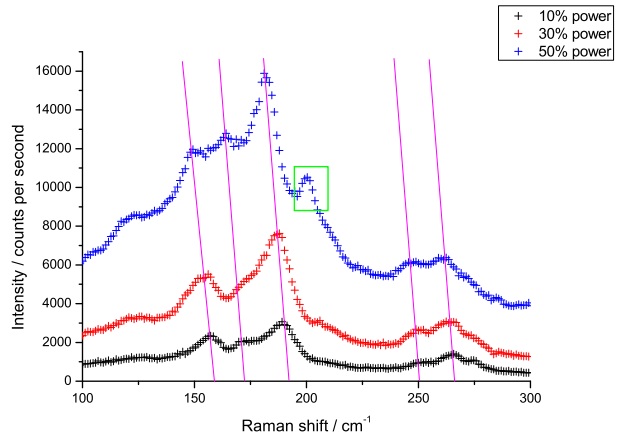

(a)

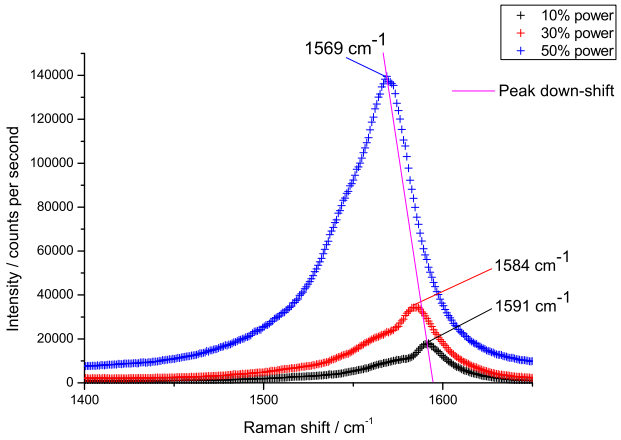

(b)

Figure 6.11: Resonant Raman spectra of unfilled SWNTs acquired using a $E_{Laser} = 2.34$ eV laser set to 10%, 30% and 50% of the maximum power. (a) and (b) show the RBM and G bands respectively. The sloping magenta lines indicate down-shifts in peak position and the green box shows a RBM mode which has been enhanced as a result of heating.

This heating effect has been attributed to thermally induced changes in the electronic density of states of the SWNTs [104, 106, 107, 109]. It has been explained in terms of the allowed transition energies of the SWNTs, E_{ii}, coming into and out of resonance with the energy of the laser, E_{Laser}. For example, if E_{ii} and E_{Laser} are in resonance, a strong RBM signal is observed. In contrast, if the SWNT is heated causing E_{ii} to decrease, the resonance with the laser can be broken and in the extreme case the mode will disappear from the spectrum. The opposite can also occur, with heating modifying E_{ii} in such a way that it is brought into resonance with E_{Laser}, thus causing a mode which was previously out of resonance to start to resonate, introducing a new mode to the spectrum.

Another factor which can affect the amount of peak shift is the thermal conductivity of the sample. At the individual SWNT level it has been observed that intimate contact between the SWNT and a SiO_2/Si substrate provides a sufficient thermal contact such that the substrate acts as a heat-sink for the SWNT and no peak down-shifts are observed. However, when the same measurements were acquired on an unsupported part of the same nanotube, thermally induced peak down-shifts, similar to those observed in bulk samples, were observed [103]. Clearly the thermal conductivity of the sample plays a big part in determining the effectiveness of the substrate as a heat-sink.

It has been observed that the amount of disorder in the sample has a significant effect upon the thermal conductivity of carbonaceous samples [105]. For example, if a SWNT sample contains a large amount of amorphous carbon the ability of the sample to conduct laser-imparted heat to the substrate is severely compromised. In bundled samples, it might be advantageous to acquire spectra from areas of the sample where the SWNT layer is thin. This might maximise the heat transmission to the substrate and minimise the heat stored in the body of the sample.

Another way in which heating effects can be minimised is by placing the sample in an aqueous solution, hence providing liquid cooling [103].

This however, is deemed too risky for powder samples, primarily due to the possibility of the solution lifting the SWNT mat off the substrate, thus ruining the sample; in addition, the Raman spectra of nanotubes have been observed to change when immersed in water [112].

In conclusion, out of the possible environmental effects which can cause perturbations to the resonant Raman spectra of SWNTs it is the temperature effects which are by far the most significant. They have been found to affect both the positions of the radial breathing, D and G modes and the relative intensities of the RBMs in bundled samples. It is therefore imperative to avoid heating effects if one is to attribute changes in peak position and intensity to non-thermal effects such as charge transfer. There are a number of ways in which the risk of heat-induced shifts can be minimised. The most obvious and effective is to use a laser set to a relatively low power coupled with a low magnification objective lens which will spread the laser spot over a larger area.

The next section will focus upon the experimental procedures which were developed to eliminate undesirable thermal effects.

6.3.4 Heating control experiments

In order to be certain that any changes in the SWNT spectra were due to SWNT-molecule interactions, it was first necessary to rule out the influence of heating effects. The procedure by which this was achieved is described below.

It was mentioned in section 6.3.3 that the position of the G band is very sensitive to heating, therefore it presents the ideal mechanism by which heating can be detected. In order to determine the position of the G band in the absence of heating effects, a resonant Raman spectrum was acquired from an unmodified SWNT sample using a 2.34 eV laser set to a very low power of 0.1% of the maximum laser power (350 mW) and a short acquisition time of 1 second. It can be seen from the spectrum acquired (Figure 6.12) that the G peak position is 1596 cm^{-1} - this agrees with the expected peak position of a semiconducting SWNT.

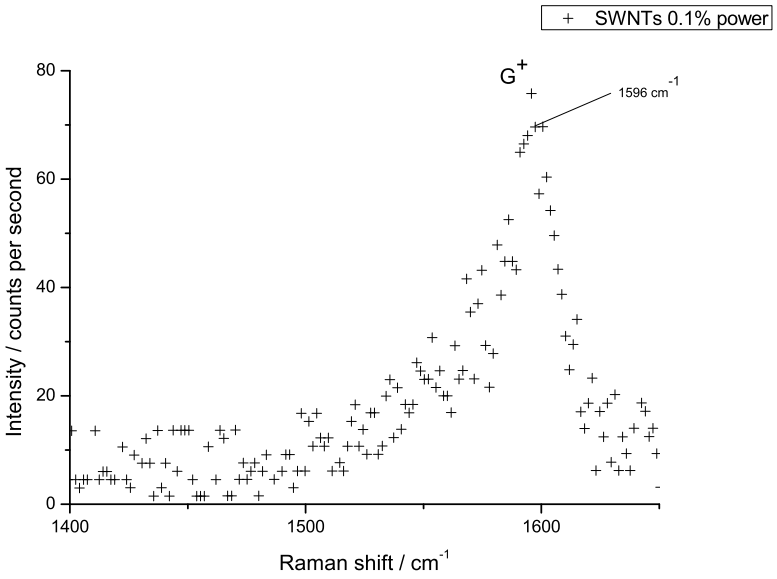

Figure 6.12: Resonant Raman spectra of unfilled SWNTs acquired using a 2.34 eV laser set to 0.1 % of the maximum laser power with an acquisition time of 1 second.

In order to determine the largest intensity that could be used without causing heating a series of readings was taken in which the sample was illuminated by the laser for 1 second at 1% and 5% of the maximum power - the results are shown in Figure 6.13. Comparing the positions of the G^+ modes of the spectra acquired with 1% and 5% maximum power with the spectrum acquired using 0.1% maximum power (Figure 6.12), it can be seen that a large peak down-shift of 22 cm^{-1} was observed when 5% maximum power was used (a clear indication of laser-induced heating) and a small down-shift of 1 cm^{-1} was also observed when 1% maximum power was used.

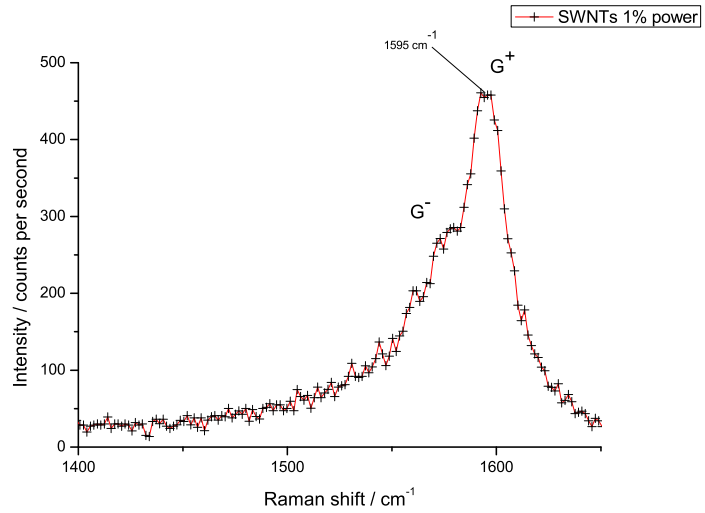

(a)

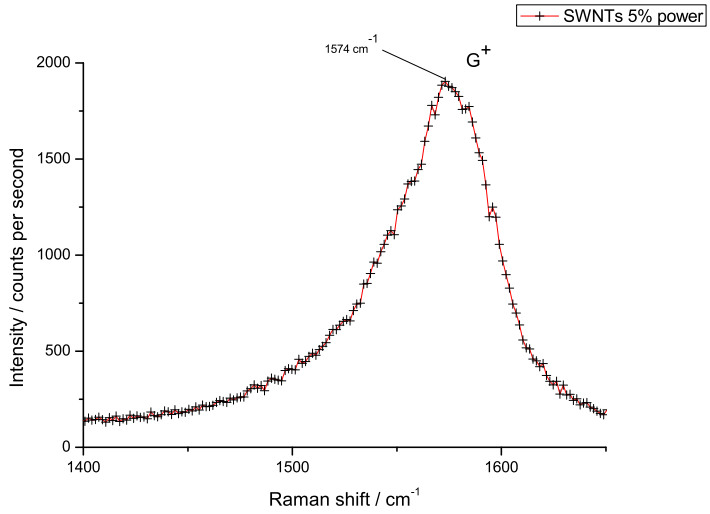

(b)

Figure 6.13: Resonant Raman spectra of SWNTs acquired using a 2.34 eV laser set to (a) 1 % and (b) 5 % maximum power and an acquisition time of 1 second.

With some fine tuning of the laser power, it was found that the highest power which did not result in a peak shift was 0.5% maximum power. An example spectrum acquired with 0.5 % maximum power for 1 second is shown in Figure 6.14 (a). This spectrum is a lot more intense than the spectrum acquired with 0.1 % maximum power (Figure 6.12), however, the signal to noise ratio is still not as high as desirable.

To improve the signal to noise ratio of the spectra, longer acquisition times were experimented with. A number of different acquisition times were tried ranging from 1 second to a few minutes. It was found that a good signal to noise ratio was obtained when an acquisition time of 30 seconds was used (Figure 6.14 (b)). It can be seen from this spectrum that there is a significant increase intensity of the G band in the 30 seconds spectra compared to that acquired using a 1 second acquisition time and the signal to noise ratio is greatly improved.

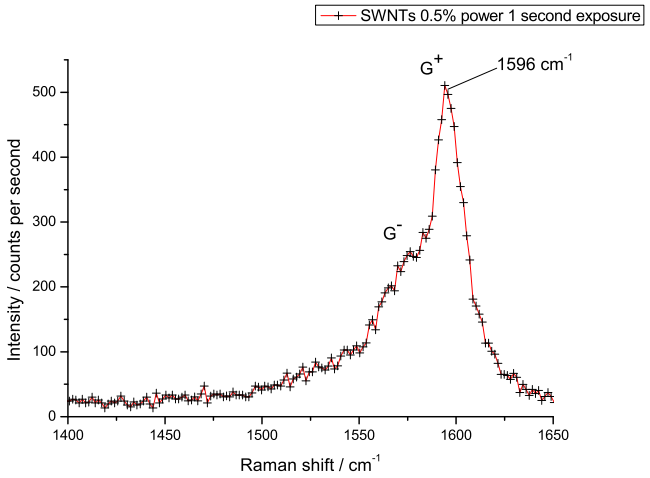

(a)

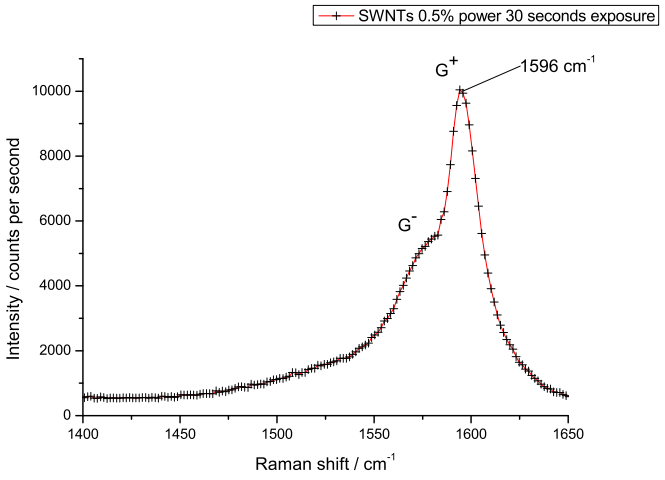

(b)

Figure 6.14: Resonant Raman spectra of SWNTs acquired using a 2.34 eV laser using 0.5 % maximum power with an acquistion time of (a) 1 second and (b) 30 seconds.

To check whether a longer exposure of the sample to the laser beam would produce a noticeable temperature change in the sample, a number of exposure series were acquired on different positions on the sample. An exposure series consisted of illuminating the sample continuously for 30 seconds and acquiring a spectrum every second. This allowed for the temporal evolution of the sample under laser irradiation to be investigated. A representative time series acquired using 0.5 % maximum power is shown in Figure 6.15 - a time series acquired using 5% maximum laser power is shown for comparison. It can be seen from this figure that the position and intensity of the G^+ mode in the component spectra of the series acquired using 0.5 % maximum power remain constant at a value of 1596 cm^{-1} over time, this implies that no significant heating effects have occured.

In contrast, the component spectra of the series acquired with 5 % maximum power is temporally dependent. Two main observations can be made from this graph - one that the intensity of the SWNT G band increases with time, as such it was not necessary to displace the spectra for clarity as in Figure 6.15 (a). Secondly, the down-shifted G^+ mode centered at 1574 cm^{-1} shows a small up-shift with time. These observations indicate that laser-induced heating is causing modification the sample with time. The fact that the changes are beneficial to the signal strength of the G band implies that the laser induced heating is burning off some of the impurities present in the sample. Such a conclusion would be consistent with more light reaching the SWNTs and hence result in a greater signal strength and fewer impurities resulting in a higher thermal conductivity of the sample resulting in a cooling-induced up-shift in the G band.

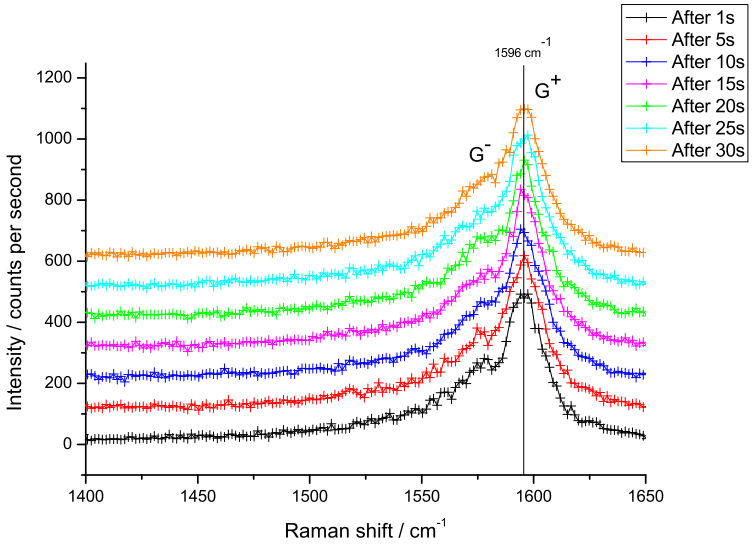

(a)

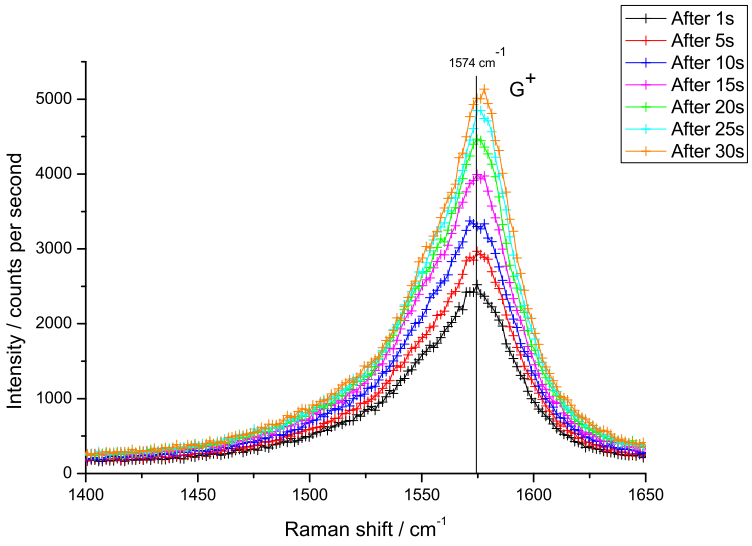

(b)

Figure 6.15: Resonant Raman spectra of SWNTs acquired using a 2.34 eV laser set to 0.5 % (a) and 5% (b) maximum power. Each coloured trace on the graphs represents a one second acquisition from the sample, with 30 being acquired from the sample for each laser power. The individual spectra shown in Figure (a) have been artificially separated along the intensity axis for clarity.

Having determined that no heat-induced changes occur after a 30 second exposure with the laser set to 0.5 % maximum power, the final effect to test was whether variations in the thickness of the SWNT layer of the sample produced noticeable changes in peak position or shape. This was probed by acquiring spectra at a number of different locations on the sample using the laser set to 0.5 % maximum power with an acquisition time of 30 seconds - some representative spectra are shown in Figure 6.16.

It can be seen from Figure 6.16 that there is little or no variation in the Raman shift of the SWNT G bands - this implies that the power and acquisition time are such that they do not cause position-sensitive effects to appear in SWNT spectra.

Similarly, the radial breathing modes do not show any noticeable change in the positions of the most intense modes; however, there are a number of minor changes to the lines-shape as one moves from position to position. This is most likely to be a result of variations in the types and diameters of the SWNTs which form the bundles in the sample. The changes in the intensity of the modal peaks are likely due to either variations in the density of the samples in different regions of the sample or differences in the focus of the laser.

In conclusion, SWNT resonant Raman spectra which were free from heating-induced perturbations were acquired using a 2.34 eV laser set to 0.5 % maximum power and set to acquire for 30 seconds.

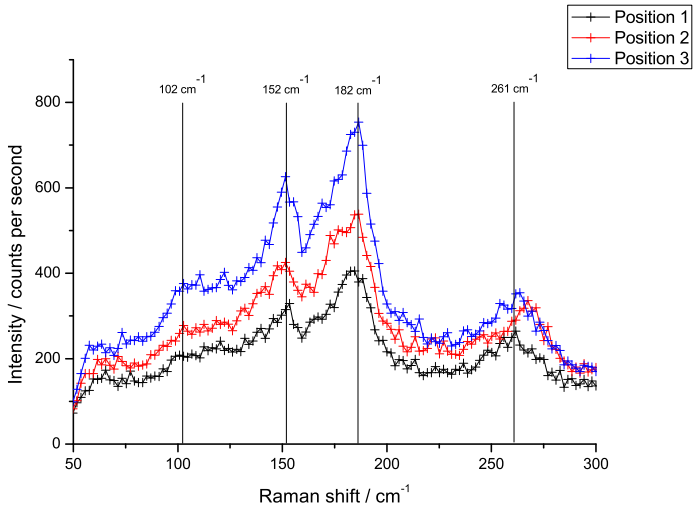

(a)

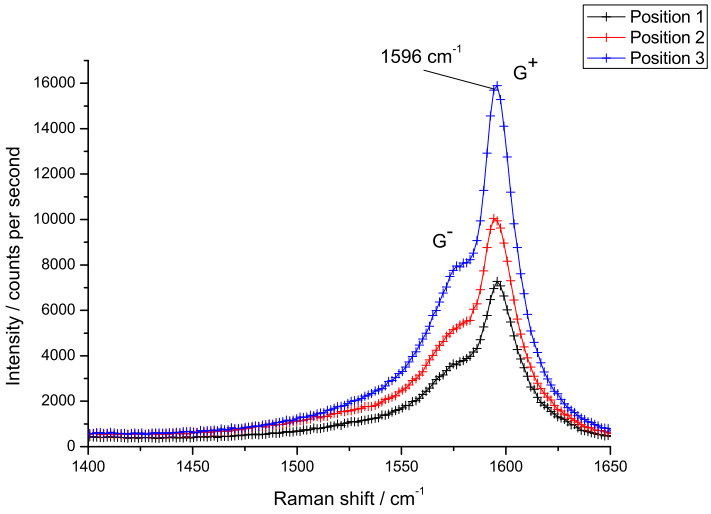

(b)

Figure 6.16: Resonant Raman spectra of unmodified SWNTs acquired using a 2.34 eV laser set to 0.5 % of the maximum laser power with an acquisition time of 30 seconds acquired from three different positions on the sample, (a) and (b) show the RBM and G bands of the spectra respectively.

The same procedure as outlined above was used to determine the optimum conditions for the 1.59 eV and 2.34 eV lasers.

SWNT spectra which were free from heating effects were acquired when the 1.59 eV laser was set to 0.5 % and 0.1 % of the maximum power (350 mW) depending upon whether the system was operated in laser spot or laser line mode respectively; and when the 3.83 eV laser was set to 5 % of the maximum power (300 mW). As discussed in section 6.2.6, the most likely reason for the need for a higher power setting for the U.V. laser is to compensate for the extra absorption of U.V. by some of the components of the spectrometer.

6.3.5 (iii) Vibrational modes of non-nanotube components

Another possible cause of perturbation to the SWNT spectra is contributions from the presence of vibrational modes originating from molecules and structures sharing the environment of the SWNTs. In the experiments conducted in this study the two main sources are the SiO_2/Si substrates upon which the samples were deposited and the molecular species with which the SWNTs were filled or covered.

Vibrational modes of silicon

Raman spectra were acquired from a SiO_2/Si substrate which is representative of those used in this study using 2.34 eV and 1.59 eV lasers and are are shown in Figure 6.17 below. It can be seen from parts (a) and (b) of the figure that the Raman spectra acquired from the silicon substrate using both laser wavelengths show sharp intense modes at 521 cm^{-1}. This is a well known vibrational mode and was used to calibrate the spectrometers used in this study. Given the sharpness and position of this mode it is unlikely that it would cause any problems in SWNT peak identification.

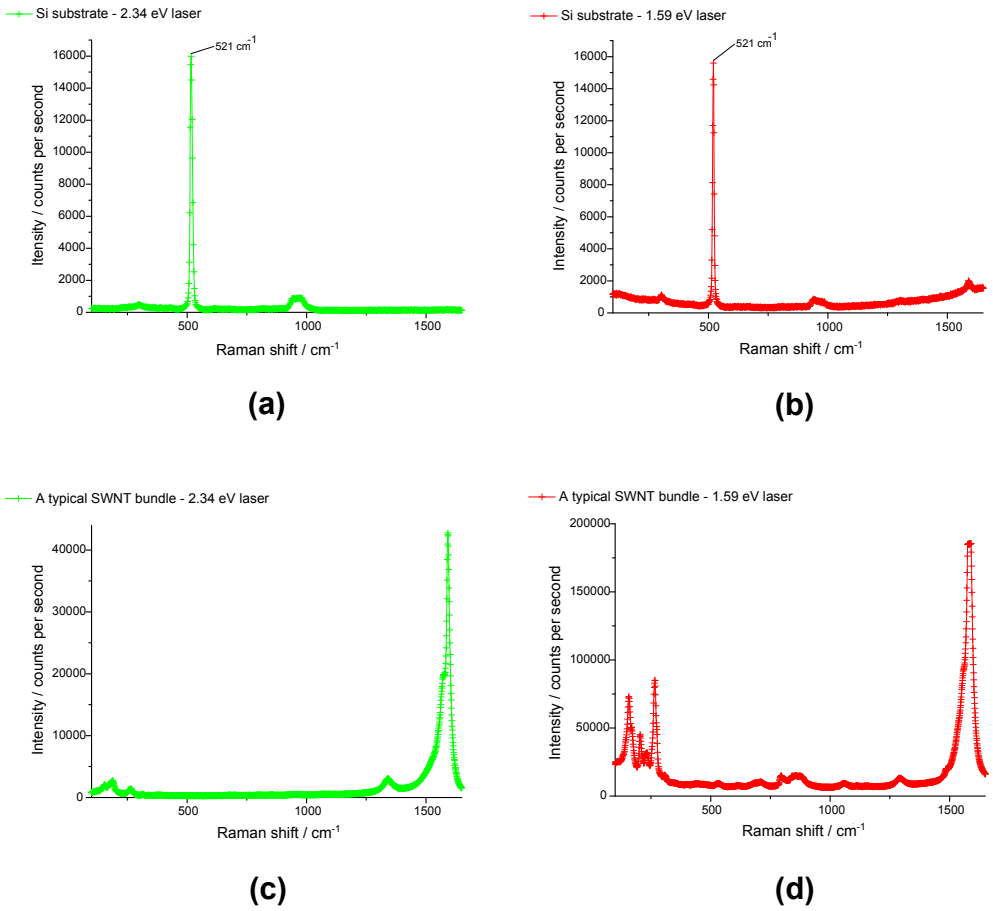

Figure 6.17: Raman spectrum of silicon acquired with a 2.34 eV energy laser (a) and a 1.59 eV energy laser (b). (c) and (d) show resonant Raman spectra from SWNTs placed on the SiO_2/ Si substrate acquired with a 2.34 eV and 1.59 eV energy laser respectively.

Resonant Raman spectra were acquired from a SWNT sample which is representative of those used in the study using 2.34 eV and 1.59 eV lasers and are shown in parts Figure 6.17 (c) and (d) respectively. It can be seen that there is no evidence of the relatively intense 521 cm^{-1} Si vibrational mode in either of the spectra. This implies that the thickness of the SWNT layer in the samples is of sufficient thickness so that little or no light reaches Si substrate upon which it is deposited. It is therefore reasonable to conclude that providing there is a sufficient covering of SWNTs, perturbations to the SWNT spectra from the substrate are unlikely.

The vibrational modes of molecular systems

The other source of vibrational modes which could disrupt the SWNT modes originate from the molecular species with which the SWNTs have been filled or covered. Raman spectra were acquired from the molecules used in this study using a 2.34 eV and 1.59 eV lasers and are shown in Figure 6.18. It can be seen that clear spectra with a high degree of spectral resolution were acquired using the 2.34 eV laser. The spectral clarity is such that the vibrational modes of the molecules can be clearly identified, meaning that any molecule peaks which appear in any of the modified SWNT spectra can be easily identified - the most intense modes have been labelled for clarity.

It can be seen from the spectra shown in parts (b) and (c) of Figure 6.18 that the phthalocyanine (Pc) molecules possess intense vibrational modes in the region of 1520 - 1545 cm^{-1} - it is these intense modes which are most likely to cause confusion in the interpretation of the SWNT G band. The vibrational modes of metallic phthalocyanines at this frequency have been attributed to stretches in the C-N-C bonds as well as expansion of the pyrrole structure coupled with C-H in-plane bending (IPB) vibrations in the molecule [113]. The position of this peak varies depending upon which metal ion is present at the core of the molecule. The Raman spectrum of the NiTPP molecule shown in part (a) of the figure show that there are no high intensity molecular vibrational modes present which might overlap with the SWNT G band.

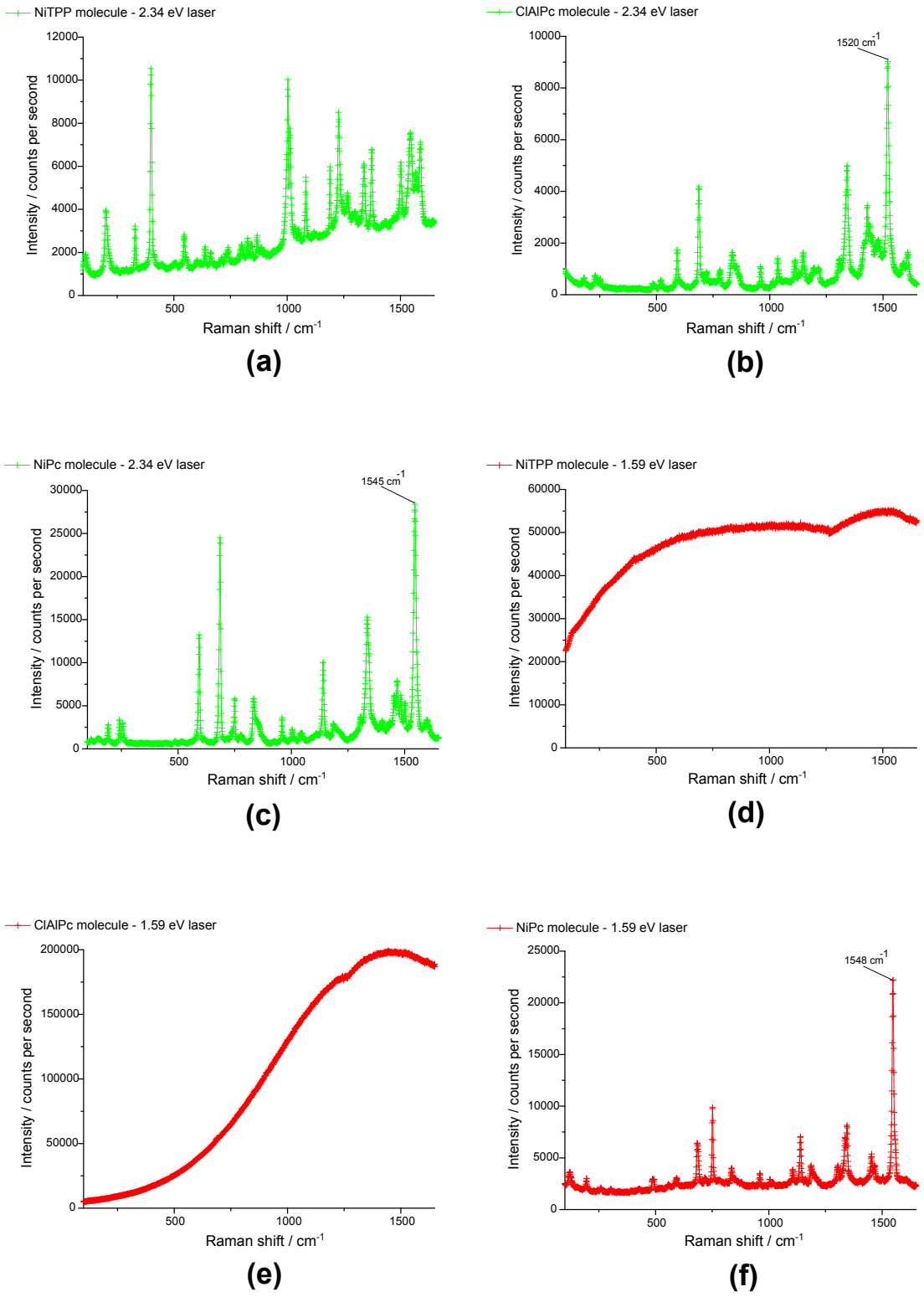

Figure 6.18: (a), (b) and (c) show Raman spectra of the NiTPP, ClAlPc and NiPc molecules respectively, acquired using a 2.34 eV laser. (d), (e) and (f) show the equivalent spectra, but acquired using a 1.59 eV laser. The molecules from which these Raman spectra were acquired were deposited onto SiO_2 / Si substrates.

Figure 6.19 (a) and (b) show a comparison between spectra acquired from a sample of un-modified SWNTs and of SWNTs with a surface covering of NiPc molecules. This particular molecular species was chosen because it was seen to provide the greatest overlap with the SWNT spectrum. It can be seen from these spectra that there are clearly some vibrational modes in the doped SWNT spectrum which are not present in the undoped spectrum, which can be attributed to the NiPc molecule. However, it can be seen that the SWNT spectrum is clearly still very dominant.

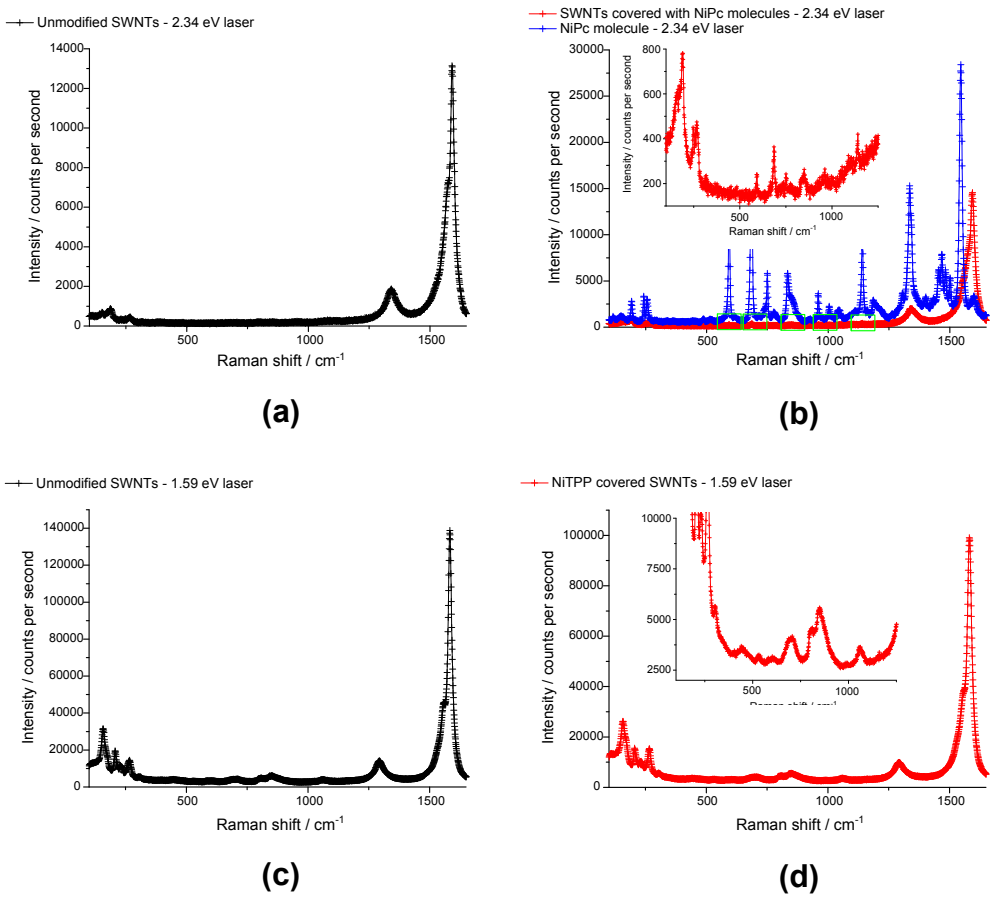

Figure 6.19: Raman spectra of (a) unmodified SWNTs and (b) SWNTs covered with NiPc molecules acquired using a 2.34 eV laser. The Raman spectrum of the NiPc molecules has been included in (b) for comparison. Areas of the modified SWNTs Raman spectrum which have been modified by the presence of the NiPc spectrum are highlighted in green boxes. The inset shows a zoomed in version of the Raman spectrum of SWNTs covered with NiPc molecules acquired using a 2.34 eV laser. (c) and (d) of the figure show Raman spectra of unmodified SWNTs and SWNTs covered with NiTPP molecules respectively- the Raman spectra were acquired using a 1.59 eV laser. The inset in (d) shows a zoomed in version of the Raman spectrum of SWNTs covered with NiTPP molecules acquired using a 1.59 eV laser.

When illuminated with a 1.59 eV laser both the NiTPP and ClAlPc molecules showed very large and intense fluorescence peaks (see Figure 6.18 (d) and (e)). These could cause a significant overlap with the SWNT spectra if a sufficient amount of molecules were present. In Figure 6.19 (c) Raman spectra acquired using a 1.59 eV laser from a sample of unmodified SWNTs and Figure 6.19 (d) SWNTs modified with NiTPP molecules are compared. It can be seen that there is little or no difference between the SWNT spectra before and after modification with NiTPP molecules, specifically, no large fluorescence features are observed, and the SWNT modes clearly dominate the spectrum.

6.4 Results and discussion

6.4.1 The SWNT G band

2.34 eV and 3.83 eV lasers have been used to probe both metallic and semiconducting nanotubes, while the 1.59 eV laser will probe predominately semiconducting nanotubes. The different laser excitation energies will only resonate with nanotubes specific diameters.

The component modes of the SWNT G band from nanotubes probed with each laser, show changes in both the positions and relative intensities of the G^+ and G^- modes upon modification of the nanotubes with organo-metallic molecules.

Changes in the peak position of these modes have been investigated to determine whether charge transfer between nanotube and dopant molecules had occured.

Spectra acquired using the 1.59 eV laser

The spectra acquired using the 1.59 eV laser were fitted well by four Lorentzian line-shapes centred at approximately 1546 cm^{-1}, 1566 cm^{-1}, 1593 cm^{-1} and 1601 cm^{-1}.

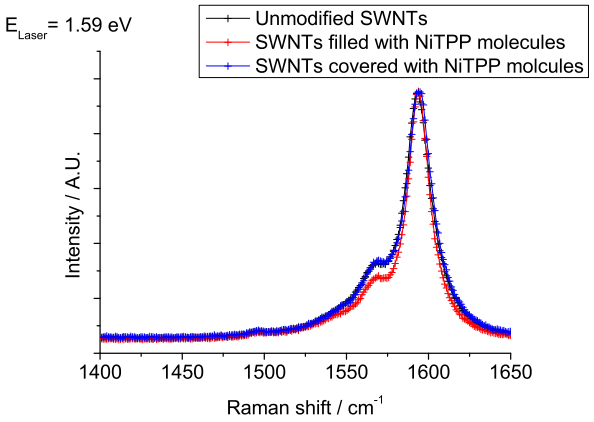

(a)

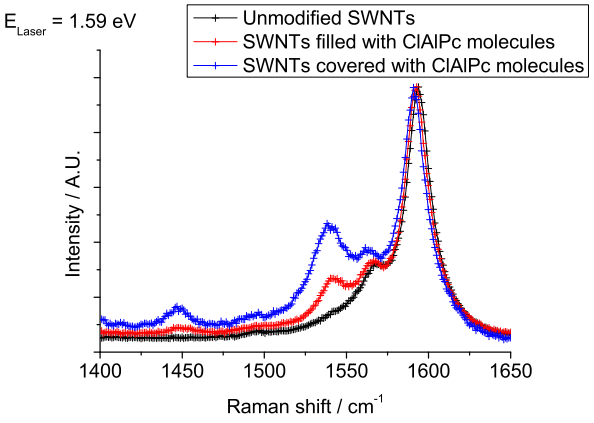

(b)

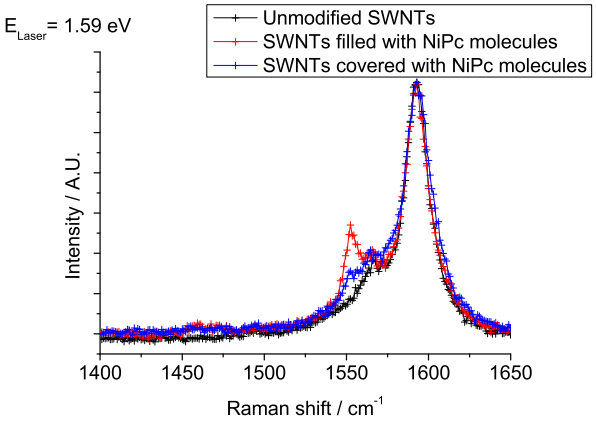

(c)

Figure 6.20: (a) to (c) of the figure show resonant Raman spectra of SWNTs filled and covered with NiTPP, ClAlPc and NiPc molecules respectively, acquired using a 1.59 eV laser. The spectra of the modified SWNTs for each molecular species have been normalized to the G^+ mode of the unmodified SWNT spectrum for clarity. The spectra of unmodifed SWNTs are shown in black as a reference.

The vibrational modes located at 1566 cm^{-1} and 1593 cm^{-1} are consistent with the G^- and G^+ vibrational modes of semiconducting SWNTs. This is in agreement with the resonance conditions described in section 6.2.6.

In order to achieve a good fit to the experimental data it was necessary to include some of the weaker modes of the SWNT G band, specifically those located at 1546 cm^{-1} and 1601 cm^{-1}. These modes are not thought to be sensitive to charge transfer, variation in the fitted peaks assigned to these modes are most likely an artefact of the data fitting process. In addition, given the low amplitude of these peaks and the lack of any well defined signatures in the G bands of the acquired spectra, it is reasonable to put a low weighting to the significance of the changes in the positions of these peaks and instead to focus upon the G^- and G^+ modes. The resonant Raman spectra acquired are shown in Figure 6.20.

It can be seen from the fitted peak positions shown in Table 6.2 that there are small up-shifts of 1 cm^{-1} in the positions of the SWNT G^- and G^+ modes upon being filled with NiTPP molecules. There is also a decrease in the relative intensity of the G^- peak relative to the G^+ peak. The SWNTs covered with NiTPP molecules also show a small up-shift of 1 cm^{-1} in the position of G^- mode, however no shift in the G^+ mode is observed and there is negligible change in the relative intensity of the G^- mode.

A comparison of the results from SWNTs filled and covered with NiTPP molecules shows that the greatest changes to the SWNT vibrational modes occur when the nanotubes are filled with molecules.

In contrast to the situation observed when SWNTs were functionalized with NiTPP molecules, down-shifts in the positions of the G^+ and G^- peaks are seen when SWNTs were modified with ClAlPc molecules.

These down-shifts are significant, down-shifts of -2 cm^{-1} in the positions both the G^- and G^+ SWNTs modes occur when they are filled with ClAlPc molecules. When covered with ClAlPc molecules even greater down-shifts of -3 cm^{-1} and -4 cm^{-1} are observed.

SWNTs modified with:	SWNT mode frequency / cm^{-1}	Additional modes / cm^{-1}	Frequency shift (filled) /cm^{-1}	Frequency shift (covered) / cm^{-1}	Relative intensity (unmodified)	Relative intensity (filled)	Relative intensity (covered)	Optimum filling diameter / nm	Intense modes of molecule in region / cm^{-1}
NiTPP								2.3	
	1546		0	-2	0.06	0.05	0.04		-
	1566		1	1	0.21	0.15	0.23		-
	1593		1	0	1.00	1.00	1.00		
	1601		-1	1	0.16	0.11	0.20		
ClAlPc								1.8	-
	1548	1539	-7	-7	0.06	0.18	0.09		
	1567		-2	-3	0.19	0.19	0.18		
	1594		-2	-4	1.00	1.00	1.00		
	1604		-1	-3	0.08	0.10	0.08		
NiPc								1.8	1548
	1557	1554	-1	-5	0.09	0.04	0.07		
	1566		-1	0	0.14	0.19	0.19		
	1593		-1	0	1.00	1.00	1.00		
	1605		0	0	0.04	0.07	0.08		

Table 6.2: 1.59 eV Excitation. Note: the intensities are relative to the intensity of the G^+ peak.

The relative intensities of the G^- modes to the G^+ modes are the same for the unmodified and filled samples, however, a small decrease is observed in the covered sample. The covered spectrum does not reflect this decrease due to the presence of an intense mode located at 1539 cm^{-1}. This mode is not present in the unfilled SWNT spectrum and is therefore is most likely due to a particularly strong Raman-active vibrational mode originating from the ClAlPc molecule. Due to strong fluorescence it was not possible to reveal a Raman spectrum from this molecule using this laser excitation, however, the spectra acquired using the 2.34 eV and 3.83 eV lasers show an intense molecular vibrational mode at $\approx$ 1520 cm^{-1} - it is likely that the 1539 cm^{-1} mode present in the filled and covered nanotube spectra is an upshift of the 1520 cm^{-1} mode which may have resulted from aggregation of the molecules. It can be seen from Figure 6.20 (b) that the relative intensity of this peak is greater for nanotubes covered with ClAlPc molecules.

For SWNTs modified with NiPc molecules, down-shifts of -1cm^{-1} are observed in the positions of both the G^- and G^+ SWNT modes upon being filled with NiPc molecules. No peak shifts are observed in the G^- and G^+ modes of SWNTs covered with NiPc molecules.

As well as the observed shifts in position, a increase of 5% in the relative intensity of the G^- peak is observed for SWNTs both filled and covered with NiPc molecules.

In similarity with the ClAlPc modified SWNT spectra, there is a significant well-defined peak located in the spectra of SWNTs modified with NiPc molecules which is not present in the spectrum of the unmodified SWNTs. This implies that this mode located at 1553 cm^{-1} originates from the NiPc molecule. Indeed, this peak matches exactly the reported position of the most intense Raman-active mode of the NiPc molecule [113]. In contrast to what is observed for the ClAlPc molecule, this peak is larger in the spectrum of SWNTs filled with NiPc molecules (see Figure 6.20 (c)).

Resonant Raman spectra resulting from a mixture of semiconducting and metallic SWNTs

Both the 2.34 eV and 3.83 eV laser excitation energies are such that they are expected to resonate with the allowed transitions of both semiconducting and metallic SWNTs. As a result, the resonant Raman spectra of the SWNT G band acquired will be formed from the superposition of vibrational modes of both electronic types.

As mentioned earlier in this chapter, the two most intense Raman-active modes of the SWNT G band are the G^- and G^+ modes. Therefore, one would expect the four most intense vibrational modes of a mixed G band to be the G^- metallic mode located at ≈ 1540 cm^{-1}, the semiconducting G^- mode located at ≈ 1570 cm^{-1}, the metallic G^+ mode located at 1580 cm^{-1} and the semiconducting G^+ mode located at ≈ 1590 cm^{-1}. However, in order to obtain a good fit to the experimental data it may be necessary to include some of the weaker modes from the semiconducting G band. The two strongest such modes are located at ≈ 1550 cm^{-1} and ≈ 1605 cm^{-1}.

The SWNT G bands shown in the spectra of Figure 6.21 are fitted well by the superposition of five Lorentzian line-shapes centred at approximately 1554 cm^{-1}, 1574 cm^{-1}, 1581 cm^{-1}, 1598 cm^{-1} and 1608 cm^{-1}.

The single broad mode centred at ≈ 1554 cm^{-1} possesses both a low intensity and a low level of spectral detail. This mode could be attributed to either a low intensity G band mode originating from semiconducting SWNTs or the G^- mode of metallic SWNTs, or a superposition of the two. An attempt was made to fit a Breit Wigner Fano function to this peak - this was found to fit poorly. This may indicate that the 1554 cm^{-1} mode has a predominately semiconducting character, however, there is insufficient detail in the spectra to identify the origin of this peak. Given the low level of spectral detail, it is reasonable to put a very low weighting upon the changes in the position of this mode.

To fit the 1577 cm^{-1} region of the G band, it was necessary to use two Lorentizian line-shapes one centred at ≈ 1574 cm^{-1} and a second centred at 1580 cm^{-1}.

The fitted peak located at 1574 cm^{-1} can be attributed to the G^- mode of semiconducting SWNTs. It possesses both the expected intensity relative to the G^+ semiconducting mode and is located at the expected position. The expected position of the metallic G^+ mode is 1580 cm^{-1}, therefore it is reasonable to assign the 1580cm^{-1} fitted peak to this mode. The amplitude of this mode is approximately equal to that of the broad mode located at 1554 cm^{-1}. This too is consistent with what would be expected in a metallic SWNT spectrum, further supporting the argument for this mode's metallic character.

The superposition of these two modes forms a shoulder to the semiconducting G^+ mode. Changes in the shape of the shoulder will result from either changes in the positions or the intensities of these modes. However, due to the close proximity of these modes it is not possible to identify the individual peaks this makes identifying their exact positions and intensities very difficult. Unfortunately, this severely degrades the reliability of the fitted positions of these peaks. As such, it is necessary to put a low weighting to individual changes in the intensities and positions of the modes.

The very intense peak located at $\approx$ 1594 cm^{-1} which dominates the G band possesses both the expected position and relatively high intensity associated with the semiconducting G^+ mode. The relatively high intensity of this mode makes identifying its position very easily and as such the position of the fitted peak can be relied upon to be accurate. It is this peak which presents the most reliable method for identifying charge transfer-induced peak shifts in mixed SWNT samples.

The relatively low intensity fitted peak at $\approx$ 1608 cm^{-1} is so close to the very intense G^+ mode that it is not possible to observe the features of this peak. Therefore, any changes in the position and or intensity of this peak are unreliable.

In conclusion, due to the lack of spectral detail in the G band spectra possessing Raman contributions from both types of nanotube, only the position of the dominant G^+ semiconducting mode can be stated with a high degree of confidence.

Therefore, changes in the position of G^+ mode located at $\approx$ 1590 cm^{-1} will be used to inform upon whether charge transfer induced peak shifts have occured.

Spectra acquired using the 2.34 eV laser

The SWNT G band spectra acquired using the 2.34 eV laser are shown in Figure 6.21 - Table 6.3 summarises the changes observed in the modes of the G band upon modification of the SWNTs with the organo-metallic molecules of the study.

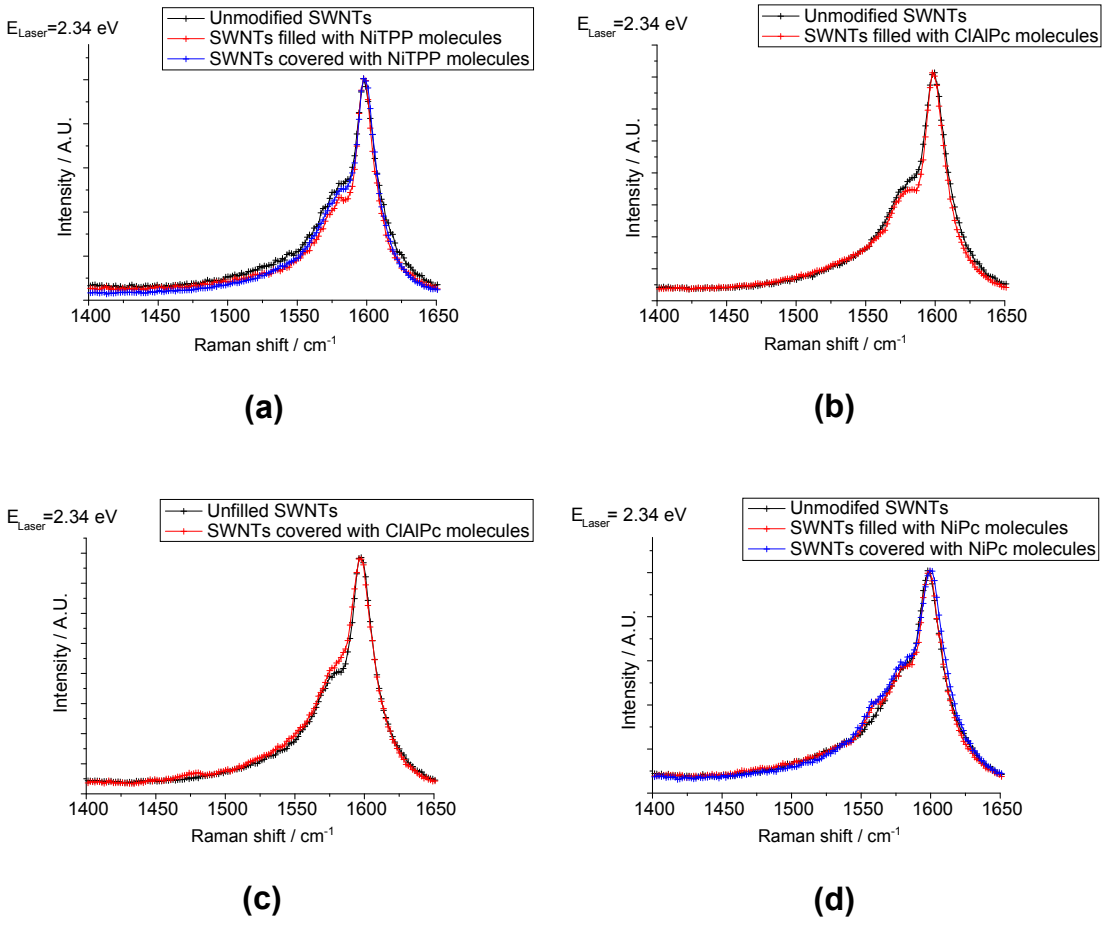

Figure 6.21: (a) to (d) show resonant Raman spectra of SWNTs filled and covered with NiTPP, ClAlPc and NiPc molecules respectively, acquired using a 2.34 eV laser. The spectra shown in (b) and (c) were acquired on different days and therefore could not be plotted on the same graph. The spectra of unmodifed SWNTs are shown in black as a reference.

SWNTs modified with:	SWNT mode frequency / cm^{-1}	Additional modes / cm^{-1}	Frequency shift (filled) /cm^{-1}	Frequency shift (covered) / cm^{-1}	Relative intensity (unmodified)	Relative intensity (filled)	Relative intensity (covered)	Optimum filling diameter / nm	Intense modes of molecule in region / cm^{-1}
NiTPP								2.3	
	1554		-3	6	0.13	0.13	0.14		
	1574		0	-2	0.22	0.22	0.22		
	1581		0	1	0.28	0.25	0.25		
	1598		0	0	1.00	1.00	1.00		
	1608		-3	-1	0.29	0.29	0.29		
ClAlPc								1.8	1520
	1550		3	-8	0.20	0.19	0.16		
	1574		-2	0	0.44	0.17	0.18		
	1582		-2	1	0.12	0.17	0.40		
	1598		1	0	1.00	1.00	1.00		
	1604		6	9	0.71	0.14	0.11		
NiPc								1.8	1545
	1542	1559	-3	3	0.17	0.15	0.17		
	1572		1	2	0.32	0.18	0.31		
	1581		0	1	0.13	0.18	0.17		
	1598		2	2	1.00	1.00	1.00		
	1611		3	1	0.21	0.14	0.24		

Table 6.3: 2.34 eV Excitation. Note: the intensities are relative to the intensity of the G^+ peak.

It can be seen from Figure 6.21 and Table 6.3 that there is no change in the position of the semiconducting G^+ mode upon modification of the SWNTs with NiTPP molecules. However, there is also evidence of a decrease in the intensity of the shoulder to the G^+ mode upon both filling and covering. The cluttered nature of the modes forming this shoulder make it difficult to be sure which modes are responsible to the observed changes, however the spectra imply that the reduction is greater for the filled nanotubes.

For SWNTs modified with ClAlPc molecules it can be seen that there is a small up-shift of 1 cm^{-1} in the postion of semiconducting G^+ mode when the SWNTs were filled with ClAlPc molecules. However, no change in the postion of this mode is observed when the SWNTs were covered. There are also changes in relative intensities of the G^- mode for both the SWNTs fillied and covered with molecules, with the filling causing a reduction in the intensity and the covering causing an enhancement. It is also worth noting that there is no evidence of a molecule peak in either spectrum.

For SWNTs modified with NiPc molecules it can be seen that there is a noticeable up-shift of 2 cm^{-1} in the postion of the semiconducting G^+ mode upon internal and external modification of the SWNTs with NiPc molecules.

There is also clear evidence of a peak at 1559 cm^{-1} which as before can be attributed to the NiPc molecule. This peak possesses both the same position and approximate intensity for both filled and covered SWNTs.

Spectra acquired using the 3.83 eV laser

The SWNT G band spectra acquired using the 3.83 eV laser are shown in Figure 6.22 - Table 6.4 summarises the changes observed in the modes of the G band upon modification of the SWNTs with the organo-metallic molecules of the study.

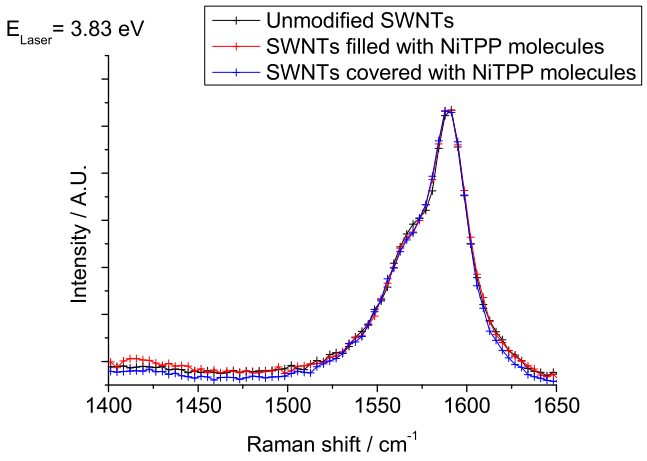

(a)

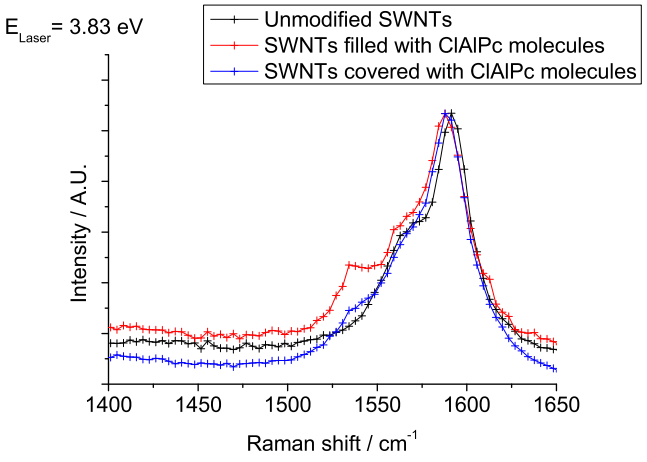

(b)

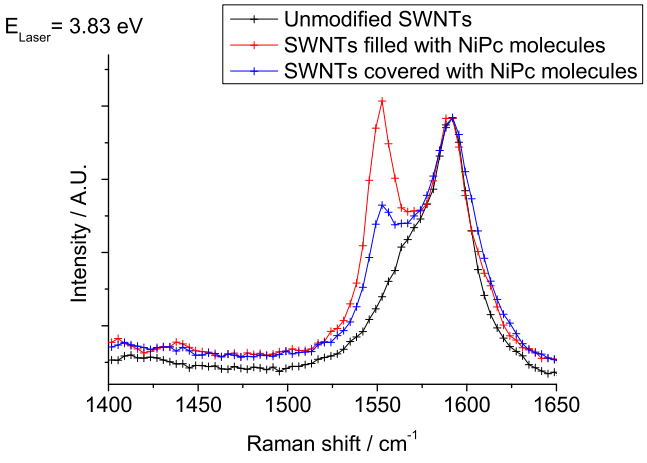

(c)

Figure 6.22: (a) to (f) show resonant Raman spectra of SWNTs filled and covered with NiTPP, ClAlPc and NiPc molecules respectively acquired using a 3.83 eV laser. The spectra of unmodifed SWNTs are shown in black as a reference.

SWNTs modified with:	SWNT mode frequency / cm-1	Additional modes / cm-1	Frequency shift (filled) /cm-1	Frequency shift (covered) / cm-1	Relative intensity (unmodified)	Relative intensity (filled)	Relative intensity (covered)	Optimum filling diameter / nm	Intense modes of molecule in region / cm-1
NiTPP								2.3	
	1548		-1	3	0.09	0.06	0.12		
	1563		2	2	0.27	0.34	0.32		
	1573		6	7	0.18	0.09	0.24		
	1590		0	1	1.00	1.00	1.00		
ClAlPc								1.8	1522
	1550	1534 (F)			0.10				
	1562	1538 (C)	-2	3	0.30	0.23	0.34		
	1573		-2		0.29	0.18			
	1591		-2	-1	1.00	1.00	1.00		
	1599				0.31				
NiPc		1552 (F)						1.8	
	1548	1553 (C)		-3	0.08		0.06		
	1560			4	0.11		0.15		
	1571		-2	4	0.43	0.24	0.25		
	1591		0	2	1.00	1.00	1.00		
	1602				0.15				

Table 6.4: 3.83 eV Excitation. Note: the intensities are relative to the intensity of the G^+ peak.

It can be seen from Figure 6.22 and Table 6.4 that no change in the position of the G^+ SWNT peak located at 1590 cm^{-1} occurs upon filling with NiTPP molecules, however a small up-shift of 1 cm^{-1} is observed for SWNTs covered with NiTPP molecules. There may be some change in the relative intensity of the shoulder to the G^+ mode located at $\approx$ 1580 cm^{-1}, but it is difficult to be sure of the origins.

For SWNTs modified with ClAlPc molecules it can be seen that the position of the G^+ semiconducting SWNT mode is down-shifted by -2 cm^{-1} and -1 cm^{-1} upon filling and covering with ClAlPc molecules respectively. The fitted peaks imply a decrease in the intensity of the shoulder to the G^+ peak for the covered SWNTs. However, the presence of the relatively intense molecule peak in the spectrum make it appear that the shoulder has been enhanced when is has not.

Both the filled and covered spectra show peaks which are not present in the unmodified SWNT spectra at 1534 and 1538 cm^{-1} respectively. The peaks are attributed to particularly intense vibrational mode originating from the ClAlPc molecule as before. The intensity of this peak is greatest in the spectrum of SWNTs filled with ClAlPc molecules.

The fitted peaks imply a decrease in the intensity of the shoulder to the G^+ peak for the filled SWNTs. However, the presence of the relatively intense molecule peak in the spectrum make it appear that the shoulder has been enhanced when is has not.

For SWNTs modified with NiPc molecules it can be seen that the G^+ semiconducting mode is seen to be up-shifted by 2 cm^{-1} upon covering with NiPc molecules, however no shift is observed for the SWNTs filled with NiPc molecules.

The molecule peaks in both the filled and covered spectra are very intense, in similarity with what was observed in the ClAlPc modified SWNTs the molecule peak is greater for SWNTs filled with NiPc molecules. There is also a small discrepancy in the positions of this peak, with it being located at 1553 cm^{-1} in the covered spectrum and slightly lower at 1552 cm^{-1} in the filled. This too is the same pattern as observed with the ClAlPc molecule.

The dominant nature of the molecule peak makes even assigning changes in the relative intensities of the shoulders to the G^+ mode difficult.

6.4.2 The SWNT RBM band

Spectra acquired using the 1.59 eV laser

The radial breathing mode spectra of the unmodified SWNTs acquired using the 1.59 eV laser show four intense and sharp peaks and the spectra are fitted well by six Lorentzian line shapes. In the low frequency region of the spectra, depending upon the individual spectrum, one or two broad peaks are required at approximately 110 cm^{-1} and 130 cm^{-1} - these fitted peaks can be assigned to low frequency SWNT RBMs. Using equation 6.10 to calculate the diameters of the SWNTs associated with these modes it can be calculated that they originate from SWNTs of 2.34 nm and 1.96 nm in diameter respectively. Such diameters would put these SWNTs close to the peak of the nanotube diameter distribution function, meaning that there should be a large number of these nanotubes. However, as previously mentioned the intensity of RBMs originating from $d > 2.0$ nm are very low. This is likely to be the cause of the very low intensity of these modes.

Given the breadth and relatively low intensity of these modes and the fact that it is not possible to clearly identify the peak positions from the spectra, it is reasonable to assign a low weighting to changes in their positions. However, changes in the intensities of these modes may still be useful.

The remaining RBM peaks located at approximately 160 cm^{-1}, 210 cm^{-1}, 234 cm^{-1} and 268 cm^{-1} correspond to nanotubes of 1.6 nm, 1.2 nm, 1.0 nm and 0.9 nm in diameter respectively. Using these calculated diameters in combination with the Kataura plot shown in Figure 6.10 it is possible to identify the electronic type of each of these SWNTs. From the Kataura plot it can be seen that the RBM located at 160 cm^{-1} originates from metallic SWNTs of $\approx$ 1.6 nm in diameter. The remaining RBM's originate from semiconducting SWNTs of $\approx$ 1.0 nm in diameter. All but the 234 cm^{-1} mode are relatively sharp and intense.

Therefore, it is reasonable to view changes in the postion and intensity of these modes with a high degree of confidence. It is changes in the postion and intensity of these three modes which will be used to inform upon molecule-induced changes to the SWNTs mechanical and electronic properties.

SWNTs modified with NiTPP molecules

It can be seen from Table 6.5 and from Figure 6.23 (a) and (b) that there is no shift in the position of three most intense RBMs upon filling with NiTPP molecules. However, there is an enhancement in the intensity in all of the RBMs including the low intensity 114 cm^{-1} mode. In addition to these increases in intensity, there is a change in peak dominance upon filling. In the unmodified SWNT spectra, the two most intense peaks located at 164 cm^{-1} and 269 cm^{-1} possess approximately equal intensities, however, upon filling with NiTPP molecules the 164 cm^{-1} peak becomes dominant.

SWNT modes / cm^{-1}	$\Delta\omega$ (Filling) / cm^{-1}	$\Delta\omega$ (Covering) / cm^{-1}
114	9	9
164	0	1
211	0	1
234	1	1
269	0	0

Table 6.5: Vibrational modes of SWNTs modified with NiTPP molecules acquired using a 1.59 eV laser.

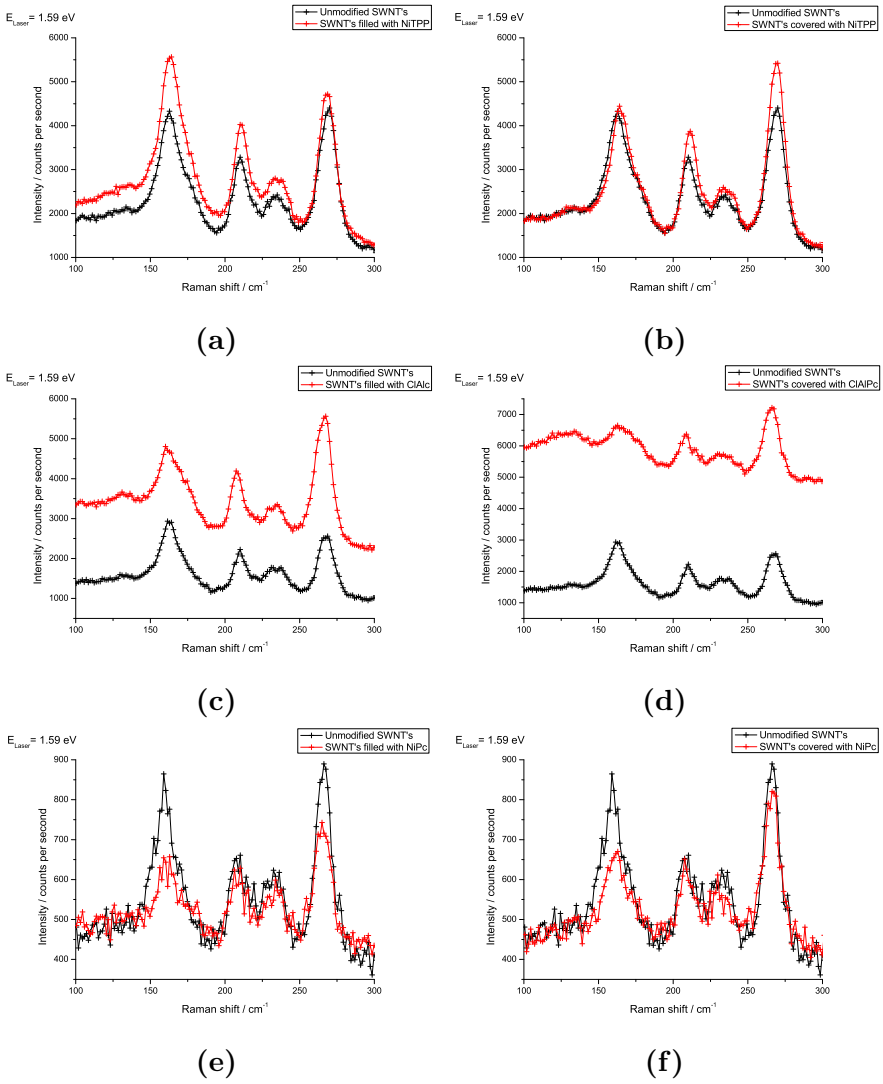

Figure 6.23: (a) to (f) show resonant Raman spectra of SWNTs filled and covered with NiTPP, ClAlPc and NiPc molecules respectively, acquired using a 1.59 eV laser. The spectra of unmodifed SWNTs are shown in black as a reference.

In contrast, a small up-shift of 1 cm^{-1} in the positions of the first two sharp peaks located at 164 cm^{-1} and 211 cm^{-1} was observed upon covering. No up-shift is observed in the 264 cm^{-1} peak. In similarity to what is observed in the NiTPP filled SWNT spectra, an increase in all of the sharp RBM's was observed when the SWNTs were covered with NiTPP molecules. However, in contrast the peak dominance is reversed. In the NiTPP covered SWNT spectra the 264 cm^{-1} peak is clearly dominant. In addition, no increase in the intensity of the 110 cm^{-1} mode is observed.

In conclusion, the RBM's of the SWNTs modified by both methods show enhancements in the intensities of the modes after modification with NiTPP molecules. However, the lower frequency modes originating from larger diameter nanotubes are dominant when the SWNTs are filled with NiTPP molecules, and the opposite is true for SWNTs covered with NiTPP molecules.

SWNTs modified with ClAlPc molecules

It can be seen from Table 6.6 and Figure 6.23 (c) and (d) that an up-shift of 1 cm^{-1} is seen in the position of the 163 cm^{-1} SWNT RBM mode when the SWNTs are filled with ClAlPc molecules. In addition to this, down-shifts of 2 cm^{-1} in the positions of the modes at 210 cm^{-1} and 268 cm^{-1} are observed. As well as these changes in peak position there are a number of changes in the intensity of the modes. The most striking changes in intensity originate from the reversal of the dominance in the spectra. In the un-modified spectrum the mode at 163 cm^{-1} is clearly dominant, however, upon filling, the mode at 268 cm^{-1} becomes dominant.

SWNT modes / cm^{-1}	$\Delta\omega$ (Filling) / cm^{-1}	$\Delta\omega$ (Covering) / cm^{-1}
104	-7	
131	1	
163	1	
210	-2	
234	1	
268	-2	

Table 6.6: Vibrational modes of SWNTs modified with ClAlPc molecules acquired using a 1.59 eV laser.

Due to the high gradient of the spectrum acquired from the SWNTs covered with ClAlPc molecules it was impossible to obtain a good fit to the data. However, it is still possible to make a number of observations from the relative intensities of the modes shown in the spectra. Firstly, there is an increase in the intensity of the broad RBM located at approximately 131 cm^{-1}. In addition to this there is a reversal in the dominance of the RBM's, with the 268 cm^{-1} mode becoming dominant after covering.

In conclusion, an up-shift of 1 cm^{-1} in the position of the 163 cm^{-1} RBM originating from metallic SWNTs is observed upon filling of the SWNTs with ClAlPc molecules. In contrast, the modes located at 210 cm^{-1} and 268 cm^{-1} originating from semiconducting SWNTs show down-shifts of 2 cm^{-1}. It can be seen that SWNTs modified with ClAlPc molecules using either method, show both an enhancement of the broad peak located at 131 cm^{-1} originating from semiconducting SWNTs of $\approx$ 2.0 nm in diameter and a shift in mode dominance with the 268 cm^{-1} RBM becoming the most intense mode upon modification.

SWNTs modified with NiPc molecules

The intensity of the spectra acquired from the NiPc samples is quite low; this makes peak fitting more difficult and hence reduces the confidence of the fitted peak positions of the RBM's. Therefore, a greater weighting is given to changes in the intensities of the RBM's of these spectra and the apparent changes in the positions of the fitted peaks will be ignored (table of peak positions not included).

The unmodified SWNT spectra shown in Figure 6.23 (e) and (f) show four relatively sharp peaks located at approximately 160 cm^{-1}, 208 cm^{-1}, 232 cm^{-1} and 266 cm^{-1}. The positions of these modes before and after modification coincide very well, this implies that there is little if any change in position. The most striking changes in the spectra upon modification of the SWNTs with NiPc molecules is the reduction in intensity of the RBMs located at 160 cm^{-1} and 266 cm^{-1}. The data imply a reduction in intensity because the intensities of the 208 cm^{-1} and 232 cm^{-1} modes remain constant upon modification, but the intensities of the other two modes decrease. The reduction in intensity of the 160 cm^{-1} mode seems to be approximately equal for both forms of modification, however the reduction in intensity of the 266 cm^{-1} mode seems to be greater for SWNTs filled with NiPc molecules as opposed to covered.

In conclusion, the most striking differences between the unmodified SWNT spectra and those modified with NiPc molecules come from decreases in the intensities of the RBM's located at 160 cm^{-1} and 266 cm^{-1} originating from metallic SWNTs of 1.9 nm in diameter and semiconducting SWNTs of 0.9 nm in diameter respectively. The decrease in the intensity of the 160 cm^{-1} mode is approximately the same for both forms of modification. In contrast, the intensity of the 266 cm^{-1} mode experiences the greater reduction in intensity when the SWNTs are filled with molecules.

Conclusions

In conclusion, it can be seen from the spectra that for SWNTs modified with the Pc type molecules the RBM located at approx. 268 cm^{-1} originating from semiconducting SWNTs of 0.9 nm in diameter is the dominant mode. This is in contradiction to what is observed in the spectra of the unmodified SWNTs where the unmodified spectra it is the 168 cm^{-1} mode originating from metallic SWNTs of $\approx$ 1.6 nm in diameter is dominant. In contrast to what is observed in SWNTs filled with Pc type molecules, the 168 cm^{-1} mode remained the dominant RBM of the SWNTs filled with NiTPP molecules. However, upon covering with NiTPP molecules the 268 cm^{-1} RBM becomes dominant in similarity to what is observed in the Pc modified SWNTs

Spectra acquired using the 2.34 eV laser

The RBM spectra acquired using the 2.34 eV laser can be fitted by at least four Lorentzian line-shapes. However, it can be seen from the Kataura plot that at this excitation energy the SWNT transition bands are much more tightly grouped. This makes identification of the individual RBM's more difficult. In general, the spectra are fitted well by the superposition of five Lorentzian line-shapes centred at 115 cm^{-1}, 153 cm^{-1}, 186 cm^{-1}, 234 cm^{-1} and 264 cm^{-1}.

Using equation 6.10 in combination with the Kataura plot it can be determined that the RBM located at $\approx$ 115 cm^{-1} can be attributed to either metallic or semiconducting SWNTs of 2.2 nm in diameter.

The broadness of the peak may be a reflection of the dense nature of the allowed transitions at this energy, or as mentioned previously, may be a result of the weak resonance of the RBM's of SWNTs with d > 2.0 nm. Given the breadth of this peak and that there is no clearly defined peak signature in the spectra, it is reasonable to put a low weighting to changes in the position of the peaks fitted to this mode, however, changes in the relative intensity of this mode may be meaningful.

The other modes are considerably sharper than the 115 cm^{-1} mode and hence the fitted peak positions are considerably more reliable. Using the Kataura plot, the modes located at 153 cm^{-1} and 186 cm^{-1} can be seen to originate from semiconducting SWNTs of 1.6 nm and 1.3 nm in diameter respectively. The modes located at 234 cm^{-1} and 264 cm^{-1} can attributed to metallic SWNTs of 1.0 nm and 0.9 nm in diameter respectively. The RBM located at 234 cm^{-1} is very broad and of low intensity, therefore changes in the position of this mode cannot be relied upon to be accurate.

In conclusion, the RBMs which are most reliable are those located at 163 cm^{-1} and 186 cm^{-1} originating from semiconducting SWNTs and the mode located at 268 cm^{-1} originating from metallic SWNTs. Changes in the positions and intensities of these modes will be utilized to identify changes in the mechanical and electrical properties of the SWNTs upon doping with molecules.

SWNTs modified with NiTPP molecules

It can be seen from Table 6.7 and Figure 6.24 (a) and (b) that the spectrum of the unmodified SWNTs and those modified with NiTPP molecules are very similar, however, there are a number of significant differences.

SWNT modes / cm^{-1}	$\Delta\omega$ (Filling) / cm^{-1}	$\Delta\omega$ (Covering) / cm^{-1}
116	-2	-2
152	7	6
183	6	7
265	8	6

Table 6.7: Vibrational modes of SWNTs modified with NiTPP molecules acquired using a 2.34 eV laser.

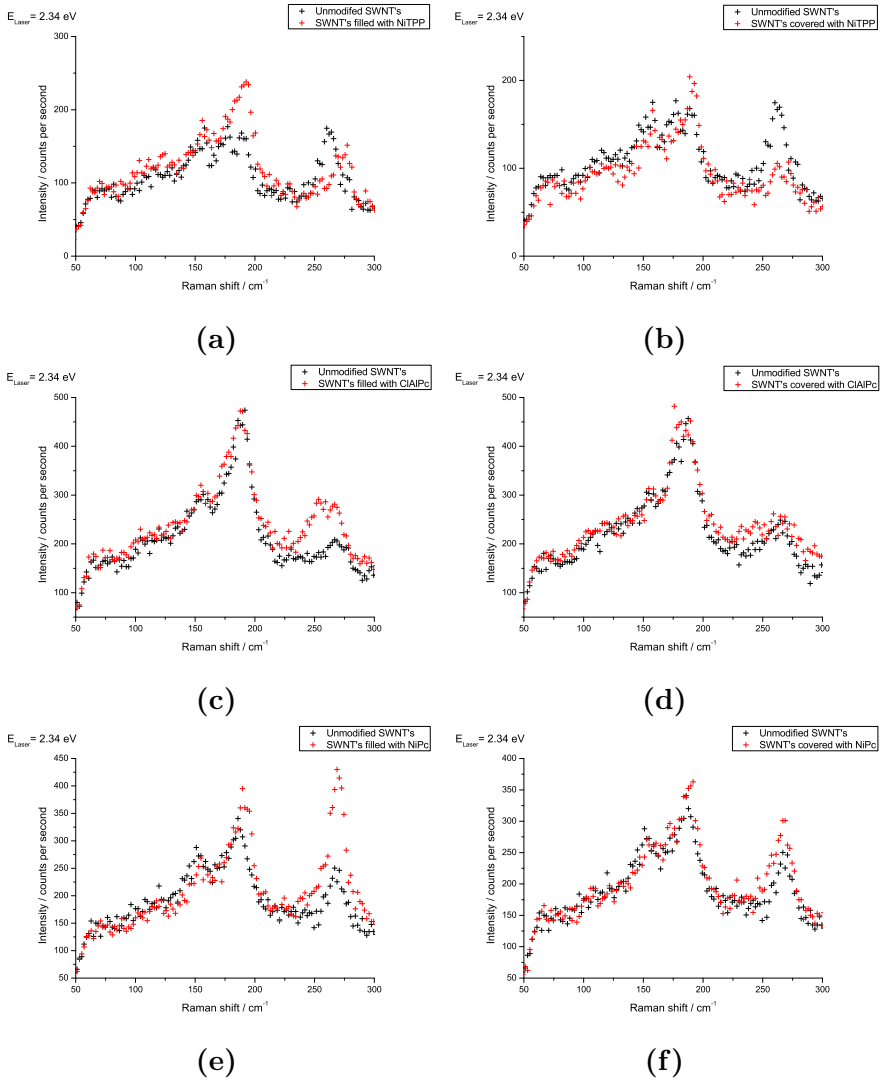

Figure 6.24: (a) to (f) show resonant Raman spectra of SWNTs filled and covered with NiTPP, ClAlPc and NiPc molecules respectively, acquired using a 2.34 eV laser. The spectra of unmodified SWNTs are shown in black as a reference.

Upon filling with NiTPP molecules the 186 cm^{-1} SWNT RBM shows a significant increase in intensity and becomes the dominant mode of the spectrum. In contrast, the RBM located at 265 cm^{-1} shows a slight decrease in intensity and is up-shifted by 8 cm^{-1} to 273 cm^{-1}.

Upon covering with NiTPP molecules a small increase in the intensity of the 186 cm^{-1} RBM, as well as a significant decrease in the intensity of the mode located at 265 cm^{-1} is observed - there is also evidence of an up-shift in the position of this mode.

In conclusion, the 186 cm^{-1} and 265 cm^{-1} SWNT RBM's both show noticeable changes after the SWNTs were modified with NiTPP molecules. The intensity of the 186 cm^{-1} mode is seen to be enhanced upon both filling and covering, however the enhancement is significantly greater for the SWNTs filled with NiTPP molecules rather than covered. A reduction in intensity of the 265 cm^{-1} mode and an up-shift in its position is observed for both forms of modification, however the up-shift is far greater for filling and the reduction in intensity is greater for covering.

SWNTs modified with ClAlPc molecules

It can be seen from the spectra shown in Figure 6.24 (c) and (d) and Table 6.8 that there is little or no significant change in either the intensity or position of the 153 cm^{-1} or 189 cm^{-1} RBM's upon either filling or covering of the SWNTs with ClAlPc molecules. There is also little or no significant change in the position or intensity of the 264 cm^{-1} mode upon covering of the SWNTs. However, the peak at 264 cm^{-1} in the ClAlPc filled SWNT spectrum is seen to be down-shifted by approximately 6 cm^{-1} and to be enhanced in intensity by a significant amount.

SWNT modes / cm^{-1}	$\Delta\omega$ (Filling) / cm^{-1}	$\Delta\omega$ (Covering) / cm^{-1}
119	-3	-10
153	2	-3
189	-1	-6
234		7
264	-6	3

Table 6.8: Vibrational modes of SWNTs modified with ClAlPc molecules acquired using a 2.34 eV laser.

SWNTs modified with NiPc molecules

It can be seen from the spectra shown in Figure 6.24 (e) and (f) and Table 6.9 that there is evidence of a small increase in the intensity of the 186 cm^{-1} mode in the spectra of SWNTs both filled and covered with NiPc molecules. In addition to this, there is evidence of up-shifts in the positions of the 153 cm^{-1} and 186 cm^{-1} modes upon filling. There is also evidence of an enhancement in the intensity of the 268 cm^{-1} mode upon both filling and covering. However, this enhancement is significantly greater in the NiPc-covered SWNT spectra.

SWNT modes / cm^{-1}	$\Delta\omega$ (Filling) / cm^{-1}	$\Delta\omega$ (Covering) / cm^{-1}
112		-5
153	5	5
186	4	2
235		18
268	1	0

Table 6.9: Vibrational modes of SWNTs modified with NiPc molecules acquired using a 2.34 eV laser.

Conclusions

In conclusion, it can be seen from the spectra that the intensity of the RBM located at $\approx$ 153 cm^{-1} is enhanced when the SWNTs are both filled and covered using NiTPP and NiPc molecules. This enhancement is greatest for SWNTs which have been filled with the molecules in both cases, however the SWNTs filled with NiTPP molecules show the greatest enhancement.

The SWNTs modified with ClAlPc molecules show no change in the position or intensity of this mode.

The intensity of the SWNT RBM located at ≈ 265 cm^{-1} shows either a small increase or no change in intensity when covered with NiPc and ClAlPc molecules respectively. In contrast, the RBM of SWNTs covered with NiTPP molecules shows a decrease in the intensity of the 265 cm^{-1} mode.

Spectra acquired using the 3.83 eV laser

It was not possible to acquire any useful RBM spectra from the nanotube samples using the 3.83 eV laser. This was due to intrinsic limitations of the spectrometer used.

6.5 Discussion

The Raman spectra described above revealed the following:

(i) Shifts in the positions of the G^- and G^+ SWNT modes and in the position of the molecule modes.

(ii) The shifts in position are larger for certain molecules.

(iii) Changes in the relative intensity of the G^- mode.

(iv) For a given molecule and type of SWNT modification employed, different spectral changes were observed depending on which laser was used.

A summary of the main results is given in Table 2.11.

E_{Laser}	Molecule	Δ G^+ / cm-1 (Filled)	Δ G^+ / cm-1 (Covered)	d_{tsc} / nm	d_{tscG} / nm	$d_{optimum}$ / nm
1.59 eV				2.2	2.5	
	NiTPP	1	0			2.3
	ClAlPc	-2	-4			1.8
	NiPc	-1	0			1.8
2.34 eV				1.8	2.0	
	NiTPP	0	0			2.3
	ClAlPc	1	0			1.8
	NiPc	2	2			1.8
3.83 eV				-	-	
	NiTPP	0	1			2.3
	ClAlPc	-2	-1			1.8
	NiPc	0	2			1.8

Table 6.10: shows the shifts in the position of the G^+ modes of spectra acquired from SWNTs both filled and covered with each molecule acquired with each laser. E_{Laser} is the energy of the lasers used, Δ G^+ is the Raman shift in the position of the G^+ mode observed upon filling and covering. d_{tsc} indicates the diameter of the semiconducting nanotubes in resonance with each laser. d_{tscG} indicates the diameter of the semiconducting nanotubes in resonance with photon scattered by the nanotube G mode. $d_{optimum}$ is the optimum filling diameter for each molecule.

Such effects can be caused by a number of phenomena. The most likely to cause such changes are (i) strain induced in the nanotubes as a result of charge transfer between nanotube and molecule and (ii) structural strain induced in the nanotubes by the filling and covering.

6.5.1 (i) Charge transfer

As discussed in section 6.2.5, charge transfer to or from dopant molecules to nanotubes is known to result in strain being induced in the nanotube structure either due to a weakening of the C-C bonds (n-type doping) or a strengthening of the bonds (p-type doping).

Charge transfer to nanotubes can occur in one of two ways, either electrons will be transferred from occupied states in the dopants to unoccupied states in the conduction band of the nanotube (n-type doping) or electrons will be donated from the nanotube valence band to unoccupied states in the dopant (p-type doping). It has been demonstrated that charge transfer between the SWNTs and organic molecules is controlled by the ionisation potential (IP) and / or the electron affinity (EA) of the guest molecule [114]. The ionisation potential of a molecule can be thought of as the minimum energy required to remove an electron. If the molecule in question was in the ground state the ionisation potential would be the difference in energy between the highest occupied molecular orbital (HOMO) and the vacuum level. In contrast, the electron affinity is the energy released when an electron attaches to a molecule. In the ground state, this would be the energy difference between the vacuum level and lowest unoccupied molecular orbital (LUMO).

When the HOMO of the dopant molecule is greater in energy than the conduction band of the nanotube as is the case in Figure 6.25 (a) then electrons are donated from the molecule to the nanotube, and the nanotube becomes n-type doped. If however, the valence band of the nanotube is higher than the LUMO of the molecule (Figure 6.25 (b)) then electrons will be transferred from the nanotube to the molecule and the nanotube will become p-type doped.

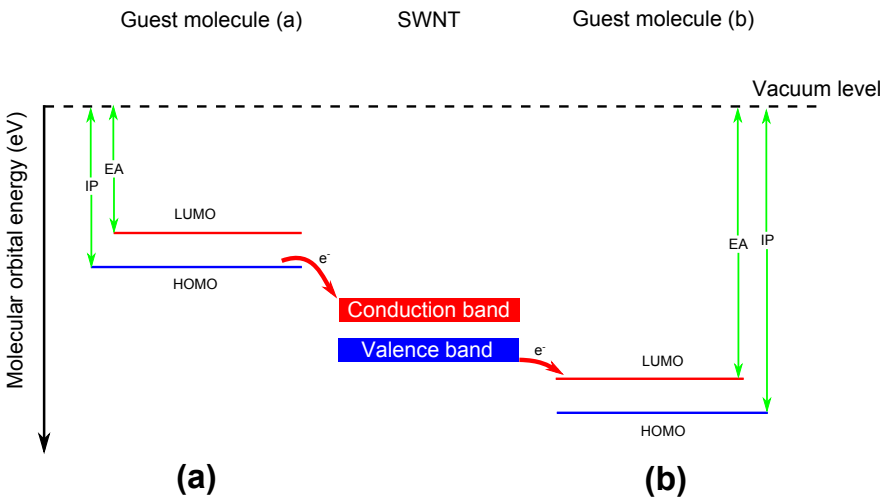

Figure 6.25: The possible charge transfer mechanisms between SWNTs and guest molecules. (a) charge transfer from molecule to nanotube (b) charge transfer from nanotube to molecule.

The charge transfer direction will depend very much upon the electronic structure of the guest organic molecule. For example when the organic chain molecule SPEEK which contains aromatic rings was added to the exterior of semiconducting SWNTs of 1.48 nm by Zhu *et. al.* [115] charge transfer from the valence bands of the SWNT to the LUMO of the SPEEK molecule was observed. Charge transfer is confirmed by a noticeable up-shift in the SWNT G band upon modification of the SWNTs with the SPEEK molecule.

In contrast, when SWNTs were functionalized with smaller aromatic molecules such as Amph-TTF and TDD-TTF [98] and aromatic amines [96] down-shifts in the positions of the SWNT G bands consistent with charge transfer from the guest molecules to the SWNTs were observed.

Figure 6.26 shows the molecular orbitals (MOs) of the three molecules used in this study. The HOMO and LUMO levels of the ClAlPc molecule were determined experimentally [116], while those of the NiPc and porphyrin molecules were calculated using density functional theory (DFT) [117, 118]. The band gaps and MOs of the phthalocyanine molecules are roughly the same. The NiTPP molecule however, has both a larger band gap and a higher LUMO than the other molecules.

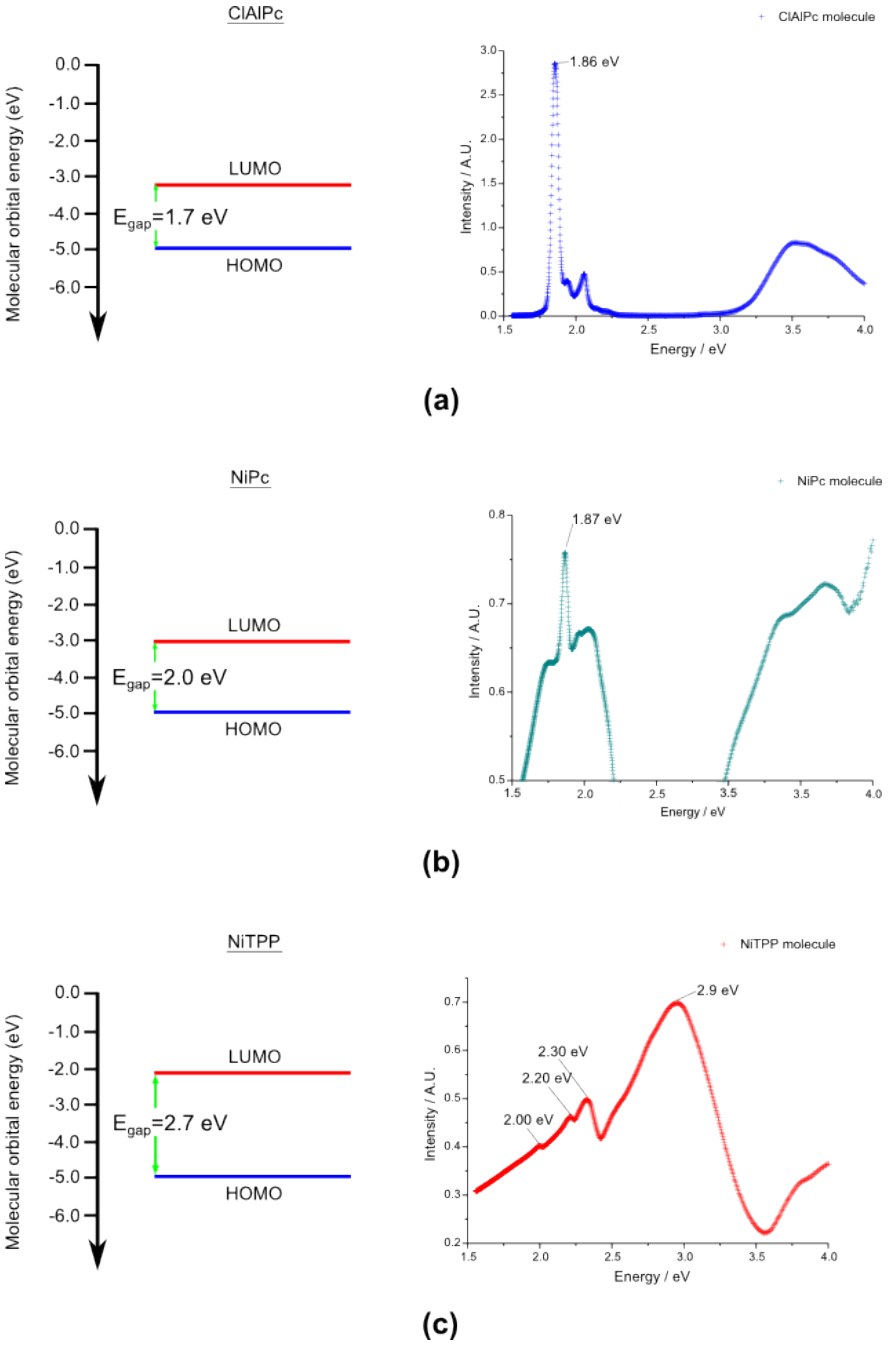

Figure 6.26: The HOMO and LUMO energy levels [116–118] and optical absorption spectra of the molecules used in this study ((a) ClAlPc, (b) NiPc and (c) NiTPP).

Optical absorption spectra acquired from the molecules have been included to gauge the validity of the values obtained from literature.

Making a comparison between the two, it can be seen that the values agree within ≈0.2 eV each other.

The other factor which determines whether charge transfer will occur is the relative positions and occupancies of the valence and conduction bands of the SWNTs upon which the guest molecules are attached. It has been found that the Fermi level of nanotubes of greater than 1 nm in diameter is approximated well by the work function of graphene (-4.66 eV) [119]. It has also been found that semiconducting SWNTs are p-doped in ambient conditions [120]; this means that the top of the valence band of semiconducting SWNTs is partially vacant and ready to receive electrons from the HOMO of a suitable molecule.

Another important aspect to consider is the quantum mechanical nature of nanotubes - specifically the relationship between the band gap of the nanotube and its diameter. In nanotubes the band gap is inversely proportional to diameter. The band gap will determine the positions of the valence and conduction bands of the nanotube. The band gaps between the V_1 and C_1 van Hove singularities of semiconducting nanotubes (i.e. the $E_{11}{}^{s}$ transition), calculated using the allowed transitions shown in the Kataura plot, of diameters in the range 1.0 to 2.5 nm (encompassing the likely diameter distribution used in this study) are given in Table 6.11.

Nanotube diameter / nm	Band gap / eV
1.0	0.80
1.5	0.55
2.0	0.40
2.5	0.35

Table 6.11: The diameters and associated band gaps of semiconducting SWNTs.

Figure 6.27 shows the likely charge transfer mechanism between the ClAlPc molecule and semiconducting nanotubes possessing diameters expected to present in the samples.

It can be seen from this figure that, on making the assumption that the obtained values for the molecular orbitals of the ClAlPc molecule and band structure of the p-doped SWNTs are true, then charge transfer from the HOMO of the molecules to the vacant states in the valence band of the nanotubes will be possible. However, the amount of charge transferred will be reduced as the band gap decreases with increasing nanotube diameter. Given that the band gap of the ClAlPc and NiPc molecules is very similar, this mechanism, if accurate, is likely true for both.

Another factor which may have an effect upon the charge transfer between the molecules and the nanotubes is the extent to which the molecules are distorted due interaction with the nanotube. It has been found using density functional theory calculations that when distorted out of planarity the HOMO level of the NiTPP molecule increases and the LUMO decreases with the amount of distortion [121]. As discussed in chapter 3, the molecules attached to nanotubes are likely to have some level of curvature induced distortion, the extent of which will depend upon the diameter of the nanotube to which they are attached. Such distortions to the molecules both encapsulated and attached to the exterior of SWNTs could have an effect upon the charge transfer between the molecules and SWNTs. For example, a distortion-induced increase in the height of the HOMO of an attached molecule could result in charge transfer which would be unfavorable in the planar molecule.

However, the calculations of Maji et al. [121] show that the increases in the energy of the HOMO are expected to be small (less than 0.1 eV) and therefore probably would not greatly affect the charge transfer between the molecules and the nanotubes.

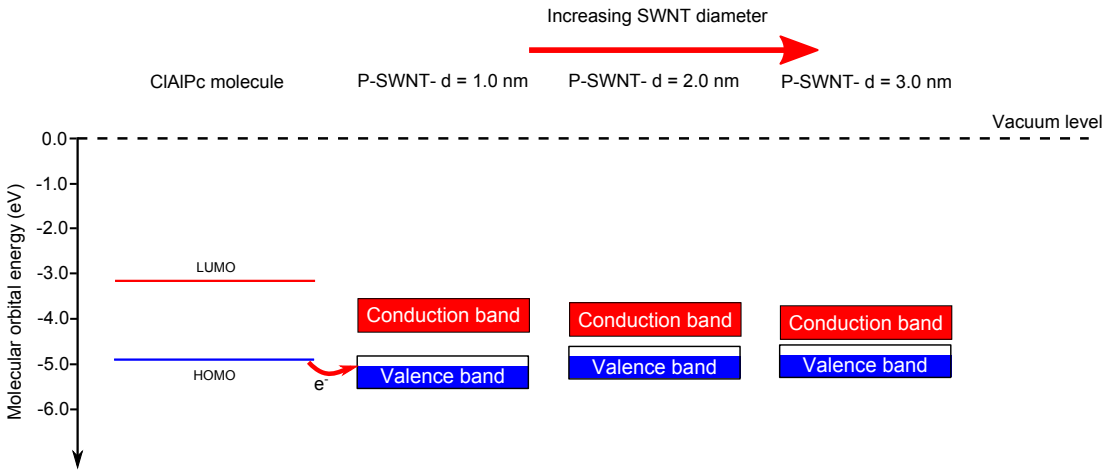

Figure 6.27: Schematic illustration of electron transfer between the ClAlPc molecule and intrinsically p-doped SWNTs of various diameters.

This mechanism would fit well with the observed down-shifts in the G^- and G^+ peaks observed when SWNTs modified with both ClAlPc and NiPc molecules were excited by a 1.59 eV laser. At this excitation energy semiconducting nanotubes of 2.0 nm in diameter are in resonance. This is close to the optimum filling diameter of 1.8 nm, therefore molecule-nanotube interaction should be maximised. The up-shift in the G^- and G^+ peaks observed when the ClAlPc modified SWNTs were excited by a 2.34 eV laser and when the NiPc modified SWNTs were excited by both the 2.34 eV and 3.83 eV lasers are inconsistent with the above charge transfer mechanism. This may result from different nanotube diameters being in resonance at these energies.

The NiTPP molecule is different both structurally and electronically and is larger than the Phthalocyanine molecules. It possesses a larger HOMO-LUMO gap of 2.9 eV meaning that its LUMO is likely to be even higher in energy that that of the Pc molecules. The HOMO is expected to be at approximately the same level as for the Pc molecules. In terms of charge transfer this would imply that using the mechanism above, electron transfer from the molecule to the nanotube should be favourable. However, the up-shifts observed in the Raman spectra of SWNTs modified with NiTPP excited with the 1.59 and 3.83 eV lasers would imply charge transfer from the nanotubes to the molecule. This would be inconsistent with the above charge transfer mechanism.

The molecular orbitals of the TPP molecule shown schematically in Figure 6.26 were obtained by density functional theory (DFT) calculations [118] and while this method is known to give good indications of molecular HOMO-LUMO gaps, it is less accurate in giving the exact position of the energy levels. This is for the TPP molecule and not the NiTPP molecule but, the HOMO and LUMOs of the two molecules should belong to the π and π^* orbitals and hence be the same. If charge transfer is responsible for the observed down-shifts then the electron affinity of the NiTPP molecule would have to be a lot larger - such a scenario in shown in Figure 6.28. In this scenario only the band structure of larger diameter SWNTs have been included. This is because the molecules are not expected to fit into the narrower tubes.

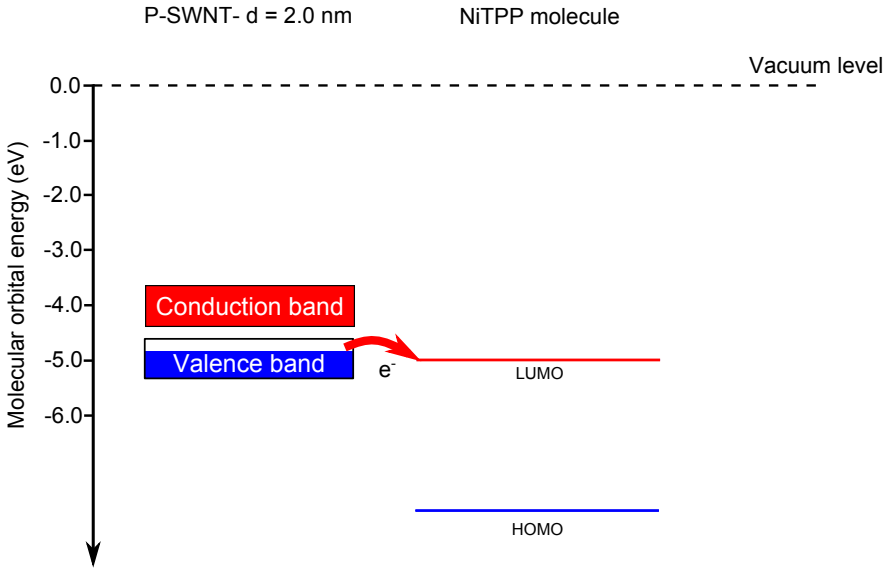

Figure 6.28: Schematic illustration of a possible scenario for charge transfer from a 2.0 nm semiconducting SWNT to the NiTPP molecule.

While the charge transfer mechanism described above could explain the down-shifts observed in some of the G^+ modes in spectra of the SWNTs filled and covered with the phthalocyanine molecules provided that their HOMOs are high enough, it is inconsistent with the up-shifts in the G^+ modes observed in others such as any of the spectra of SWNTs functionalized with NiTPP molecules.

6.5.2 (ii) Structural strain

The other way in which the nanotubes can be strained is by structural deformation of the nanotube walls, for instance by the introduction of foreign material into the internal cavity of the nanotube or by attachment of material to the exterior. Such a mechanism has been employed previously [122] to explain up-shifts observed in the G^+ modes of SWNTs doped with rubidium atoms. It is likely that the greatest level of structural deformation-based strain in filled nanotubes would result from tubes where the diameter of the nanotube filled is less than the optimum filling diameter of the encapsulated molecule [102].

The above argument could explain the up-shifts observed in some of the G^+ modes of SWNTs modified with molecular systems in this study, summarised in Table 6.10.

The semiconducting SWNTs in resonance with the 1.59 eV laser and with the G scattered photon have a diameters of 2.2 nm and 2.5 nm respectively. These diameters match well with the expected optimum filling diameter for the NiTPP molecule of 2.3 nm. It is possible that close to $d_{optimum}$ the filling causes structural strain to the nanotube. If so, the above mechanism would explain the observed up-shift in the G mode.

The semiconducting nanotubes in resonance with the 2.34 eV laser and with the G scattered photon have a diameters of 1.8 nm and 2.0 nm respectively. These tubes are too narrow for the NiTPP molecules to enter face-on, therefore, it is likely that the resulting filling yield is either a very low (undetectable), this would be consistent with the lack of any peak shift in the G^+ mode.

The diameters of the nanotubes in resonance with the 2.34 eV laser are very close to the optimum diameter for face-on filling of the NiPc molecules as discussed previously for the NiTPP molecules filling the nanotubes probed with the 1.59 eV laser, the up-shift in the G^+ modes of the Pc-filled nanotubes could be a result of filling-induced structural strain.

While individually the mechanisms do not entirely explain the observed shifts in the G^+ modes, a combination of the two mechanisms might serve to explain the majority of the shifts. Not all of the shifts can be accounted for by these two methods, for example the case of the up-shift observed in the G band of the SWNTs covered with NiPc molecules acquired with the 3.83 eV laser where no up-shift is observed in the filled sample. It is possible that this is due to some unknown effect - further study is needed to fully explain such changes.

Chapter 7

Conclusions and future work

7.1 Conclusions

Endohedral functionalization via supercritical CO_2 was undertaken in order to produce encapsulation of compounds that are difficult to encapsulate otherwise due to either their larger size or extreme air sensitivity. For this, two experimental supercritical CO_2 set-ups were developed, one for standard, stable encapsulants, and the other to enable the anaerobic encapsulation of air-sensitive systems. Though equipment related technical difficulties prevented the demonstration of encapsulation of air sensitive molecules (which would have been the first of its kind were it to have been achieved) encapsulation of planar molecules of large size ($\approx$ 2 nm) has been achieved. These latter systems are not suitable for thermally induced, diffusion-based encapsulation due to their large size. Confinement in nanotubes of optimum diameter promoted ordering of NiTPP molecules in row-like, self-assembled structures; while disordered molecular arrangement dominated in larger diameter systems. High yield of molecular filling was also obtained for diameters larger than an optimum value (of about 2.3 nm), though filling within diameters less than optimum was also produced at low yield, and involved strong structural strain to the molecule body.

The comparative endo- and exohedral systems (NiPc, ClAlPc and NiTPP) were chosen so as to induce different degrees of electronic changes in the nanotube hosts, which were found to be mostly consistent with a combination of charge transfer (controlled by the alignment of the molecular HOMO-LUMO band gap to the energy spectrum of carbon nanotubes) and structural strain. These changes affect both the RBM and G modes of carbon nanotubes. NiTPP, ClAlPc and NiPc molecules provided a set of systems differing by only one specific parameter (e.g. central ion or body type, or size of the HOMO-LUMO gap). Though the large NiTPP molecules and large diameter Nanocyl SWNTs are perfectly matched in terms of geometry, the decrease in size of the nanotubes' electronic band gap that occurs in wide Nanocyl nanotubes puts a limit on what can be achieved in terms of doping. Finally, exohedral functionalization showed some degree of perturbation of the electonic structure of the nanotubes demonstrating that the molecules did attach to the outer surface of the nanotube despite perturbation by the central metal ion of their aromatic system (which is supposed to promote π stacking).

7.2 Future work

Future work could focus on the following directions:

(i) Comparative Raman/ IR studies where Raman mainly probes the nanotube sub-system, IR spectroscopy would probe the molecular sub-system.

(ii) ClAlPc molecules possess an electronic dipole, this might effect what ordering could be obtained inside of carbon nanotube templates, hence parallel HRTEM studies could reveal differences compared to their nickel-based counterparts.

If encapsulated in an ordered form inside of a SWNT, the ClAlPc molecules with their electronic dipole core could induce a modulated periodic potential within the nanotube (see Figure 7.1). This could result in negative differential resistance in electronic transport or scanning tunnelling spectroscopy.

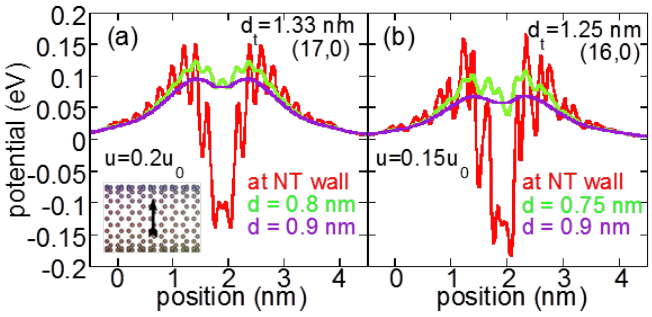

Figure 7.1: Electrostatic potential calculated along nanotube for a permanent dipole perpendicular to the nanotube's axis [123].

(iii) Another spectroscopic technique which could be employed is tip-enhanced Raman spectroscopy (TERS). In a typical TERS experiment, a laser is focused on the end of an AFM cantilever coated with gold - the tip of the cantilever acts as a nanostructure to produce Raman signal enhancement on a sample surface once the tip has been brought close enough. The resolution of this process is $\approx$ 20 nm [124], allowing Raman spectra to be acquired from very small areas [124, 125], hence the local effect of individual or a small number of encapsulates could be probed. TERS has been used successfully to acquire Raman spectra from carbon nanotubes [124, 125]. Use of this technique on the nanotube hybrids of this study, if sufficiently dispersed, would allow for the nanotubes to be probed in their un-bundled state and would allow for spectra to be acquired from individual semiconducting and metallic SWNTs. This would make assessing shifts in the peak positions of the G- modes much easier.

(iv) Finally, the hybrids produced in this work should possess paramagnetism. By studying their magnetic properties, new physics may be discovered.

Bibliography

[1] S. Iijima et al. Helical microtubules of graphitic carbon. *nature*, 354(6348):56–58, 1991.

[2] A. K. Geim and K. S. Novoselov. The rise of graphene. *Nature materials*, 6(3):183–191, 2007.

[3] M. S. Dresselhaus R. Saito, G. Dresselhaus. *Physical Properties of Carbon Nanotubes*. Imperial College Press, 2007.

[4] D. Tasis, N. Tagmatarchis, A. Bianco, and M. Prato. Chemistry of carbon nanotubes. *Chemical Reviews*, 106(3):1105–1136, 2006.

[5] D. A. Britz and A. N. Khlobystov. Noncovalent interactions of molecules with single walled carbon nanotubes. *Chem. Soc. Rev.*, 35:637–659, 2006.

[6] R. R. Meyer, J. Sloan, R. E. Dunin-Borkowski, A. I. Kirkland, M. C. Novotny, S. R. Bailey, J. L. Hutchison, and M. L. H. Green. Discrete atom imaging of one-dimensional crystals formed within single-walled carbon nanotubes. *Science*, 289(5483):1324–1326, 2000.

[7] D. A. Britz, A. N. Khlobystov, J. Wang, A. S. O'Neil, M. Poliakoff, A. Ardavan, and G. A. D. Briggs. Selective host–guest interaction of single-walled carbon nanotubes with functionalised fullerenes. *Chemical communications*, (2):176–177, 2004.

[8] A. Ilie, J. S. Bendall, K. Nagaoka, S. Egger, T. Nakayama, and S. Crampin. Encapsulated inorganic nanostructures: A route to sizable modulated, noncovalent, on-tube potentials in carbon nanotubes. *ACS nano*, 5(4):2559–2569, 2011.

[9] M. Monthioux, E. Flahaut, and J. P. Cleuziou. Hybrid carbon nanotubes: Strategy, progress, and perspectives. *Journal of materials research*, 21(11):2774–2793, 2006.

[10] W. Zhiyong, S. Zujin, and G. Zhennan. New phenomena of materials confined in nano space. *PROGRESS IN CHEMISTRY*, 21(11):2435–2444, 2009.

[11] P. M. F. J. Costa, D. Golberg, M. Mitome, S. Hampel, A. Leonhardt, B. Buchner, and Y. Bando. Stepwise current-driven release of attogram quantities of copper iodide encapsulated in carbon nanotubes. *Nano letters*, 8(10):3120–3125, 2008.

[12] S. Brahim, S. Colbern, R. Gump, and L. Grigorian. Tailoring gas sensing properties of carbon nanotubes. *Journal of Applied Physics*, 104(2):024502–024502, 2008.

[13] J. H. Warner, A. A. R. Watt, L. Ge, K. Porfyrakis, T. Akachi, H. Okimoto, Y. Ito, A. Ardavan, B. Montanari, J. H. Jefferson, et al. Dynamics of paramagnetic metallofullerenes in carbon nanotube peapods. *Nano letters*, 8(4):1005–1010, 2008.

[14] S. Y. Hong, G. Tobias, K. T. Al-Jamal, B. Ballesteros, H. Ali-Boucetta, S. Lozano-Perez, P. D. Nellist, R. B. Sim, C. Finucane, S. J. Mather, et al. Filled and glycosylated carbon nanotubes for in vivo radioemitter localization and imaging. *Nature materials*, 9(6):485–490, 2010.

[15] A. N. Khlobystov, D. A. Britz, O'neil S. A. Martyn P. Wang, J., and G.A.D. Briggs. Low temperature assembly of fullerene arrays in single-walled carbon nanotubes using supercritical fluids. *Journal of Materials Chemistry*, 14(19):2852–2857, 2004.

[16] L. Li, A. N. Khlobystov, J. G. Wiltshire, G. A. D. Briggs, and R. J. Nicholas. Diameter-selective encapsulation of metallocenes in single-walled carbon nanotubes. *Nature materials*, 4(6):481–485, 2005.

[17] P. Peumans and S. R. Forrest. Very-high-efficiency double-heterostructure copper phthalocyanine/c-60 photovoltaic cells. *Applied Physics Letters*, 79(1):126–128, 2001.

[18] Y. Qiu, Y. Gao, P. Wei, and L. Wang. Organic light-emitting diodes with improved hole-electron balance by using copper phthalocyanine/aromatic diamine multiple quantum wells. *Applied physics letters*, 80(15):2628–2630, 2002.

[19] D. R. Kauffman, O. Kuzmych, and A. Star. Interactions between single-walled carbon nanotubes and tetraphenyl metalloporphyrins: Correlation between spectroscopic and fet measurements. *The Journal of Physical Chemistry C*, 111(9):3539–3543, 2007.

[20] J. De Paula P. Atkins. *Physical Chemistry*. Oxford University Press, 2006.

[21] A. Ilie. Nanoscience lecture notes.

[22] N. D. Mermin N. W. Ashcroft. *Solid State Physics*. Brooks/Cole, 1976.

[23] J. Maultzsch S. Reich, C. Thomsen. *Carbon Nanotubes Basic Concepts and Physical Properties*. Wiley-VCH, 2004.

[24] A. L. Kalamkarov, A.V. Georgiades, S.K. Rokkam, VP Veedu, and M.N. Ghasemi-Nejhad. Analytical and numerical techniques to predict carbon nanotubes properties. *International Journal of Solids and Structures*, 43(22):6832–6854, 2006.

[25] Nanodic.com, 2008-2011. armchair nanotube [online]. available from: http://www.nanodic.com/picturepreview.php?ch=carbon&term=armchair nanotube&g=4.[accessed november 2013].

[26] J.W. Mintmire and C.T. White. Universal density of states for carbon nanotubes. *Physical Review Letters*, 81(12):2506, 1998.

[27] M.S. Dresselhaus, G. Dresselhaus, and A. Jorio. Unusual properties and structure of carbon nanotubes. *Annu. Rev. Mater. Res.*, 34:247–278, 2004.

[28] M. S. Dresselhaus, G. Dresselhaus, R. Saito, and A. Jorio. Raman spectroscopy of carbon nanotubes. *Physics Reports*, 409(2):47–99, 2005.

[29] S. Niyogi, M. A. Hamon, H. Hu, B. Zhao, P. Bhowmik, R. Sen, M. E. Itkis, and R. C. Haddon. Chemistry of single-walled carbon nanotubes. *Accounts of Chemical Research*, 35(12):1105–1113, 2002.

[30] Z. Chen, W. Thiel, and A. Hirsch. Reactivity of the convex and concave surfaces of single-walled carbon nanotubes (swcnts) towards addition reactions: Dependence on the carbon-atom pyramidalization. *ChemPhysChem*, 4(1):93–97, 2003.

[31] L.A. Girifalco, M. Hodak, and R. S. Lee. Carbon nanotubes, buckyballs, ropes, and a universal graphitic potential. *Physical Review B*, 62(19):13104, 2000.

[32] L.A. Girifalco and M. Hodak. Van der waals binding energies in graphitic structures. *Physical Review B*, 65(12):125404, 2002.

[33] G. Stan, M. J. Bojan, S. Curtarolo, S. M. Gatica, and M. W. Cole. Uptake of gases in bundles of carbon nanotubes. *Physical Review B*, 62(3):2173, 2000.

[34] J. Wang, M. K. Kuimova, M. Poliakoff, G. A. D. Briggs, and Andrei N Khlobystov. Encapsulation and ir probing of cube-shaped octasilasesquioxane h8si8o12 in carbon nanotubes. *Angewandte Chemie International Edition*, 45(31):5188–5191, 2006.

[35] K. Muthukumar, H. O. Jeschke, R. Valentí, E. Begun, J. Schwenk, F. Porrati, and M. Huth. Spontaneous dissociation of co2 (co) 8 and autocatalytic growth of co on sio2: A combined experimental and theoretical investigation. *Beilstein Journal of Nanotechnology*, 3(1):546–555, 2012.

[36] K. Schulte, C. Yan, M. Ahola-Tuomi, A . Stróżecka, P.J. Moriarty, and A.N. Khlobystov. Encapsulation of cobalt phthalocyanine molecules in carbon nanotubes. In *Journal of Physics: Conference Series*, volume 100, page 012017, 2008.

[37] Computer model of the nitpp molecule produced by dr. adelina ilie using the software crystalmaker.

[38] Computer model of the nitpp molecule inside a (25,0) swcnt of 2nm diameter produced by dr. adelina ilie using the software crystalmaker.

[39] H. Li, B. Zhou, Y. Lin, L. Gu, W. Wang, K.A. Shiral Fernando, S. Kumar, L. F. Allard, and Y. Sun. Selective interactions of porphyrins with semiconducting single-walled carbon nanotubes. *Journal of the American Chemical Society*, 126(4):1014–1015, 2004.

[40] X. Wang, Y. Liu, W. Qiu, and D. Zhu. Immobilization of tetra-tert-butylphthalocyanines on carbon nanotubes: a first step towards the development of new nanomaterials. *Journal of Materials Chemistry*, 12(6):1636–1639, 2002.

[41] F. Tournus, S. Latil, M. I. Heggie, and J.-C. Charlier. π-stacking interaction between carbon nanotubes and organic molecules. *Phys. Rev. B*, 72:075431, 2005.

[42] S. Cambré, W. Wenseleers, E. Goovaerts, and D. E. Resasco. Determination of the metallic/semiconducting ratio in bulk single-wall carbon nanotube samples by cobalt porphyrin probe electron paramagnetic resonance spectroscopy. *ACS nano*, 4(11):6717–6724, 2010.

[43] D.J. Shu and X.G. Gong. Curvature effect on surface diffusion: The nanotube. *The Journal of Chemical Physics*, 114:10922, 2001.

[44] H. Kataura, Y. Maniwa, M. Abe, A. Fujiwara, T. Kodama, K. Kikuchi, H. Imahori, Y. Misaki, S. Suzuki, and Y. Achiba. Optical properties of fullerene and non-fullerene peapods. *Applied Physics A*, 74(3):349–354, 2002.

[45] H. Rauf T. Pichler J. Bernardi H. Peterlik L. Korecz F. Flp F. Simon, H. Kuzmany and A. Jnossy. Low temperature fullerene encapsulation in single wall carbon nanotubes: synthesis of n@c60@swcnt. *Chemical Physics Letters*, 383:362–367, 2004.

[46] K. Suenaga T. Ichihashi A. Hashimoto M. Yudasaka, K. Ajima and S. Iijima. Nano-extraction and nano-condensation for c60 incorporation into single-wall carbon nanotubes in liquid phases. *Chemical Physics Letters*, 380:42–46, 2003.

[47] Occupational safety and health guideline for cobalt carbonyl (u.s. department of health and human services).

[48] K. Smith. *Porphyrins and Metalloporphyrins*. Elsevier Scientific Publishing company, 1975.

[49] A. L. Thomas F. H. Moser. *The Phthalocyanines Volume 1 Properties*. CRC Press, 1983.

[50] E. Dujardin, T. W. Ebbesen, H. Hiura, and K. Tanigaki. Capillarity and wetting of carbon nanotubes. *Science*, 265(5180):pp. 1850–1852, 1994.

[51] T. W. Ebbesen. Wetting, filling and decorating carbon nanotubes. *Journal of Physics and Chemistry of Solids*, 57:951–955, 1996.

[52] R. Malhotra R. S. Ruoff, Doris S. Tse and Donald C. Lorents. Solubility of fullerene (c60) in a variety of solvents. *The Journal of Physical Chemistry*, 97:3379–3383, 1993.

[53] A. Bondi. van der waals volumes and radii. *The Journal of Physical Chemistry*, 68:441–451, 1964.

[54] N. A. Lange; J. A. Dean. *LANGE'S HANDBOOK OF CHEMISTRY 14th Edition*. McGraw-Hill, 1992.

[55] M. Roth, K. Maag, G. M. Schneider, and Dirk T. Solution properties of c60 and c70 fullerenes and c21 to c40 n-alkanes at infinite dilution in carbon dioxide from supercritical fluid chromatography. *The Journal of Physical Chemistry B*, 105(42):10373–10378, 2001.

[56] S.A. Westwood. *Supercritical Fluid extraction and its use on in chromatographic sampler preparation*. Blackie academic and professional, 1992.

[57] S. Rizvi. *Supercritical fluid processing of food and biomaterials*. Chapman and Hall, 1994.

[58] J. M. DeSimone. Practical approaches to green solvents. *Science*, 297(5582):799–803, 2002.

[59] S. Iijima and T. Ichihashi. Single-shell carbon nanotubes of 1-nm diameter. *Nature*, 363:603 – 605, 1993.

[60] Nanocyl^{TM} nc1000 10 march 2009 - v03. Manufacturers data sheet containing information on the NC1100 nanotubes used in this study.

[61] Y. Li, W. Kim, Y. Zhang, M. Rolandi, D. Wang, and H. Dai. Growth of single-walled carbon nanotubes from discrete catalytic nanoparticles of various sizes. *The Journal of Physical Chemistry B*, 105(46):11424–11431, 2001.

[62] V. Georgakilas, D. Voulgaris, E. Vazquez, Maurizio P., D. M. Guldi, A. Kukovecz, and H. Kuzmany. Purification of hipco carbon nanotubes via organic functionalization. *Journal of the American Chemical Society*, 124(48):14318–14319, 2002.

[63] Y. Feng, H. Zhang, Y. Hou, T. P. McNicholas, D. Yuan, S. Yang, L. Ding, W. Feng, and Jie Liu. Room temperature purification of few-walled carbon nanotubes with high yield. *ACS nano*, 2(8):1634–1638, 2008.

[64] K. Tohji, H. Takahashi, Y. Shinoda, N. Shimizu, B. Jeyadevan, I. Matsuoka, Y. Saito, A. Kasuya, S. Ito, and Y. Nishina. Purification procedure for single-walled nanotubes. *The Journal of Physical Chemistry B*, 101(11):1974–1978, 1997.

[65] P.M. Ajayan, T.W. Ebbesen, T. Ichihashi, S. Iijima, K.S. Tanigaki, and H. Hiura. Opening carbon nanotubes with oxygen and implications for filling. *Nature*, 362:522 – 525, 1993.

[66] K. Sathiyamoorthy, C. Vijayan, and S. Varma. Nonlinear optical response of chloroaluminiumphthalocyanine encapsulated by silica core-shell particles. *Langmuir*, 24(14):7485–7491, 2008.

[67] S. Wischnitzer. *Introduction to Electron Microscopy*. Pergamon Press, 1981.

[68] B. W. Smith and D. E. Luzzi. Electron irradiation effects in single wall carbon nanotubes. *Journal of applied Physics*, 90(7):3509–3515, 2001.

[69] F. Banhart. Irradiation effects in carbon nanostructures. *Reports on Progress in Physics*, 62(8):1181, 1999.

[70] A. Ilie, S. Crampin, L. Karlsson, and M. Wilson. Repair and stabilization in confined nanoscale systemsinorganic nanowires within single-walled carbon nanotubes. *Nano Research*, 5(12):833–844, 2012.

[71] Crystalmaker,2.0; crystalmaker software: Oxford, 2006.

[72] A. Gómez-Rodríguez, L. M. Beltrán-del Río, and R. Herrera-Becerra. Simulatem: Multislice simulations for general objects. *Ultramicroscopy*, 110(2):95–104, 2010.

[73] A. Thust C. Kbel. *'TrueImage: Introduction to Focal-Series Reconstruction' in Nato Science Series E.* Kluwer Academic Publishers, 2005.

[74] K. Schulte, J. C. Swarbrick, N. A. Smith, F. Bondino, E. Magnano, and A. N. Khlobystov. Assembly of cobalt phthalocyanine stacks inside carbon nanotubes. *Advanced Materials*, 19(20):3312–3316, 2007.

[75] S. Okada and H. Segawa. Substituent-control exciton in j-aggregates of protonated water-insoluble porphyrins. *Journal of the American Chemical Society*, 125(9):2792–2796, 2003.

[76] Y. Fujita, S. Bandow, and S. Iijima. Formation of small-diameter carbon nanotubes from ptcda arranged inside the single-wall carbon nanotubes. *Chemical physics letters*, 413(4):410–414, 2005.

[77] M. C. Tobin. *Laser Raman spectroscopy.* Wiley-Interscience, 1971.

[78] P. J. Hendra T. R. Gilson. *Laser Raman Spectroscopy.* Wiley-Interscience, 1970.

[79] S. Sasic. *Pharmaceutical applications of Raman spectroscopy.* Wiley-Interscience, 2008.

[80] R. Saito, M. Hofmann, G. Dresselhaus, A. Jorio, and M.S. Dresselhaus. Raman spectroscopy of graphene and carbon nanotubes. *Advances in Physics*, 60(3):413–550, 2011.

[81] A.M. Rao, E. Richter, S. Bandow, B. Chase, P.C. Eklund, K.A. Williams, S. Fang, K.R. Subbaswamy, M. Menon, A. Thess, et al. Diameter-selective raman scattering from vibrational modes in carbon nanotubes. *Science*, 275(5297):187–191, 1997.

[82] M. J. OConnell, S. Sivaram, and S. K. Doorn. Near-infrared resonance raman excitation profile studies of single-walled carbon nanotube intertube interactions: A direct comparison of bundled and individually dispersed hipco nanotubes. *Physical Review B*, 69(23):235415, 2004.

[83] S. Piscanec, M. Lazzeri, J. Robertson, A. C. Ferrari, and F. Mauri. Optical phonons in carbon nanotubes: Kohn anomalies, peierls distortions, and dynamic effects. *Physical Review B*, 75(3):035427, 2007.

[84] S.D.M. Brown, A. Jorio, P. Corio, M.S. Dresselhaus, G. Dresselhaus, R. Saito, and K. Kneipp. Origin of the breit-wigner-fano lineshape of the tangential g-band feature of metallic carbon nanotubes. *Physical Review B*, 63(15):155414, 2001.

[85] S. K. Das, A. S.D. Sandanayaka, N. K. Subbaiyan, M. E. Zandler, O. Ito, and F. D'Souza. Functionalization of diameter-sorted semiconductive swcnts with photosensitizing porphyrins: Syntheses and photoinduced electron transfer. *Chemistry-A European Journal*, 18(36):11388–11398, 2012.

[86] H. Zhao, Y. Zhu, C. Chen, L. He, and J. Zheng. Synthesis, characterization, and photophysical properties of covalent-linked ferrocene–porphyrin–single-walled carbon nanotube triad hybrid. *Carbon*, 50(13):4894–4902, 2012.

[87] B. Ballesteros, G. de la Torre, C. Ehli, G.M. Aminur Rahman, F. Agullo-Rueda, D. M. Guldi, and T. Torres. Single-wall carbon nanotubes bearing covalently linked phthalocyanines-photoinduced electron transfer. *Journal of the American Chemical Society*, 129(16):5061–5068, 2007.

[88] T. Mugadza and T. Nyokong. Covalent linking of ethylene amine functionalized single-walled carbon nanotubes to cobalt (ii)

tetracarboxyl-phthalocyanines for use in electrocatalysis. *Synthetic Metals*, 160(19):2089–2098, 2010.

[89] W. Chidawanyika and T. Nyokong. Characterization of amine-functionalized single-walled carbon nanotube-low symmetry phthalocyanine conjugates. *Carbon*, 48(10):2831–2838, 2010.

[90] C. Meyer, C. Besson, R. Frielinghaus, A. Saelhoff, H. Flötotto, L. Houben, P. Kögerler, and C. M. Schneider. Covalent functionalization of carbon nanotubes with tetramanganese complexes. *physica status solidi (b)*, 249(12):2412–2415, 2012.

[91] M.V. Kharlamova, L.V. Yashina, A.A. Eliseev, A.A. Volykhov, V.S. Neudachina, M.M. Brzhezinskaya, T.S. Zyubina, A.V. Lukashin, and Yu D Tretyakov. Single-walled carbon nanotubes filled with nickel halogenides: Atomic structure and doping effect. *physica status solidi (b)*, 249(12):2328–2332, 2012.

[92] F.H. Monteiro, D.G. Larrude, M.E.H. Maia da Costa, and F.L. Freire. Estimating the boron doping level on single wall carbon nanotubes using raman spectroscopy. *Materials Letters*, 2012.

[93] S. Suzuki and H. Hibino. Characterization of doped single-wall carbon nanotubes by raman spectroscopy. *Carbon*, 49(7):2264–2272, 2011.

[94] G. Jayamurugan, K.S. Vasu, Y.B.R.D. Rajesh, S. Kumar, V. Vasumathi, P.K. Maiti, A.K. Sood, and N. Jayaraman. Interaction of single-walled carbon nanotubes with poly (propyl ether imine) dendrimers. *The Journal of Chemical Physics*, 134:104507, 2011.

[95] L.G. Moura, L.M. Malard, M.A. Carneiro, P. Venezuela, R. B. Capaz, D. Nishide, Y. Achiba, H. Shinohara, and M.A. Pimenta. Charge transfer and screening effects in polyynes encapsulated inside single-wall carbon nanotubes. *Physical Review B*, 80(16):161401, 2009.

[96] R. B. Koizhaiganova, D. H. Hwang, C. J. Lee, S. Roth, and U. Dettlaff-Weglikowska. N-type doping effect of single-walled carbon nanotubes with aromatic amines. *physica status solidi (b)*, 247(11-12):2793–2796, 2010.

[97] M.V. Kharlamova and J.J. Niu. Comparison of metallic silver and copper doping effects on single-walled carbon nanotubes. *Applied Physics A*, 109(1):25–29, 2012.

[98] A. Ghosh, K. V. Rao, R. Voggu, and S. J. George. Non-covalent functionalization, solubilization of graphene and single-walled carbon nanotubes with aromatic donor and acceptor molecules. *Chemical Physics Letters*, 488(4):198–201, 2010.

[99] Dr. s. maruyama, 2002. kataura-plot for resonant raman [online]. department of mechanical engineering, the university of tokyo, tokyo. available from: http://www.photon.t.u-tokyo.ac.jp/ maruyama/kataura/kataura.html [accessed november 20013].

[100] S. Reich, C. Thomsen, and P. Ordejon. Electronic band structure of isolated and bundled carbon nanotubes. *Physical Review B*, 65(15):155411, 2002.

[101] F. Hennrich, R. Krupke, S. Lebedkin, K. Arnold, R. Fischer, D. E. Resasco, and M. M. Kappes. Raman spectroscopy of individual single-walled carbon nanotubes from various sources. *The Journal of Physical Chemistry B*, 109(21):10567–10573, 2005.

[102] A. Ilie, J.S. Bendall, D. Roy, E. Philp, and M.L.H. Green. Effects of ki encapsulation in single-walled carbon nanotubes by raman and optical absorption spectroscopy. *The Journal of Physical Chemistry B*, 110(28):13848–13857, 2006.

[103] M. Steiner, M. Freitag, J. C. Tsang, V. Perebeinos, A. A. Bol, A. V. Failla, and P. Avouris. How does the substrate affect the raman and excited state spectra of a carbon nanotube? *Applied Physics A*, 96(2):271–282, 2009.

[104] Y. Zhang, H. Son, J. Zhang, J. Kong, and Z. Liu. Laser-heating effect on raman spectra of individual suspended single-walled carbon nanotubes. *The Journal of Physical Chemistry C*, 111(5):1988–1992, 2007.

[105] H.D. Li, K.T. Yue, Z.L. Lian, Y. Zhan, L.X. Zhou, S.L. Zhang, Z.J. Shi, Z.N. Gu, B.B. Liu, R.S. Yang, et al. Temperature dependence of the raman spectra of single-wall carbon nanotubes. *Applied Physics Letters*, 76(15):2053–2055, 2000.

[106] Z. Zhou, X. Dou, L. Ci, L. Song, D. Liu, Y. Gao, J. Wang, L. Liu, W. Zhou, S. Xie, et al. Temperature dependence of the raman spectra of individual carbon nanotubes. *The Journal of Physical Chemistry B*, 110(3):1206–1209, 2006.

[107] A. Jorio, C. Fantini, M.S.S. Dantas, M.A. Pimenta, A.G. Souza Filho, G. G. Samsonidze, V.W. Brar, G. Dresselhaus, M.S. Dresselhaus, A.K. Swan, et al. Linewidth of the raman features of individual single-wall carbon nanotubes. *Physical Review B*, 66(11):115411, 2002.

[108] N. R. Raravikar, P. Keblinski, A. M. Rao, M. S. Dresselhaus, L. S. Schadler, and P. M. Ajayan. Temperature dependence of radial breathing mode raman frequency of single-walled carbon nanotubes. *Physical Review B*, 66(23):235424, 2002.

[109] C. Fantini, A. Jorio, M. Souza, M.S. Strano, M.S. Dresselhaus, and M.A. Pimenta. Optical transition energies for carbon nanotubes from resonant raman spectroscopy: Environment and temperature effects. *Physical review letters*, 93(14):147406, 2004.

[110] M. Takase, H. Nabika, S. Hoshina, M. Nara, K. Komeda, R. Shito, S. Yasuda, and K. Murakoshi. Local thermal elevation probing of metal nanostructures during laser illumination utilizing surface-enhanced raman scattering from a single-walled carbon nanotube. *Phys. Chem. Chem. Phys.*, 15(12):4270–4274, 2013.

[111] S. Chiashi, Y. Murakami, Y. Miyauchi, and S. Maruyama. Temperature dependence of raman scattering from single-walled carbon nanotubes: Undefined radial breathing mode peaks at high temperatures. *Japanese Journal of Applied Physics-Part 1 Regular Papers and Short Notes*, 47(4):2010–2015, 2008.

[112] W. Wenseleers, S. Cambré, J. Čulin, A. Bouwen, and E. Goovaerts. Effect of water filling on the electronic and vibrational resonances of car-

bon nanotubes: Characterizing tube opening by raman spectroscopy. *Advanced Materials*, 19(17):2274–2278, 2007.

[113] Z. Liu, X. Zhang, Y. Zhang, and J. Jiang. Theoretical investigation of the molecular, electronic structures and vibrational spectra of a series of first transition metal phthalocyanines. *Spectrochimica Acta Part A: Molecular and Biomolecular Spectroscopy*, 67(5):1232–1246, 2007.

[114] T. Takenobu, T. Takano, M. Shiraishi, Y. Murakami, M. Ata, H. Kataura, Y. Achiba, and Y. Iwasa. Stable and controlled amphoteric doping by encapsulation of organic molecules inside carbon nanotubes. *Nature Materials*, 2(10):683–688, 2003.

[115] J. Zhu, B. S. Shim, M. Di Prima, and N. A. Kotov. Transparent conductors from carbon nanotubes lbl-assembled with polymer dopant with $\pi-\pi$ electron transfer. *Journal of the American Chemical Society*, 133(19):7450–7460, 2011.

[116] M.S. Roy, P. Balraju, Y.S. Deol, S.K. Sharma, and G.D. Sharma. Charge-transport and photocurrent generation in bulk hetero junction based on chloro-aluminum phthalocyanine (clalpc) and rose bengal (rb). *Journal of Materials Science*, 43(16):5551–5563, 2008.

[117] A. V. Soldatova, J. Kim, X. Peng, A. Rosa, G. Ricciardi, M. E. Kenney, and M. A. J. Rodgers. Effects of benzoannulation and α octabutoxy substitution on the photophysical behavior of nickel phthalocyanines: A combined experimental and dft/tddft study. *Inorganic Chemistry*, 46(6):2080–2093, 2007.

[118] Y. Zhang, W. Ruan, Z. Li, Y. Wu, and J. Zheng. Dft study on the influence of$< i >$meso$< /i >$-phenyl substitution on the geometric, electronic structure and vibrational spectra of free base porphyrin. *Chemical physics*, 315(1):201–213, 2005.

[119] B. Shan and K. Cho. First principles study of work functions of single wall carbon nanotubes. *Physical review letters*, 94(23):236602, 2005.

[120] J. Kong, N. R. Franklin, C. Zhou, M. G. Chapline, S. Peng, K. Cho, and H. Dai. Nanotube molecular wires as chemical sensors. *Science*, 287(5453):622–625, 2000.

[121] S. Maji and S. Sarkar. Homo based two electrons and one-electron oxidation in planar and nonplanar methoxy-substituted nickel tetraphenylporphyrins. *Inorganica Chimica Acta*, 363(12):2778–2785, 2010.

[122] N. Bendiab, L. Spina, A. Zahab, P. Poncharal, C. Marliere, J.L. Bantignies, E. Anglaret, and J.L. Sauvajol. Combined in situ conductivity and raman studies of rubidium doping of single-wall carbon nanotubes. *Physical Review B*, 63(15):153407, 2001.

[123] A. Ilie, S. Egger, S. Friedrichs, D. Kang, and M. L. H. Green. Correlated transport and high resolution transmission electron microscopy investigations on inorganic-filled single-walled carbon nanotubes showing negative differential resistance. *Applied Physics Letters*, 91(25):253124–253124, 2007.

[124] A. Weber-Bargioni, A. Schwartzberg, M. Cornaglia, A. Ismach, J. J. Urban, Y. Pang, R. Gordon, J. Bokor, M. B. Salmeron, D. F. Ogletree, et al. Hyperspectral nanoscale imaging on dielectric substrates with coaxial optical antenna scan probes. *Nano letters*, 11(3):1201–1207, 2011.

[125] A. Hartschuh, E. J. Sánchez, X. S. Xie, and L. Novotny. High-resolution near-field raman microscopy of single-walled carbon nanotubes. *Physical Review Letters*, (9):095503–1, 2003.